Doctoral Dissertation
Doctoral Program in Electrical, Electronics and Communications Engineering
(33th Cycle)

Microfluidic devices: application for liquid biopsy

Federica Barbaresco
* * * * * *

Supervisors
Prof. C. F. Pirri, Supervisor
Prof. M. Cocuzza, Co-Supervisor

Politecnico di Torino
January, 2021

I hereby declare that, the contents and organisation of this dissertation constitute my own original work and does not compromise in any way the rights of third parties, including those relating to the security of personal data.

…….....

Federica Barbaresco

Turin, January, 2021

Summary

Lung cancer is nowadays a leading cause of death, second only to cardiovascular diseases. Thus, the large diffusion and incidence make the development of new diagnostic tools of crucial importance for lung cancer early detection, prognosis and treatment. In recent years, due to research improvements in cancer studies and biomedical technologies, liquid biopsy, a non-invasive and real-time monitoring approach, resulted a promising tool for the early diagnosis of cancer alterations. Moreover, this highly sensitive technique permits to control the evolution of lung cancer at different stages contributing to adjust therapy according to a personalized patient's treatment. Liquid biopsy concerns the analysis of biomarkers (i.e. cells, extracellular vescicles, sequence of nucleic acids, etc.) from blood or any other body fluids into integrated and automated microfluidic systems for point-of-care or in-the-field detection. Thus, the development of enhanced microfluidic devices, thanks to their characteristics, could overcome some critical aspects derived from traditional approaches, leading to a widespread application of liquid biopsy in everyday use either in diagnostic and in clinical practice.

In this contest, this PhD Thesis focuses on the development of three microfluidic devices for the separation or detection of biomarkers for the early diagnosis and screening of lung cancer treatment. In detail, each microfluidic device is referred to a specific class of biomarker. Thus, for each chip a proper design and fabrication method were selected depending on its functionality. Then, devices feature dimensions and their performances were investigated either with synthetic and biological samples employing different approaches.

At first, a novel free-flow microfluidic device was developed exploiting the 3D printing technology to manipulate the motion of particles and exosomes. Morphological characterizations of device features dimensions highlighted how an accurate reproducibility of the design was performed employing an additive manufacturing method. Moreover, 3D printing allowed to easily integrate threated

fluidic fittings features in the chip in correspondence to inlet and outlet ports for tube interconnection by modifying a preliminary design of the device. Results performed with this device demonstrated their ability to tune the motion of analytes, owing different surface-to-charge ratios (i.e. particles and exosomes) either as single or mixed population, in a specific outlet when a defined voltage value at the electrodes was imposed and to accumulate them in a microliter volume range.

A second microfluidic device was developed throughout a silicon micromachining fabrication process to separate biomarkers possessing micrometric dimensions by exploiting acoustic forces. To allow the creation of an acoustic standing wave field into the microfluidic channel a customized set-up, with related protocol steps, was assembled and investigated. Afterwards, device focalization performances were evaluated by inspecting samples composed either by polystyrene micro- and nanoparticles and cells as single or mixed populations collected at the outlets of the device when different setting conditions (i.e. sample concentration, applied voltage value at the piezoelectric element and flow rate) were applied. Regarding micro particles tests, higher focalization performances were proven when lower concentration, lower flow rate and higher applied voltage value to the transducer were imposed. In addition, confirmation of these data resulted by comparing them to simulated ones. Furthermore, high focalization values with cells resulted both at high flow rate and when cells were mixed with population of micro- and nanoparticles without affecting focalization performances of the device.

Finally, two PDMS-based microfluidic devices, characterized with different surface-to-volume ratios, were designed and evaluated to capture low amount of microRNA molecules. Results performed throughout PCR reaction assays either with synthetic microRNAs and a pool of microRNA molecules associated to non-small cell lung carcinoma spiked in water or human plasma demonstrated higher performances of these devices to capture biomarkers with respect to a previous PDMS-based device, due to their higher availability of internal surfaces. Moreover, a rapid and automatized set-up for the capture of microRNAs was assembled and presented.

To conclude, microfluidic devices developed during this PhD Thesis work constitute proof-of-concepts for the development of new diagnostic tools for liquid biopsy. Further improvements regarding the presented chips, as well as their integration into a unique microfluidic platform will offer a new, rapid, low cost and multiple-analysis diagnostic tool able to overcome current challenges.

Acknowledgments

I would like to express my gratitude to my supervisors Prof. Fabrizio Pirri and Prof. Matteo Cocuzza for giving me the opportunity to take up this outstanding PhD journey. I would like to thank my mentors Simone Marasso, Giancarlo Canavese and Valentina Cauda for guiding, supporting and encouraging me during these years. At the same time, I want to acknowledge Cristina Potrich, Cecilia Pederzolli, Lorenzo Lonelli and all the other members at the *Centre for Materials and Microsystems* at the Fondazione Bruno Kessler in Trento to introduce me into a biological contest and how to handle biological elements and to join them with nanotechnology. I gratefully acknowledge Mauro Raimondo and Salvatore Guastella for FESEM analyses. I would like to thank all the members of the *χLab* and *THN Lab* who helped me during these years and shared with me many moments in lab as well as during breaks.

Personally, a big thank goes to the DISAT PhDs and staffs current and former members who helped me not only as colleagues, but as friends, supporting me and sharing with me funny moments. Thus, an extraordinary thank goes to Veronica, Anna, Roberta, Luisa B., Alessandro, Giorgio, Vittorio, Federico, Gianluca, Pietro, Marco, Luca, Roberto, Nicolò, Davide and Marco. In particular, a devoted thank goes to my friends Bianca, Marta, Luisa and Gullo, thanks for having supported me every moment in every state of my mind ☺.

I would like to thank all my friends Daniela, Ludovica, Cecilia, Giulia, Marta, Bessy, Feddy, Alessandro E., Alessandro G. and Stefano for their longtime friendship and constant sustain. The biggest devoted thank goes to Bianca, for being part of my life in every moments and situations.

A special thank goes to my "second family" all the members of *ASAKI*, who sustained me during these intense years, thus thank to Diego (Il Sommo), Alessandro (Kung Fu Panda), Fulvio (Bro), Yuri, Roberto, Sara, Mauro, Claudio, Fabrizio, Elena, Michele, Giuseppe (Giuseppi) and my Mum as aikido-mate.

Last but not least, I would like to acknowledge all my parents, uncles and cousins. I'm born in the most beautiful and funniest family of the world. I want to thank my grandparents Angelica, Primo, Adelma and Angelo for raising me as the person who I am. And of course, I deeply thank my Mother and my Father for their unconditionally love and encouragement in every day moment.

Finally, to my sweetheart Federico goes the most devoted acknowledgment, you are the sunshine in my life.

To my loving parents
Angelica, Adelma,
Primo, Angelo,
Antonella, Maurizio
and
my soul mate Federico

Contents

List of Tables

List of Figures

Chapter 1

Introduction

1.1 New challenges for lung cancer diagnosis

1.1.1 Lung cancer diagnosis

According to the International Agency for Research on Cancer (IARC) a specialized agency of the World Health Organization (WHO), the second most common cause of death worldwide after cardiovascular diseases is cancer[1].

Based on data collected in 2018, from 185 countries and territories among 36 types of cancers, lung cancer was the main cause of cancer death with an incidence of 2.09 million cases and a mortality of 1.76 million cases. Adding demographic changes to previous assumptions, IARC predicts that lung cancer will reach an incidence of 3.61 million cases with a mortality equal to 3.10 million cases in 2040.

Lung cancer arises from the respiratory epithelium cells and can be divided into two wide categories: small cell lung carcinoma (SCLC) and non-small cell lung carcinoma (NSCLC). The first type is a malignant tumor derived from cells exhibiting neuroendocrine characteristics, while the second one accounts the 85% of lung cancers and it is subdivided into three main classes: adenocarcinoma, squamous cell carcinoma and large cell carcinomas[2][3][4](**Figure 1.1.1**). Lung cancer is initially asymptomatic, thus, despite advances in early detection and standard treatment for most other cancer types, this cancer is often diagnosed at advanced stages were the survival rates are discouraging[3][4][5]. Indeed, according to IARC data, the five-year relative survival rate of all lung cancer types is 20.5%. In addition, although smoking is the major risk factor of lung cancer, accounting the 80-90% of tumors, only approximately 15% of smokers develop lung cancer, suggesting that other risk factors must be identified[6][7][8][9]. Indeed, there are several factors associated with an increased risk of developing lung cancer in never smokers, estimated as the 25% of all lung cancer cases, including second hand smoke, indoor air pollution, occupational exposure either to carcinogens and to cooking oil fumes and genetic modifications[10][11].

To conclude, based on literatures and statistical data, lung cancer represents a critical global public health issue to which research must be addressed to improve a better understanding of its pathophysiology and molecular origins to allow the development of diagnostic tools for the early detection, prognosis and treatments of this disease.

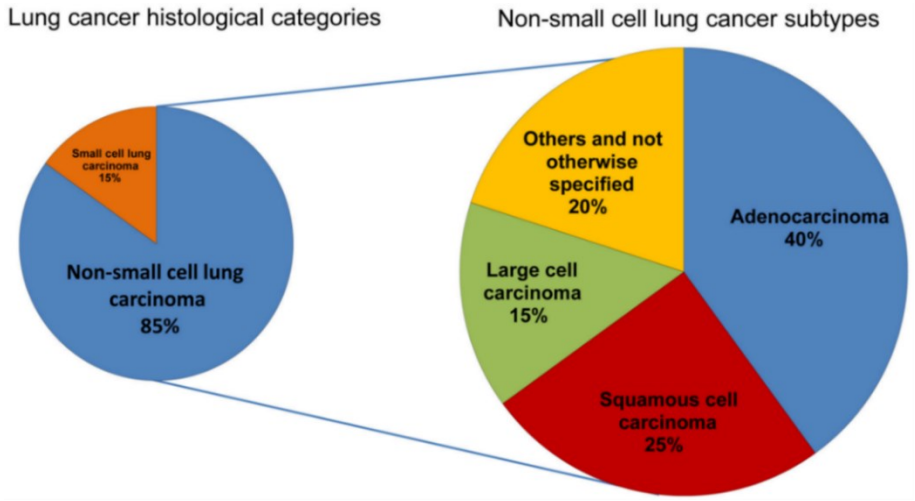

Figure 1.1.1 Histological classification of lung cancer. Image from [3].

1.1.2 Liquid biopsy

At present performing an early diagnosis of cancer alterations is of fundamental importance for patient's clinical evaluation and treatment strategy. Generally, conventional tissue biopsy is exploited to assess cancer's mutational profile (i.e. primary tumor or metastasis), but there are several limitations derived from this approach. Indeed, when it is possible to reach the lung cancer, biopsy sampling involves invasive and harmful surgical interventions. In addition, tissue biopsy is a localized analysis, thus it is not able to characterize intra- or inter-tumor heterogeneity, which is fundamental to assess cancer in its advanced stages or in presence of different tumor sites. Furthermore, it is not possible to perform serial tissue biopsies to achieve a dynamic follow-up of cancer molecular modifications in order to evaluate cancer progression and evolutions in patients[12]. Because of this, the National Lung Screening Trial investigated the low-dose computed tomography (LDCT) analysis for the screening of lung cancer, as alternative approach. But, even if researchers demonstrated a reduction in lung cancer mortality, repeated LDCT screening tests are not suggested, due to the accumulation of radiation exposure[6].

To overcome such critical issues, thanks to research improvements either in cancer studies and in biomedical technologies (i.e. microfluidic devices) new diagnostic tools are being developed. Among these stands out liquid biopsy, a high sensitive technique, that helps to manage lung cancer screening and to adjust therapy according to a personalized patient's treatment.

Liquid biopsy concerns the analysis of any tumor-derived material circulating in blood or any other body fluids instead of a fragment of cancer tissue[13] (**Figure 1.1.2**). It is a non-invasive and real-time monitoring approach requiring low time and costs for sample taking. It can improve the early diagnosis to identify asymptomatic cancer patients through the systematic and routine measurements of tumor-derived biomarkers[14][15]. In addition, it was demonstrated that liquid biopsy is a highly sensitive assay able to detect the presence of tumor cells in

different organs in patients who lack any clinical or radiological signs or residual tumor cells left behind after local invasive therapy[16].

Up to now, a relevant branch of literature has emerged highlighting potential clinical applications of liquid biopsy even throughout preliminary results derived from many clinical trials. Despite several challenges, the next coming years will be based on further works in standardization of analytical procedures that must be performed and generalized for all components upon which liquid biopsies are based[17][18][19][20].

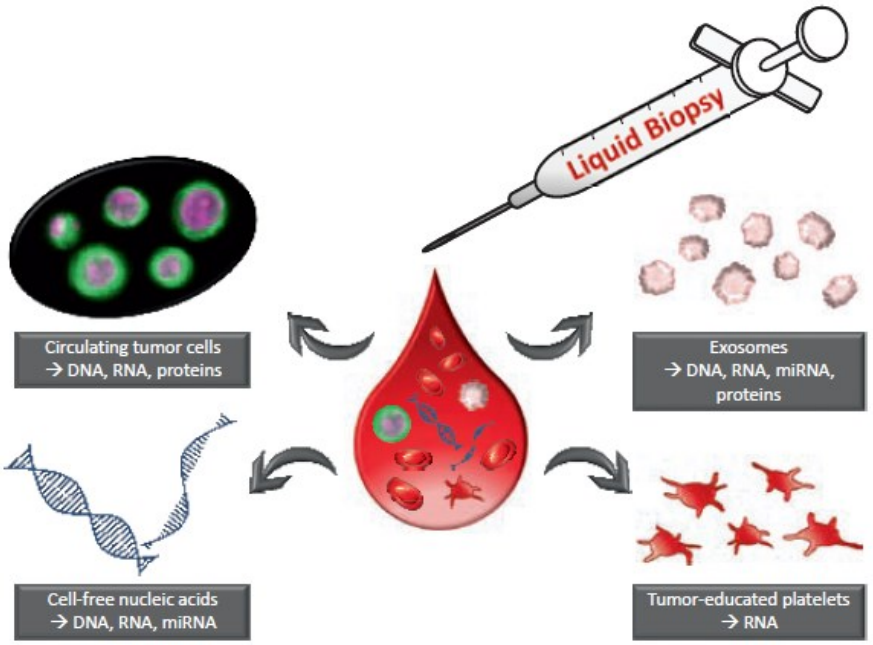

Figure 1.1.2 Liquid biopsy provides a variety of clinically informative components. Image from[13].

1.2 Biomarkers

1.2.1 Classification

As mentioned before, biomarkers are objective and measurable entities of characteristic biological processes taken into account in liquid biopsy. By definition they are characteristic indicators measured and evaluated to check normal biological and pathogenic processes or pharmacological responses to a therapeutic intervention[21]. Due to this, they are used for a variety of purposes such as diagnostic, monitoring, predictive and prognostic tools. In addition, conversely to direct measures correlated with patients' experiences and sense of wellbeing, biomarkers can detect variations on biological processes even if there are no changes on the patient's clinical state[22][23]. They should not be examined as surrogate of clinical outcomes, but together. Indeed, understanding the relationship between these elements should increase the knowledge of normal and healthy physiology, as well as expand the awareness of treatments for many diseases[24].

Regarding cancer biomarkers, they include a variety of biochemical species as circulating tumor cells, exosomes, platelets, tumor-derived nucleic acids, proteins, cytogenetic and cytokinetic parameters[25][26][27]. Usually, among these a panel of biomarkers is required instead of the expression of a single biomarker, to avoid false responses in cancer diagnosis. Up to now, innovative clinical trial approaches the use of biomarkers, but future optimization strategies must be achieved in developing efficient detection platforms owing high sensitivity, selectivity, throughput, as well as the detection of new biomarkers in specific fields[28][29].

Below follows a brief descriptions of the type of biomarkers which is referred this thesis work for the early diagnosis and prognosis of lung cancer.

1.2.2 Circulating tumor cells

Circulating tumor cells (CTCs) were first discovered in 1869, when Ashworth discovered cells identical to cancer ones in blood[30]. Some tumor cells, as a consequence of the connection loss between adjacent cells and the extracellular matrix, detach from the primary tumor allowing its dissemination and the creation of metastatic sites through the circulation[31]. When CTCs enter in blood or in lymphatic vessels they can be arranged as cluster (25-100 cells) or as single entity. Usually, the immune system erases the 85% of CTCs and the surviving cells persist in the circulation few hours before undergo apoptosis. For this reason, CTCs are a rare population in blood, indeed, one CTC is detected per 10^5-10^7 mononuclear cells, and between these CTCs only the 3% is constituted by a CTC clusters[32][33].

During the metastasis progression, CTCs cells acquire mutations different from the primary tumor, therefore, since they possess intra-tumor heterogeneity

characteristics, CTCs have been investigated as diagnostic, prognostic as well as predictive biomarkers in numerous type of cancer. Up to now, CTCs count represents a prognostic factor in prostate, breast and colorectal cancers, but additional research must be performed to demonstrate the clinical utility of CTCs in routine clinical practice[34][35]. Indeed, although CTCs presents different characteristics from erythrocytes or leukocytes as increased and irregular nucleus and cell shapes and different electro-magnetic charges, the limited number of CTCs available in blood introduce a challenge for currently method exploited in CTCs enrichment and detection[36][37]. In detail, the lack of the development of standardized methods for CTCs detection as well as an established a recognized cut-off values to distinguish between healthy and not-healty patients are some critical issues involving the employment of CTCs as early diagnosis biomarkers in lung cancer[38]. In the future, larger studies should be performed to assess the clinical validity of CTCs in cancers, among these the lung one, leading the development of new anticancer strategy related to an early detection of drug-resistance events or high risk of metastasis development[39][40].

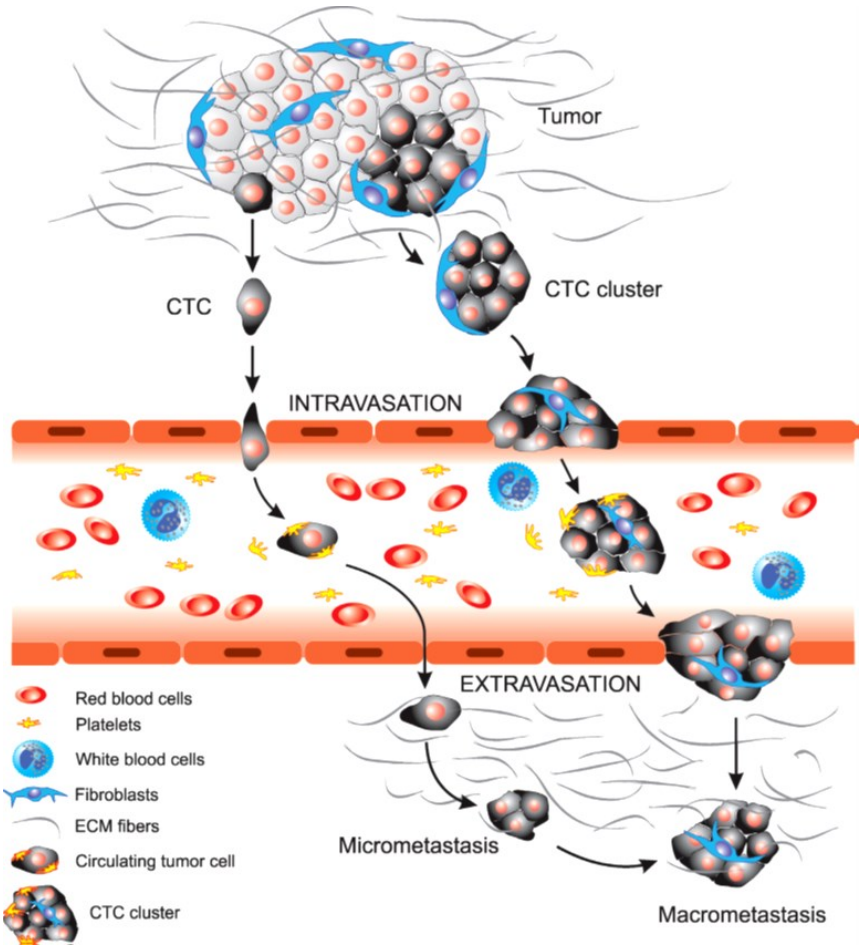

Figure 1.2.1 Overview of circulating tumor cells (CTCs) and/or CTC clusters involved in the tumor metastasis development. Image from[32].

1.2.3 Extracellular vescicles and exosomes

Among biomarkers entities, cancer related-exosomal biomarkers have been investigated due to their potential uses in clinical practice either for the early diagnosis and prognosis, but also as indicators of lung cancer progression[41][42][43].

They were firstly discovered in 1981, by analysing extracellular vesicles (EVs) produced by normal and cancerous cells during the maturation process of reticulocytes throughout a Transmission Electron Microscopy (TEM) characterization[44].

According to a common and widespread classification method, EVs are grouped for dimensions, different intracellular sources and specific biological functions in the following main categories: microvescicles, apoptotic bodies, and exosomes (**Figure 1.2.2**)[45][46]. The first class, characterized by EVs of dimensions between 50 and 500 nm, sometime extended up to 1 μm or even 10 μm in case of oncosomes (cancer-derived microvesicles), derives directly from the budding and subsequent fission of plasma membrane[47]. Apoptotic bodies, instead, comprehend larger vesicles of about 1-2 μm released by cells during the apoptotic process and containing a portion of dying cells cytoplasm[48]. Finally, exosomes originated by the inward budding of endosomal compartments into multi-vesicular bodies, whose diameter range from 40 to 100 nm, are released in the extracellular environment through fusion with the cell membrane. They are secreted by different type of cells, including normal and diseased ones, in many biological fluids such as saliva, blood, urine, amniotic liquid, breast milk and synovial fluid. Thus, thanks to their membranes composed by a lipid bilayer, exosomes can shuttle to neighbouring or considerably distant recipient cells many functional molecules as proteins, structural lipids, metabolites or nucleic acids, derived from secreting cells, located on vesicles membranes or in their cores. In detail, the interaction between exosomes and recipient cells can be explicated directly by a receptor-mediated interaction or be mediated by elements situated in the vesicle lumen[49][50][51].

Therefore, exosomes play a pivotal role in intercellular communication, indeed, depending on their different cellular source, they can be associated with physiological but also pathological conditions like cancer, infectious and neurodegenerative diseases[52][53][54]. Because of this, and also due to the vastness of target cells that exosomes can reach, they are interesting either as biomarkers and as naturally derived drug delivery carriers since they represent an autologous product of human body. Indeed, by transferring cargos from one cancer cell to a healthy one, exosomes can promote the development of cancer cell growth and metastasis. At the same time, exosomal cargos can be exploited for early detection and treatment of cancer comparing them with cancer patients at different stages and healthy people[41].

Finally, to use exosomes in clinical practice, a huge effort needs to be done to overcome the current critical issues regarding exosomes separation techniques from biological fluids.

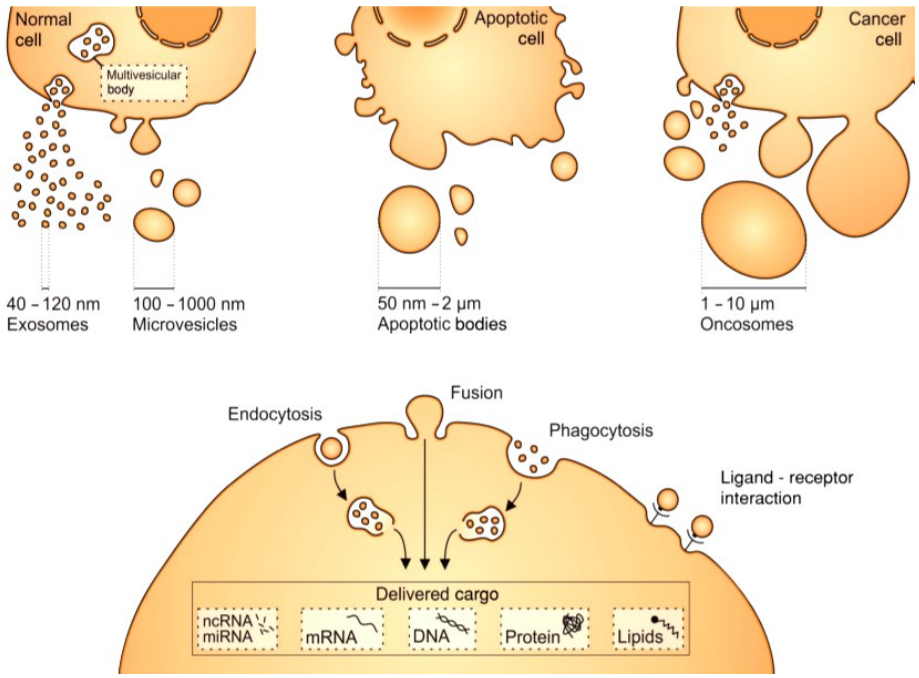

Figure 1.2.2 Types of extracellular vescicles produced by cells with their delivery cargos. Image from[45].

1.2.4 MicroRNAs

MicroRNAs (miRNAs) consist of small, 19-25 nucleotides in size, endogenous ribonucleic acid (RNA) molecules, accounting approximately the 3% of the human genome[55]. Their function is to regulate the post-transcriptional gene expression inside cells, regulating cell cycle and cell differentiation, proliferation and apoptosis by controlling the expression of tumor suppressor genes and oncogenes. In addition, microRNAs are involved in the intercellular communication either when these molecules are located into exosomes and microvescicles travelling stable in an assortment of biological fluids and when isolate microRNAs are detected in serum or plasma[56]. Therefore, mutations or alterations of genome microRNA molecules could result in the progression of many syndromes and diseases such as cancer[55][57].

Indeed, depending if microRNAs molecules are down-regulated or up-regulated, microRNAs can lead to cancer development or suppression, allowing the possibility to exploit circulating microRNAs molecules as potential biomarkers for the early diagnosis, prognosis as well as therapy of various cancers, inducing a real time and dynamic monitoring[58][59]. A schematic representation regarding a series of functions where microRNAs biomarkers are involved in cancer is depicted in **Figure 1.2.3**.

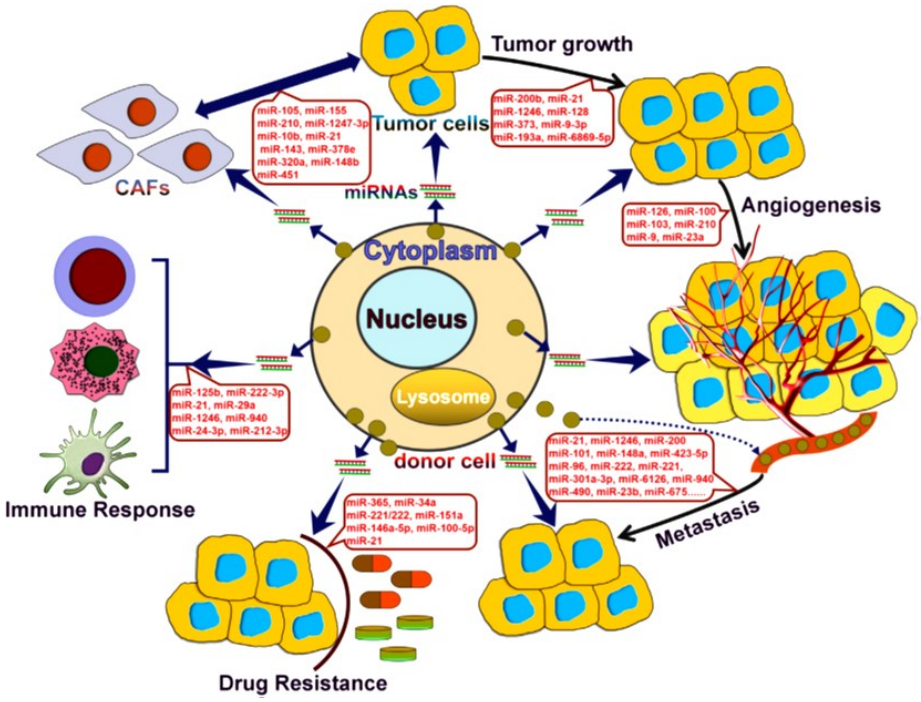

Figure 1.2.3 Function of microRNA biomarkers in cancer. Image from[59].

Notwithstanding research advancements in recent years[60][61][62], the exploitation of miRNAs molecules for early diagnosis and targeted therapies are still at early stages. Additional studies must be performed both to confirm the validity of a panel of microRNA molecules to a specific disease and also to assess a safety protocol to delivery microRNAs to a specific target for therapeutic use[63].

1.3 Microfluidic devices for biomarkers manipulation

1.3.1 Principles of microfluidic devices

In the last decades, the development of microfluidic devices has increased rapidly in various biomedical applications: clinical diagnostics[64], cells and molecules separation[65][64], tissue engineering[66], chemical analysis[67], as well as other fields as automotive and electronics industries[68]. Among previous mentioned applications, microfluidics devices play an important role on the basis of Lab-On-a-Chip (LOC) systems, allowing the miniaturization of laboratory instrumentations and procedure in portable, integrated and automated systems for point-of-care or in-the-field detection[69]. Indeed, LOC comprehend different manipulation steps as sample pre-treatment, analyte separation and/or detection and data analysis, as illustrated in **Figure 1.3.1**.

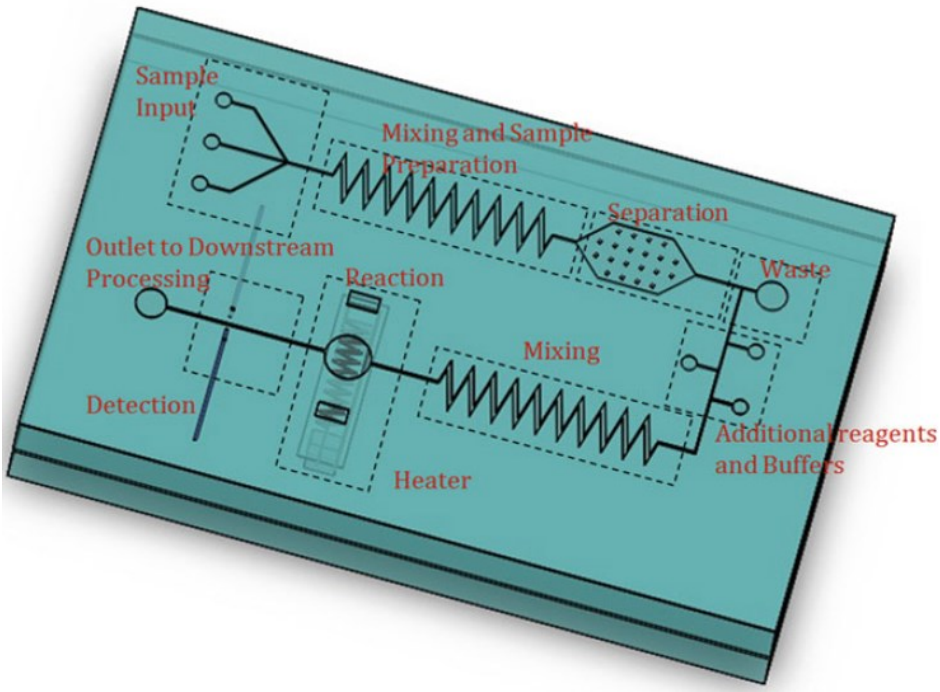

Figure 1.3.1 Lab-On-a-Chip schematic diagram where different components are sketched. Image from[70].

Microfluidics regards the science field which elucidates the description of the phenomena involved in the manipulation of small volume of fluids on the microscale level. Thus, microfluidic devices characterized by having at least one dimension in the micrometres range level (i.e. from 10 to 100 μm), are able to manage and process low quantity of fluids volume, up to 10^{-9} – 10^{-18} L, both concerning samples and reagents. A minute consumption of fluids is useful for handling expensive reagents and samples difficult-to-obtain as well as reducing the

production of waste. Compared to large-scale systems[51], microfluidic devices perform separation and detection operations with high resolution and sensitivity, enabling high-throughput and faster analysis in a reduced response time. Among these properties, microfluidic devices are also defined by simultaneous parallel analysis, fully automated and user-friendly characteristics[70][71][72].

All of these advantages derived from the exploitation of microscale phenomena, such as laminar flow and surface-to-volume ratio, become predominant over forces experienced in everyday life. For instance, laminar flow in microfluidic channels allow to perform experiments for cells sorting by exploiting diffusion between laminar streams able to flow parallel to each other without mixing and acting on cells velocity in a fluid stream. Furthermore, the downscaling leads to an increased surface-to-volume ratio, thus a higher quantity of molecules can be adsorbed on microfluidic channel surfaces in a short time[73]. Concluding, rapid, cost-effective and customizable microfluidic devices represent suitable tools for a widespread development of liquid biopsy in clinical practice[19].

1.3.2 State-of-the-art on materials and microfabrication methods

Silicon, glass, elastomer and plastic represent a list of materials employed for the fabrication of microfluidic systems. Thus, depending on the characteristics of the selected material, many factors, such as microfluidic devices' applications or functions, as well as the employment of a precise fabrication method will be affected[74].

At the beginning, the development of microfluidic devices was based on silicon and glass materials exploiting the same fabrication techniques applied in the microelectronics industry as silicon bulk and surface micromachining or glass etching approaches. Glass and silicon are suitable for their resistance to organic solvent, high thermal conductivity and stable electroosmotic mobility. In addition, glass is optically transparent and electrically insulating, while high vertical sidewalls can be produced in silicon. Although the widespread development of silicon and glass-based microfluidic devices, the hardness of these materials, their non-gas permeability, the opacity of silicon, as well as the employment of expensive and labour intensive micromachining techniques, needed of specialized facilities, limited their application in microfluidics[72][73].

Thus, to overcome such critical issues and to promote a widespread use of microfluidic devices, new fabrication techniques and materials have been investigated[70]. Among these, polymer-based microfluidic devices prevail over silicon and glass materials resulting in processes which are cheaper and suitable for mass production. Moreover, the application of a wide range of polymeric materials (i.e. elastomers, thermosets and thermoplastics) characterized by high biocompatibility, elasticity, transparency and permeation of gases, make them suitable for many biological applications. Commonly, polymer-based microfluidic devices are manufactured throughout molding techniques or laser cutting. Among

these, replica molding, known as soft lithography, became a standard process in the fabrication of microfluidic devices. It exploited photolithography to generate silicon and photoresists masters, over which an elastomer (i.e. polydimethylsiloxane) is poured and cured to reproduce a well-defined replica of micro/nano channels or patterns depicted in the master[75][76] (see **4.1**).

The development of hot-embossing technology, injection molding and laser cutting permit to produce microfluidic devices with thermoplastic materials (i.e. polymethymethacrylate, polystyrene, polyvinylchloride) also ensuring high device throughput, results in cost-efficient and precise microfluidics structures characteristics, essential for the commercial field. In detail, meanwhile hot-embossing and injection molding shaped microfluidic devices applying mold, pressure and heat; laser cutting exploited a pulsed laser irradiation associated with a mask to reproduce the pattern onto the polymer substrate[77]. Finally, in recent years to solve some critical aspect emerged in previous mentioned methods, as creating multi-material objects with high resolution in a reduced fabrication process time and cost, 3D printing technology appears to be a promising fabrication method. This manufacturing process, based on a layer-by-layer technique, is exploited not only for commercial purposes but also for prototyping ones[78].

1.3.3 Classification of microfluidic devices

The motion of biomarkers in microfluidic devices can be controlled using several mechanisms[79][80][81] (**Figure 1.3.2**). They can be classified as label-based or label-free approaches, depending if they act on biochemical or physical biomarker characteristics[82].

In detail, label-based techniques act on specific proteins or molecules presented on nucleic acid sequences or expressed on the surface of cells and vescicles[51][83]. Thus, they can be captured by antibodies or aptamers located on microchannel surfaces (i.e. immunocapture) or by an immunomagnetic approach, where magnetic beads, coated with aptamers and antibodies, are exploited to capture specific biomarkers throughout the application on an external magnetic field[84].

Label-free techniques, instead, are based on mechanical and physical properties of biomarkers such as size, density, compressibility, viscosity, deformability and electromagnetic properties, characteristics of each biomarker[85][86].

Label-free approaches can be categorized as active or passive if an eternal force field is exploited for their functionality[87], as in the former case, or if channel geometries and features, as well as hydrodynamic forces are employed, in the latter[88]. For instance, features like pillars, pores or channel shrinkages are developed in microfluidic devices based on size-based methods. As an alternative to these approaches, suffering for clogging and risk to damage analytes, other passive approaches based on hydrodynamic forces associated to analytes size and deformability properties are used in deterministic lateral displacement[89], pinched flow fractionation and inertial microfluidic devices.

Beyond these passive mechanisms, active approaches governed by forces derived from an external field, which can be electric, acoustic, magnetic or optic are preferred to passive ones, since they are characterized by higher efficiency and throughput. Indeed, forces allow to control analyte trajectories not only for sorting and delivery biomarkers to specific positions, but also to trap them. For instance, a non-uniform electric field governs the movement of biomarkers depending on their dielectric properties in dielectrophoresis devices, meanwhile a uniform electric field manages analytes deflection according to surface-to-charge ratio or isoelectric point in electrophoresis and in isoelectric microfluidic devices, respectively[69]. Seeing that the application of an external electric field can produce some unpleasant effects as joule heating and analytes damages, alternative approaches as magnetic- and acoustic-based microfluidic devices have been developed.

The application of an external non-uniform magnetic field reduces analyte damages and operation times. In addition, it doesn't require a physical contact between the magnet and the liquid, therefore magnetic forces are not influenced by ionic strength and pH solutions variations. Commonly, this approach is combined with an immunocapture technique to achieve a higher specificity.

Acoustic forces, derived from an acoustic pressure field, act on biomarkers mechanical properties as size, density and compressibility related to surrounded medium characteristics (i.e. viscosity and compressibility). Acoustophoretic devices are non-invasive and versatile, indeed they can be exploited either as continuous flow separation[90] or trapping tools[91].

Finally, optical forces[92], known as optical tweezing, allow to manipulate biomarkers exploiting a light radiation pressure without mechanical contact. Even if this approach is characterized by a high precision either concerning analytes motion and immobilization, it presents some critical aspects as analytes over-heating and over-exposure.

Despite progresses performed in microfluidic field in the las few years, each mechanism illustrated above for controlling the motion of biomarkers presents some disadvantages, asserting that additional improvements must be performed to employ microfluidic platforms in everyday use. Then, further work will be focused on combining different methods advantages to overcome critical aspects, involving new technology as 3D printing to develop multistep integrated microfluidic platforms characterized by simple, rapid and low cost configuration with high level of automations and high-throughputs.

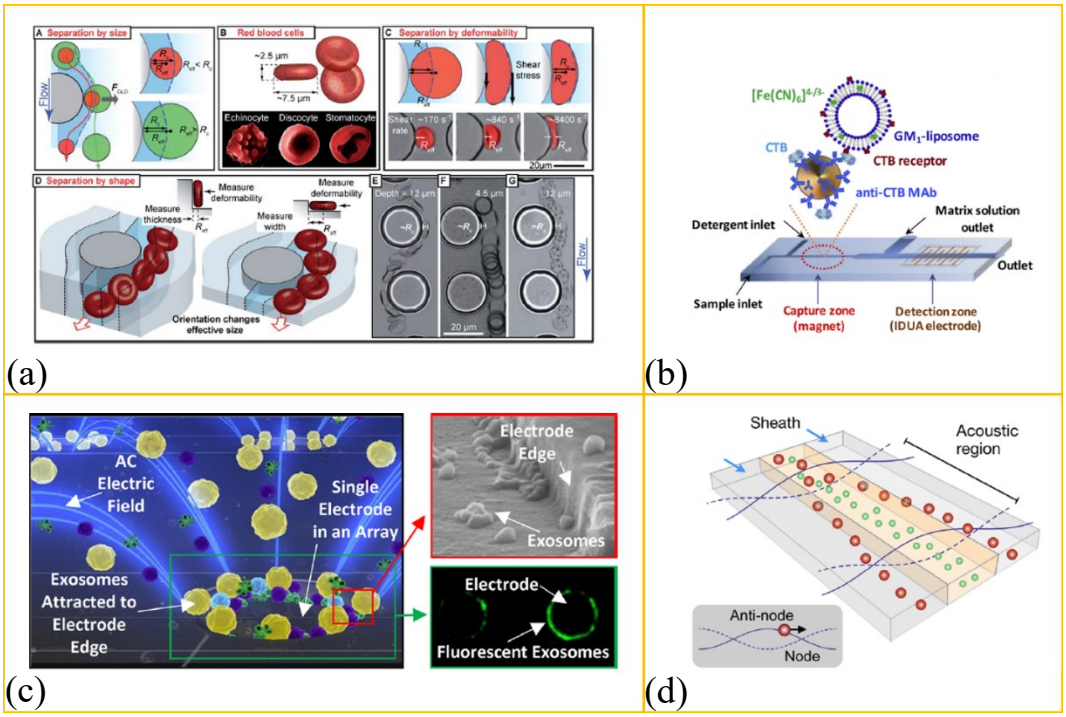

Figure 1.3.2 Examples of developed microfluidic devices: (a) Deterministic lateral displacement on red blood cells. Image from[89] (b) microfluidic device based on coated magnetic particles for biosensing. Image from[84], (c) alternating current electrokinteic microarray chip device. Image from[93] and (d) acoustic purification of extracellular microvescicles. Image from[90].

1.4 Aim of the work and thesis structure

As illustrated in the introductory section, the application of nanotechnologies to clinical and medical fields offers a great opportunity for the development of innovative options for the diagnosis and treatment of cancer disease. Indeed, the development of microfluidic devices, thanks to their characteristics, could overcome some drawbacks of traditional clinical approaches such as invasive tissue biopsy or expensive and dangerous screening tests that lack of selectivity and real-time monitoring.

In this context stand design, fabrication and characterization steps of microfluidic devices described in this thesis. In detail, the work described in this PhD Thesis is part of a wider project called "DEFLeCT" (Digital tEchnology For Lung Cancer Treatment) founded by Piedmont Region in the framework of "Health & WellBeing" Platform program. The aim of the project is the development of Lab-On-a-Chips and Organ-On-a-Chips for the early diagnosis and screening of lung cancer treatments. Results obtained during this thesis work are reported as follows.

Chapter 2 treats a novel 3D printed microfluidic device developed for the separation of biomarkers depending on their surface-to-charge ratio. Indeed, the separation between each type of analyte is performed throughout the application of an electric field inside the microfluidic chamber of the device. Thus, devices manufactured throughout a novel approach, an additive manufacturing method, are deeply investigated via morphological characterizations. Then, separation performances of the device, at different conditions, are evaluated either with synthetic and biological analyte solutions.

Chapter 3 illustrates the focalization potentiality of a silicon-based microfluidic device for the separation of biomarkers with micrometric dimensions. In this case, alternatively to the previous described device, samples are separated in the microfluidic channel by the presence of an acoustic field, which collects particles or cells according to their mechanical properties compared to the surrounded medium ones. Then, design and fabrication processes are reported, followed by focalization performance tests conducted either with synthetic particles and cells.

Chapter 4 depicts the third type of microfluidic device developed during this work. In detail, two PDMS-based microfluidic devices are introduced as valid tools for the capture of circulating microRNA biomarkers. Thus, characterization processes on channels morphology and chemical composition are illustrated as well as parameters for the automatized process. Then, the best working conditions at which is demonstrated the capture of microRNAs on microfluidic surfaces either with synthetic and a pool of microRNAs related to NSCLC are highlighted.

Finally, **Chapter 5** summarizes conclusions and reports future perspectives for the application of these microfluidic devices as LOC in liquid biopsy for the early diagnosis and detection of lung cancer.

Chapter 2

Micro-free flow electrophoresis device

2.1 Introduction

2.1.1 State-of-the-art of micro-free flow electrophoresis devices

In the last decades, the miniaturization upcoming trend and the development of LOC systems, as small portable devices and point-of-care diagnostic tools, has led to the development of micro-free flow electrophoresis (μFFE) devices. These tools characterized both by the advantages related to the dimensions scaling down and by the highly versatile approach are commonly used for preparative scale fractionation and separation of solid particles, organelles, cells, complex protein mixture, etc[94][95].

Starting from the first μFFE device fabricated in silicon through a standard micromachining process, nowadays the majority of μFFE devices are developed by exploiting various types of polymers through soft-lithographic approach or replica molding strategy (**Figure 2.1.1**). Indeed, even if the first μFFE device demonstrated its capability to separate different amino acids in a continuous manner, silicon possesses an inappropriate substrate for this type of application considering its low electric breakdown potential[96]. Moreover, among an adequate selection of proper materials and technological processes for the fabrication of μFFE devices, researchers had to face a critical aspect related to the miniaturization of free-flow electrophoresis: the formation of electrolysis bubbles generated by the application of an electric field during experiments.

As a first attempt, to overcome the electrolysis bubbles issue μFFE devices exploited solutions as membrane-likes arrays of channels patterned between the separation chamber and the electrodes channels[97], electrodes channel depth control[98], salt bridges[99][100][101] or electrostatic charge induction[102]. Nevertheless, these solutions were inadequate since they produced high fluidic resistances, therefore high electrical resistances leading to low voltage efficiencies. Thus, enhanced μFFE devices, characterized by ion permeable membranes manufactured through new technological processes as multistep liquid-phase lithography[103] and in situ polymerization[104][105] have been promoted. However, these enhanced devices were characterized by persistent potential drops as well as reduced chemical stabilities, then other approaches such as addition of surfactants [106] or organic solvents[107] have been evaluated. Despite buffers modifications, innovative features as integrated nanoporous membrane[108] and channel shrinkages between electrodes and separation channels[109][110] are now introduced in μFFE devices. To conclude, the last mentioned design innovation, characterized by simpler features, pave the way to the employment of 3D printing technology for manufacture μFFE devices[111], ensuring fast and cheap prototype developments for future works.

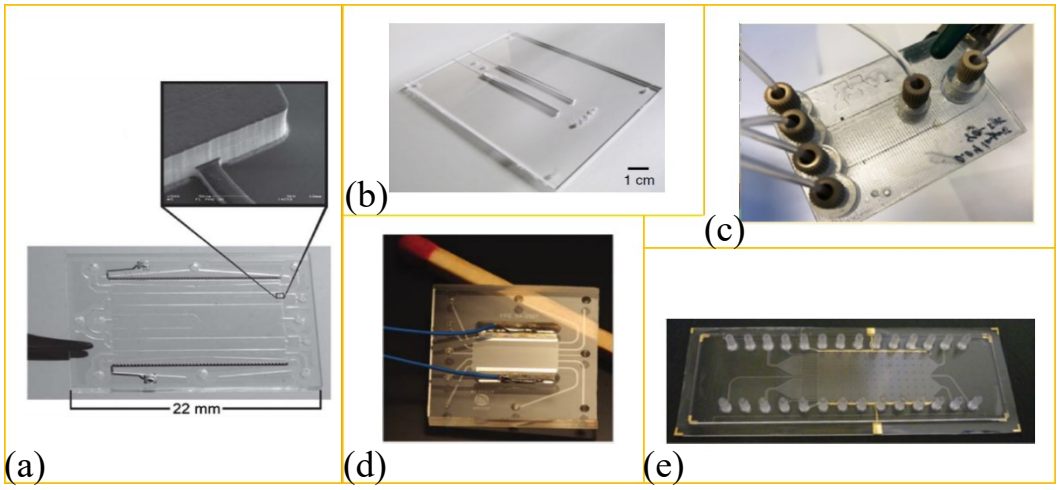

Figure 2.1.1 Examples of µFFE devices: (a) microfabricated electrophoretic enrichment chip with integrated platinum black electrodes, phaseguides and bubble-expulsion structures. Image from[104], (b) polymer-based chip. Image from[105], (c) 3D-printed chip. Image from[111], (d) microfabricated glass with integrated platinum electrodes and soldered electrical connections. Image from[100] and (e) cycloolefin polymer chip with integrated gold electrodes. Image from[110].

2.1.2 Micro-free flow electrophoresis theory

µFFE is a continuous and analytical separation technique used to separate chemical species and biomolecules in a flowing stream according to size-to-charge ratio when an electric field is applied perpendicular across a planar separation chamber. Commonly, µFFE devices are divided in four modes (**Figure 2.1.2**)[112][113][114]:

- *free-flow zone electrophoresis (FFZE)*: a thin sample stream is introduced into a planar separation channel with a buffer characterized by constant pH and electrical conductivity, thus charged analytes deflect laterally based on their electrophoretic mobility when the electric field is applied;
- *free-flow isoelectric focusing (FFIEF)*: sample compounds move into a buffer composed by ampholytes exploited to create a linear pH-gradient perpendicular to the flow direction. Thus, when the electric field is applied, analytes move into the pH-gradient until reaching their isoelectric point to be focused;
- *free-flow isotachophoresis (FFITP)*: sample analytes shift between a high mobility leading electrolyte and a low mobility trailing electrolyte compared to the analyte mobility. Therefore, when the electric filed is applied, analytes focus in adjacent regions that create according to their electrophoretic mobility.
- *free-flow field-step electrophoresis (FFFSE)*: a less conductive buffer is introduced into the centre of the separation chamber and it is enclosed by more conductive buffers leading to the formation of an electric field step gradient. Thus, analytes passing from a high electrical field strength, located in the central zone, to the lower field one can be concentrated.

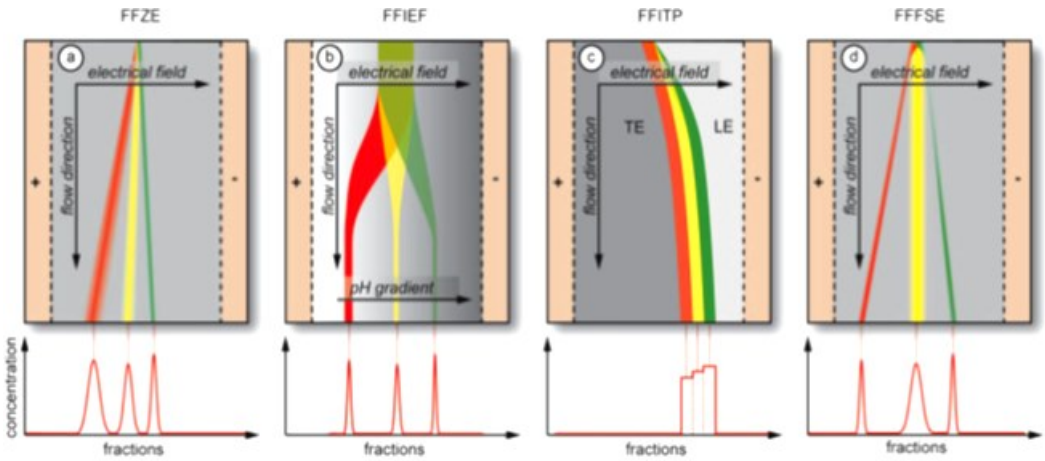

Figure 2.1.2 Modes of FFE: (a) FFZE, (b) FFIEF, (c) FFITP and (d) FFFSE. Image from[113].

Among these electrophoresis modes, FFZE is the separation approach selected for the fabrication of the μFFE device presented in this chapter. Indeed, it implied either a simpler design and less complex buffer solutions[113].

Thus, focusing on the background theory of the FFZE separation mode, one can determine the position where the analyte crosses the detection zone (d). Indeed, analytes deflect laterally under a constant angle depending on the applied electric field (E), analytes' mobility (μ_e) and the time spent by analytes inside the separation chamber (t) [112][113]:

(1) $$\boldsymbol{d = \mu_e E t}$$

Therefore, by varying the electric field or the buffer velocity it is possible to tune the position of an analyte sample to a precise place in the device. On the contrary, none of these parameters influenced the bandwidth, a fundamental parameter that must be considered to achieve a high resolution μFFE device. Indeed, the μFFE separation performance is influenced by several sources of band broadening (σ^2_{FFE}) derived from the width of the injected sample stream (σ^2_{inj}), diffusional broadening (σ^2_D), electrodynamic broadening (σ^2_{ED}), hydrodynamic broadening (σ^2_{HD}) and electrodynamic broadening (σ^2_{EHD})[98].

(2) $$\boldsymbol{\sigma^2_{FFE} = \sigma^2_{inj} + \sigma^2_D + \sigma^2_{ED} + \sigma^2_{HD} + \sigma^2_{EHD}}$$

Finally, combining the equation which predicts the band position **(1)** with the one that predicts the bandwidth **(2)**, one can define the resolution of a pair of streams as[112][113][98]:

(3) $$\boldsymbol{R_s = \frac{d_1 - d_2}{2(\sigma_1 - \sigma_2)}}$$

where 1 and 2 represent the pair of streams.

Thus, at lower buffer velocities the resolution scales linearly with the electric field and inversely with the square root of the buffer linear velocity, while the opposite behavior is observed at higher buffer velocities and deflection distances.

To conclude, the maximum achievable resolution occurs at low combination of electric field and buffer linear velocities, suggesting that the separation power should be maximized to spread the analyte streams across the full width of the separation chamber.

2.2 Materials and methods

2.2.1 Design

The bottom of the µFFE device was designed by a 3D computer aided design (CAD) software (Rhinoceros), which offers 2D and 3D design solutions in a unique environment, and files export in standard triangulation language (STL) format for the 3D printing process.

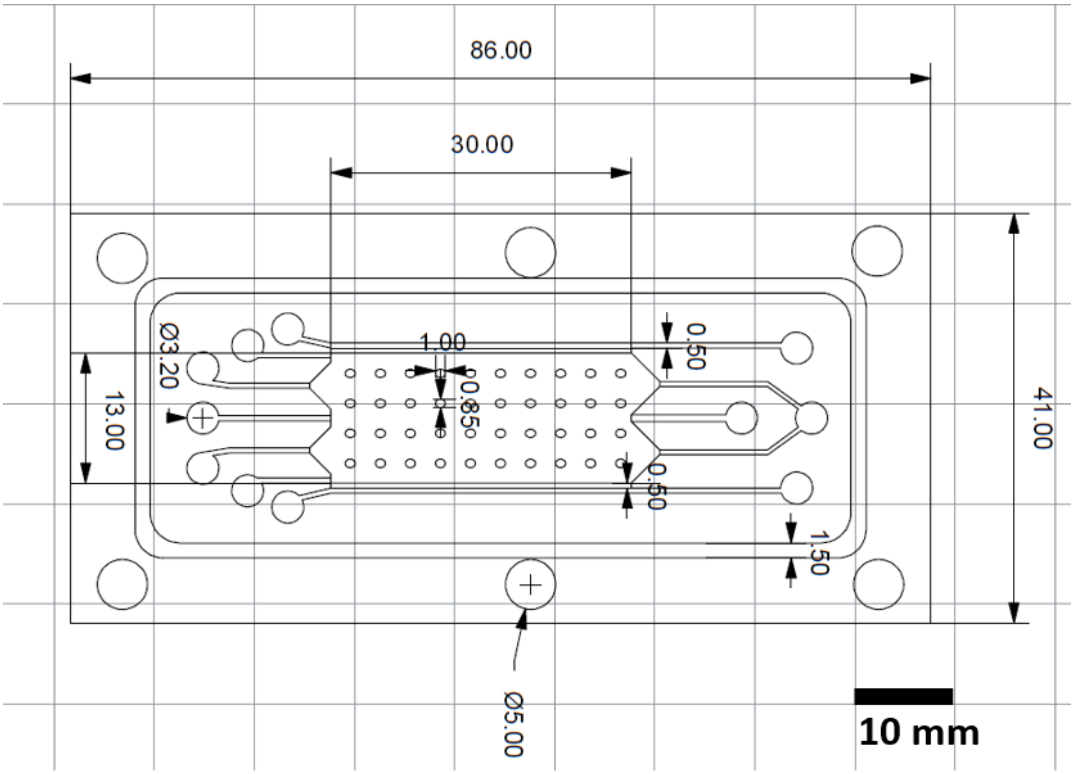

Figure 2.2.1 2D draw of the first µFFE device with nominal CAD dimensions.

Features	CAD (mm)		
	Length	Width	Height
Device	41.00	86.00	2.80
Separation chamber	30.00	13.00	0.10
Pillar	1.00	0.85	0.10
Inlet/outlet diameter	-	3.20	-
Inlet/outlet channel	-	0.50	0.50
Electrode channel	48.00	0.50	0.50
Partition bar height	30.00	0.05	0.50

Table 2.2.1 Features CAD dimensions of the bottom of the first µFFE device design.

As depicts in **Figure 2.2.1** the first design of the µFFE device was defined by the following dimensions: 41 mm in width, 86 mm in length and with a height of 2.80 mm. Detailed device's features dimensions are also reported in **Table 2.2.1**. The chip was characterized by a separation chamber, two electrode channels, an inlet for the buffer solution, one for the analyte solution and five outlets. In details, the separation chamber dimensions were 30 mm in length, 13 mm in width and 100 µm in height. Inlets and outlets, with 3.2 mm holes' diameter, were characterized by channels with a 500 × 500 μm^2 square sections. This square section layout was used also to design electrode channels, placed alongside the separation chamber, to facilitate the electrode wire insertion. Furthermore, around the device design was added a 100 µm deep and 1.5 mm wide trench to define the bonding area and prevent the microfluidics clogging during the sealing step of the chip as reported as follows. Finally, the first design of the µFFE device was characterized by six holes of 5 mm of diameter along the design borders to allow the clamping of the chip with a polymethyl methacrylate (PMMA) (PLEXIGAS®) holder through screws, in order to avoid solutions leakages between tubes and the device during experiments.

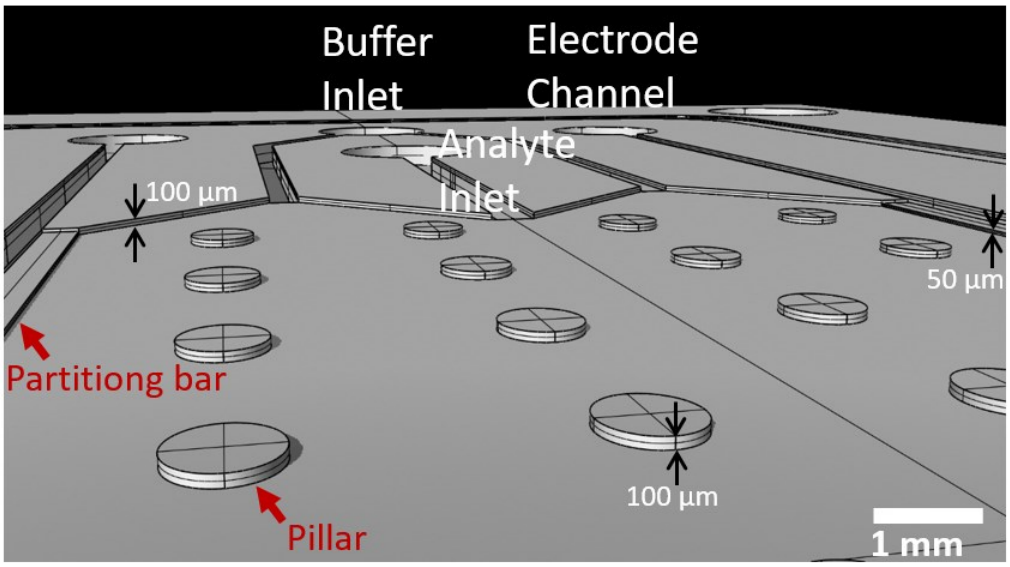

Figure 2.2.2 Inset of the separation chamber of the µFFE device with its characteristic features.

Figure 2.2.2 shows an inset of the µFFE device separation chamber. It was characterized by an array of 40 elliptic pillars with dimensions of 1 mm × 0.85 mm with a height of 100 µm. In details, they were settled in evenly spaced rectangular array imposing a distance equal to 3 mm from each pillar centre, both along longitudinal and transversal directions. The integration of these features inside the separation chamber accomplished two functions: as structural columns in order to avoid the collapse of the top cover after the sealing of the device and to promote a uniform solutions chamber filling during the experiment, thus pillars were used as flow guides [97][110].

Furthermore, the design was defined by characteristic features to prevent electrolysis and bubbles formation in the separation chamber when the electric field

was applied. To mediate the effect of this phenomenon on µFFE stream stability, as mentioned above, in recent years different solutions were presented in literature[110][109][105][102][104][99][101]. In this work, an open channel design was preferred to a closed one since it involved simpler fabrication and operation processes. Indeed, the open channel configuration operated without any physical barriers between the separation chamber and the electrode channels, without applying ion permeable membranes[105][104][101] or salt bridge connections[102][99] commonly used in the closed one.

Thus, characteristic features known as partitioning bars were integrated in the design between the separation chamber and the electrode channels. In details, these features were defined with dimensions equal to the separation chamber concerning the length and with a height equal to the half of it, thus equal to 50 µm. By exploiting these constrictions, bubbles were hindered to migrate from the main chamber to the electrode channels guaranteeing the laminar flow in the separation area, thus a stream stability, during the experiment [110][109].

Finally, the first µFFE design was replaced with an enhanced one to overcome some critical issues observed during preliminary tests performed with 3D printed devices (see **Appendix A** for first µFFE device fabrication and leakages tests). In details, the new enhanced design had the purpose to remove leakages located between the top of the device and the PMMA cover near inlet ad outlet ports where solutions were pumped into the separation chamber. To do this, interconnections characterized by ¼'' 28 Unified Fine (UNF) threaded fluidic fittings were directly integrated into the 3D design. In details, interconnections were designed on the bottom of the microfluidics side in correspondence to inlet and outlet device ports to ensure a stable connection with the polyurethane (PU) (SMC) and the device itself. As a consequence, the layout disposition of inlet and outlet channels changed in the enhanced design due to interconnection sizes, preserving the constraint to design a functional device employing the same working area of the first draft (**Figure 2.2.3**).

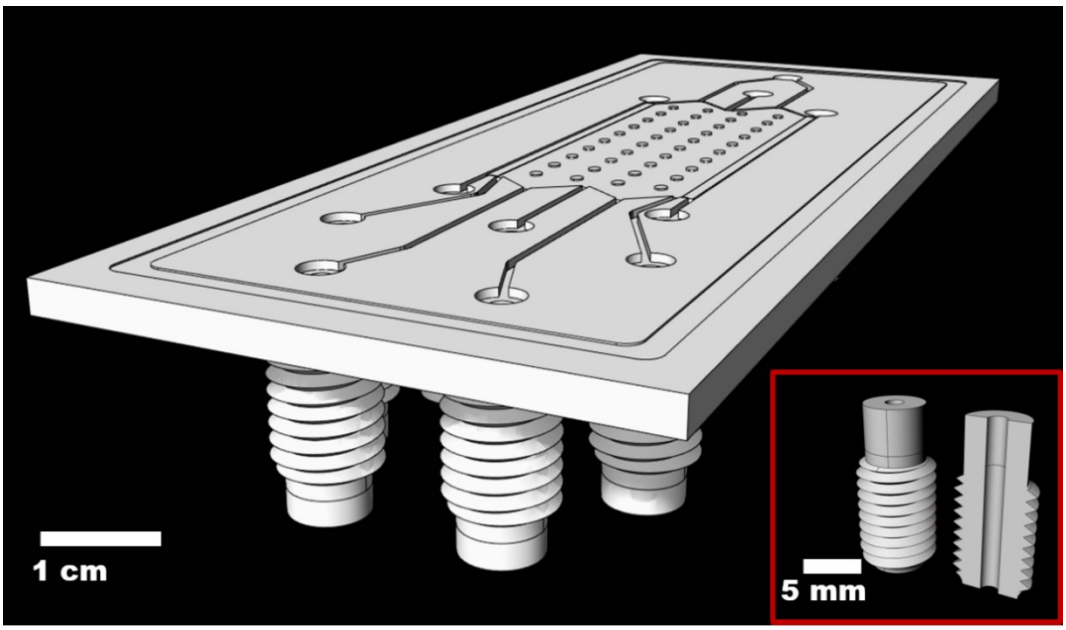

Figure 2.2.3 2D design of the enhanced device with an inset of the ¼'' 28 UNF threaded fluidic fittings in the red box on the right.

2.2.2 Device fabrication

The employment of an additive manufacturing process provided an excellent strategy for devices fast prototyping, reducing time and cost since it involved no cleanroom facilities as conventional micromachining technique, soft-lithographic or molding replica strategies. Furthermore, 3D printing allows an easy introduction of further design updates with limited re-work time since the CAD model salved in a STL format file was directly pre-processed by the 3D printer.

The µFFE device fabrication process can be outlined by the following steps: 3D microfluidics printing, electrode insertion and device sealing (**Figure 2.2.4**).

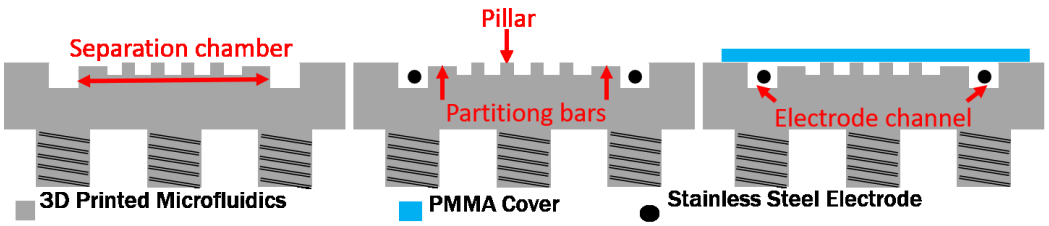

Figure 2.2.4 Fabrication process flow: 3D printed microfluidics, electrode insertion and device bonding.

During the first step, the microfluidics of the µFFE device, thus the bottom part of the chip, was fabricated by employing the 3D printing technique. To do this, the final 3D CAD model was converted in a STL file format and was pre-processed by the InkJet 3D printing system that converted the file into the machine's low-level language. In details, the bottom of the device was fabricated by employing the 3D printer Objet30, provided by Stratasys, based on the poly-jet® technology. It works like an inkjet printer that instead of using a common ink, employs a patented

photocurable ink. Thus, hundreds of nozzles in the printing heads, moving across the build tray, jet structural and support materials at the same time to create a thin single layer that was immediately cured by an ultraviolet (UV) light source, allowing to manufacture a fully polymerized object through a layer-by-layer deposition (**Figure 2.2.5**).

The Objet30 printer allows the building of 3D printed objects with two different types of surface finish: glossy or matte. The matte surface option introduces a complete cover and UV curing of the structural material with the support material, while the glossy one exploits only the necessary support material, ensuring cheaper and faster manufacturing and a smoother surface finishing of the microfluidic internal surfaces. In details, the microfluidics of the µFFE device and the threaded fluidic fittings were manufactured by using Verowhiteplus RGD835 resin as structural material and SUP705 resin as sacrificial one. To conclude, further devices were manufactured employing the glossy surface finished as reported in the following.

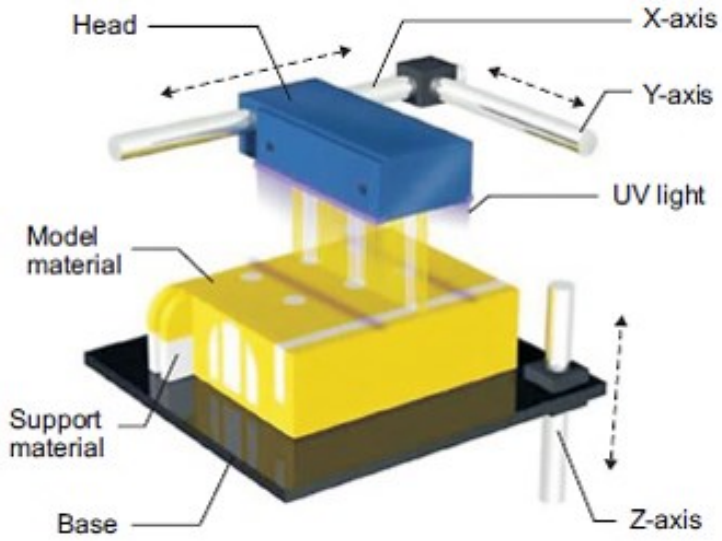

Figure 2.2.5 PoliJet® process (with the permission from[115]).

When the device was 3D printed, it was surrounded by structures made by the support material that was removed by using a water-jet station. Next, it was washed by isopropanol (Sigma-Aldrich) and flushed by a nitrogen flux as last cleaning step. After that, two stainless steel wire electrodes of diameter equal to 140 µm (The Crazy Wire Company) were manually inserted in the corresponding lateral channels. Finally, a 750 µm thick PMMA cover was used to seal the microfluidic chip. A slice with the same dimensions of the device was obtained using a paper cutter and it was cleaned by isopropanol and flushed by a nitrogen flux before bonding. A uniform and irreversible bonding between the 3D printed part and the PMMA slice was achieved by using as glue Poly(ethylene glycol) diacrylate (PEGDA) 575 resin (Sigma-Aldrich) mixed with 1% IRGACURE 819 (Sigma-Aldrich). In details, a thin layer of glue was spread near the microfluidics borders

and the glue overflow was collected in the trench located around the device border to prevent the clogging of the microfluidic area. Next, the PMMA slice was laid down on the microfluidics and the sealing was completed by clamping the whole structure inside as aluminium frame and baking for 20 min on a hot plate at 120 °C to obtain the full curing of the resin (**Figure 2.2.6**).

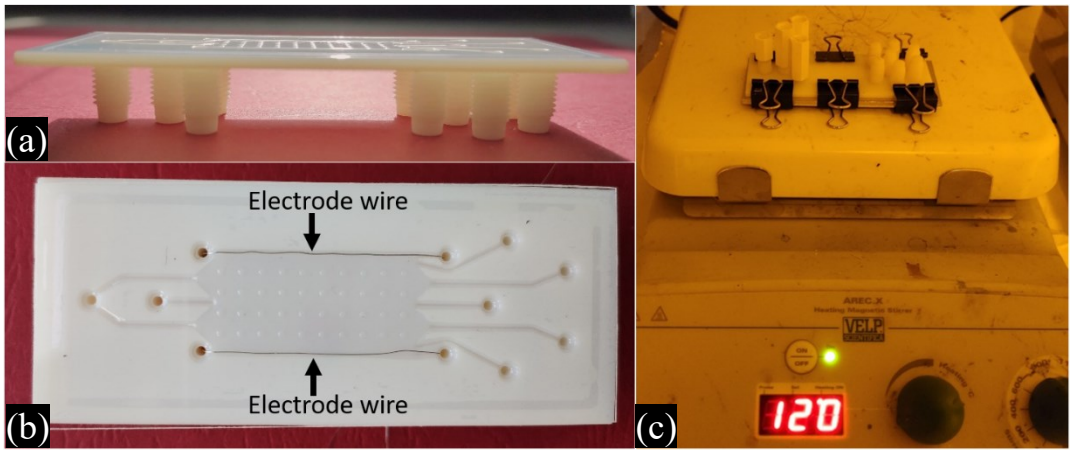

Figure 2.2.6 Micro free-flow electrophoresis (μFFE) device fabrication: (a) 3D printed microfluidics, (b) electrode insertion and (c) device sealing.

2.2.3 Experimental Setup

A customized experimental setup, composed by different elements, is depicted in **Figure 2.2.7**. A syringe pump system (Harvard Apparatus Pump33) was used to inject buffer and analyte solutions inside the microfluidic chip in a preliminary phase to evaluate system's leakages and then to perform field flow electrophoresis tests. In details, the pumping system drove the solutions flow rates, preloaded in plastic syringes (Terumo syringe, 2.5 mL), into PU tubes (OD = 2.0 mm, ID = 1.2 mm) connected to inlets via standard OmniLok fittings (Omnifit Labware) to the chip. To apply the electrical field in the separation chamber during the experiments a DC power supply (C4D HV 230 Sequencer) was employed. Thus, the voltage was applied to stainless steel wire electrodes setting the left electrode of the device to ground while a range of positive potentials was applied to the right electrode.

Before each experiment and between each run, the device was washed with a 70% ethanol solution (v/v) at a flow rate of 40 μL/min for 10 min and then rinsed twice with the buffer solution composed by 4-(2-hydroxyethyl)piperazine-1-ethanesulfonic acid (HEPES) 20 mM at 7.5 pH (Sigma-Aldrich) with the same flow rate and time settings.

Tests performed with micro and nanoparticles employed analytes dispersed in 20 mM HEPES containing: 4 μm fluorescent sulfated polystyrene micro particles (from now on called MPs) and 500 nm fluorescent carboxylated polystyrene nanoparticles (from now on called NPs) (FluoSpheres and Magsphere Inc. respectively). Analysing M/NPs datasheets the evaluation of maximum number of

MPs dispersed in HEPES was $5.68 \cdot 10^7$ particles/mL, while for NPs it was equal to $3.64 \cdot 10^8$ particles/mL.

Concerning µFFE experiments dedicated to biovesicles, exosomes (EXs) collected from fetal bovine serum (FBS, Sigma-Aldrich) through an overnight centrifugation process at 10^5 g at 4 °C were employed.

To conclude, during µFFE tests, a volume equal to 60 µL of analyte solution was dispersed into 555 µL of buffer solution volume.

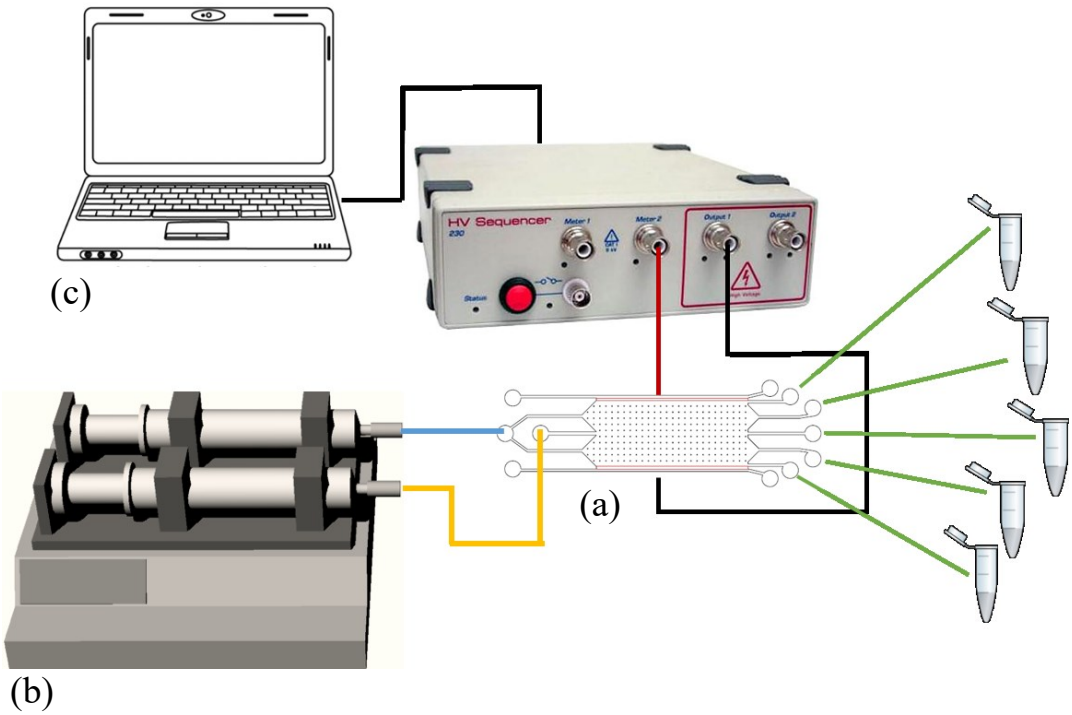

Figure 2.2.7 Experimental setup: (a) µFFE device sketch in which the yellow line is the solution containing the analyte, the blue one the buffer solution, red is the +V, black the ground electrode; and the green lines are the sample outlets; (b) the syringe pump system and (c) the power supply.

2.2.4 Device characterization methods

Features dimensions such as heights, lengths and widths of the 3D printed device were analysed to assess the accuracy of the chip evaluating the minimum feature sizes and the dimensions with respect to the CAD design. In details, the walls smoothness of 3D printed µFFE devices correlated to the CAD design was characterized and a comparison between the XY and Z resolutions was performed. In addition, the same characterizations were employed to compare the two surface finish types, to determine which was the best surface morphology to be selected for the chip manufacture.

A surface profilometer (Tencor P-10) was employed to characterize heights and surfaces roughness, while devices topography was evaluated through an optical microscope (Leica DVM2500). Finally, values and error limits were defined by

mediating four different printed devices of each type of surface finish, where on each device fifteen independent measurements had been taken for each feature.

2.2.5 Particles characterization methods

Hydrodynamic sizes and zeta potentials of M/NPs dispersed in 20 mM HEPES at 7.5 pH were characterized using the dynamic light scattering (DLS) technique with a Zetasizer Nano ZS90 (Malvern Instruments). Estimation of M/NPs sizes were based on how they scatter a light source, then a multiple narrows mode was applied as an analysis model. Instead, regarding the surface charge assessment the Cholesky model was applied.

M/NPs concentration at each outlet was quantified by ultraviolet−visible spectrophotometry (UV–Vis) (Multiskan GO Microplate Photometer Thermofisher Scientific). This technique is based on the Beer−Lambert law, which directly correlates the absorbance of the solution and the concentration of the M/NPs. To provide a correct quantification of particles concentration, thus calibration linear curves were obtained for each fluorescent wavelength. In detail, as reported from the MPs datasheet, they were analysed with a wavelength equal to 505 nm. Meanwhile, since for the NPs the manufacturer did not report that wavelength value, before performing the calibration curve it was necessary to characterize them by an absorbance spectrum using the UV−Vis instrument. Furthermore, M/NPs samples collected at the outlets where diluted in bi-distilled Water (MilliQ) to reach a minimum volume equal to 100 µL to perform the UV-Vis analysis and poured in different wells of the 48-microplate. Before performing the UV-Vis characterization they were shacked for 95 seconds to prevent particles sedimentation issues. At last, the quantification of particles concentration was defined avoiding the background signal from each read values.

EXs and EX/NPs samples employed for the µFFE experiments were characterized by nanoparticle tracking analysis (NTA, Malvern Panalytical instrument). By using this, particle size distributions and concentrations were determined exploiting the nanoparticles' Brownian motion in a liquid suspension lightened by a laser light source.

Finally, the percentage either of particles and exosomes collected from the µFFE device was determined as the ratio of percentage of elements concentrations at each outlet to the total elements concentrations collected at all five outlets [116]. For each set of tested analytes, experiments were repeated three times, thus error bars were reported according to the acquired data over the repetitions.

2.3 Results and discussion

2.3.1 Pillars characterization

Pillars dimensions were characterized by optical microscope images and surface profilometer measurements concerning XY and Z resolutions to evaluate the accuracy of the printer with respect to CAD values. These analyses were performed for devices printed either in the glossy surface finish mode and in the matte one. In details, observing **Figure 2.3.1**, pillars printed in the glossy device are more visible instead of the matte ones, since the surface was less rough than the other, allowing a more reflective topography to the impinging light source of the optical microscopy. Due to this, pillars manufactured through the glossy printing mode displayed a more defined shape in comparison with the matte ones.

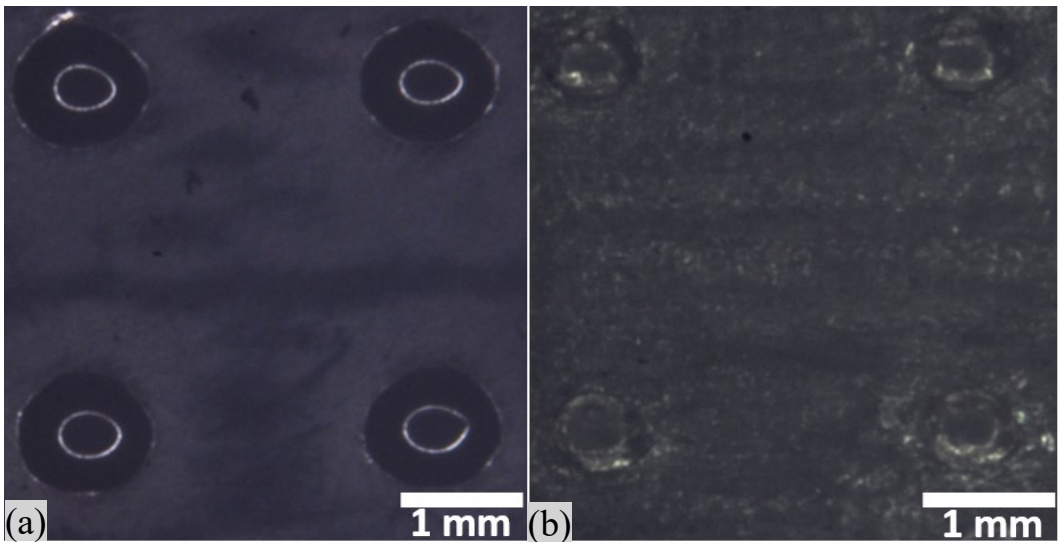

Figure 2.3.1 Optical microscope images: (a) pillars in the glossy surface device and (b) pillars in the matte surface device.

In detail, as depicted in **Figure 2.3.1**, in the glossy type device, pillar average dimensions were 1032 μm and 933 μm in length and width, thus larger values with respect to CAD ones of about 30 and 80 μm in length and width, respectively. On the contrary, pillar features in the matte device revealed narrower average values by hundreds of microns related to nominal ones. In fact, their average sizes were 725 μm in length and 603 μm in width.

Finally, only concerning pillar heights, both types of surface finish reproduced accurately the CAD values showing a discrepancy of 1 μm for the glossy type and 3 μm for the matte one.

Features	CAD (µm)	Glossy Surface (µm)	Matte Surface (µm)
Pillar length	1000	1032 ± 13	725 ± 56
Pillar width	850	933 ± 23	603 ± 33
Pillar height	100	99 ± 2	103 ± 33

Table 2.3.1 CAD pillar dimensions versus real values.

2.3.2 Partitioning bars and electrode channels characterization

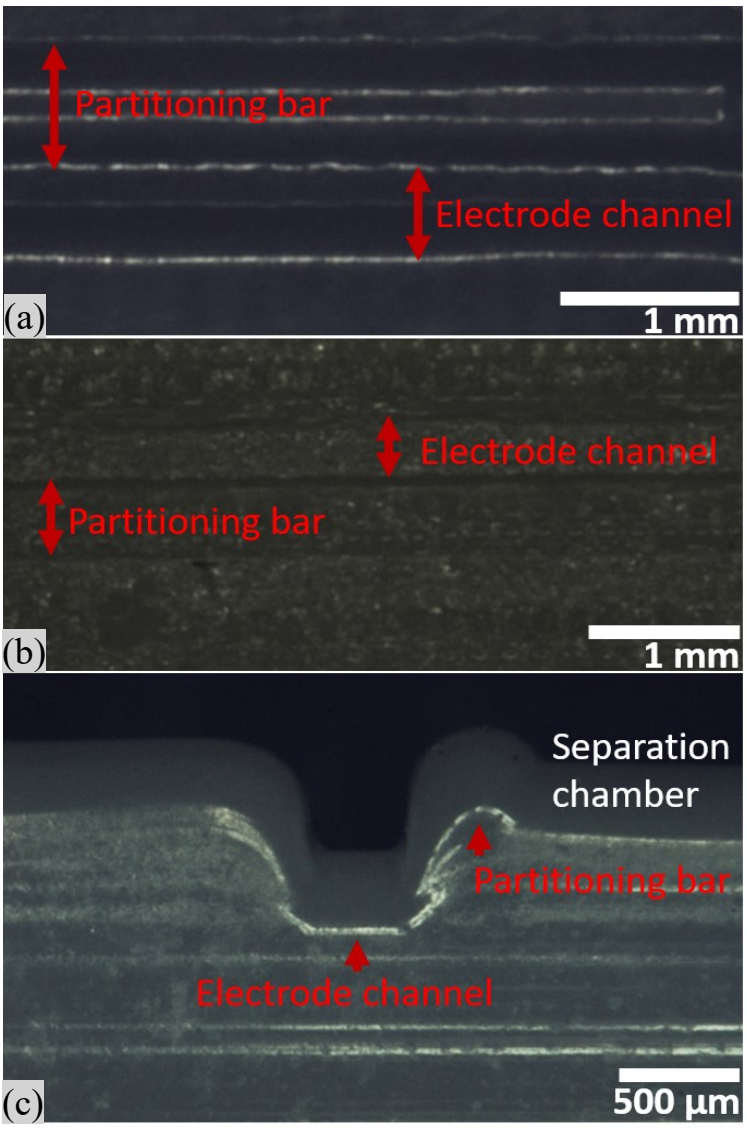

Figure 2.3.2 Optical microscope images: (a) partition bar and electrode channel in the glossy surface device, (b) partition bar and electrode channel in the matte surface device and (c) cross section of the glossy µFFE device, where the partition bar and electrode channel were highlighted.

From optical microscopy images (**Figure 2.3.2**), likes the previous case regarding pillar analyses, it was arduous to identify partitioning bar and electrode

channel features in the matte device due to the greater surface's roughness with respect to the glossy one. In fact, even if partition bars printed in the matte mode best fitted the CAD values, they resulted to be less visible from optical microscope characterization.

In details, as reported in **Table 2.2.1**, while the width average value of partitioning bars in the matte device differed by 24 μm with respect to CAD one, in the glossy printing mode they were reproduced with an error of 42 μm. A comparison between the two printing modes regarding partitioning bars heights indicated how the matte surface finish was the most accurate referring to the nominal value. Indeed, it was equal to 52 μm compared to the CAD value of 50 μm, while for the glossy features it was 55 μm. Finally, even if average values of the matte mode best represented CAD values, the emphasized surface's roughness in the matte features lead to a higher average mean error compared to the glossy one.

Both surface finish modes displayed similar average mean error only regarding electrode channel width dimensions. Indeed, these 3D printed features exhibited larger dimensions corresponding the nominal ones. The average value in the glossy surface finish was 612 μm, while for the matte one it was 577 μm.

Features	CAD (μm)	Glossy Surface (μm)	Matte Surface (μm)
Partitioning bar width	500	458 ± 15	524 ± 30
Partitioning bar height	50	55 ± 2	52 ± 8
Electrode channel width	500	612 ± 31	577 ± 33

Table 2.3.2 CAD partitioning bars and electrode channel dimensions versus real values.

2.3.3 Inlet/Outlet ports characterization

Inlet and outlet features presented an emphasized reproducibility referring to the CAD dimensions depending on the surface finish type used. In fact, while these features in the glossy device were printed with a 4% accuracy compared to the CAD dimensions, with the matte option this value was 21%, thus five times greater. The average values of both surface finish types were shorter than the nominal ones, in details, it corresponded to 3090 μm for the glossy type and 2519 μm for the matte one (**Table 2.3.3**). Finally, as reported before, the glossy features presented a more defined shape as illustrated in the optical image characterizations (**Figure 2.3.3**).

Features	CAD (μm)	Glossy Surface (μm)	Matte Surface (μm)
Inlet/outlet diameter	3200	3090 ± 195	2519 ± 81

Table 2.3.3 CAD inlet/outlet ports dimensions versus real values.

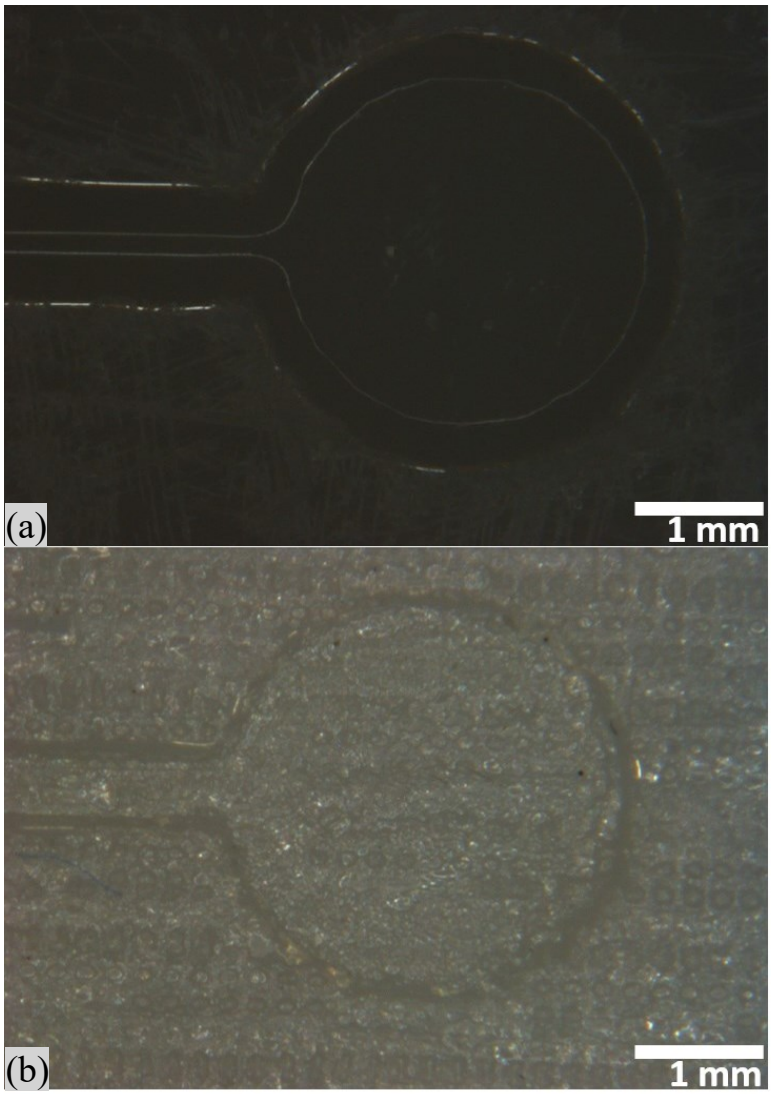

Figure 2.3.3 Optical microscope images: (a) inlet port in the glossy surface device and (b) inlet port in the matte surface device.

2.3.4 Surface roughness characterization

As depicted from previous features characterizations, concerning optical microscope images (**Figure 2.3.1**, **Figure 2.3.2**, **Figure 2.3.3**), a relevant roughness was observed in the matte device. In fact, due to the huge roughness, not only was difficult to distinguish features such as pillars and partitioning bars into the device, but also it induced a higher variability regarding the reproducibility of those features in the matte surface finish. Then, to achieve an estimation of surfaces roughness concerning both surface finish types, profilometer analyses were performed. In details, as reported in **Table 2.3.4**, the roughness of the matte devices was ten times greater with respect to the glossy ones. Thus, since the huge roughness of the matte device can determine some surface dependent phenomena, such as perturbing the flow profiles or causing localized pressure differences, the

glossy surface finish mode was definitively employed for separation tests also because it reproduced more faithfully the CAD design dimensions.

Finally, the 3D printed glossy devices reported in this work presented a better accuracy and final resolution with respect to the previous published device manufactured through the FDM printer [111].

Features	Glossy Surface (µm)	Matte Surface (µm)
Roughness (Ra)	0.06 ± 0.02	0.50 ± 0.20

Table 2.3.4 Roughness values of glossy and matte 3D printed devices.

2.3.5 Particles analysis

M/NPs and EXs hydrodynamic sizes and surface charges average values were analyzed before performing µFFE tests.

According to datasheet values, MPs hydrodynamic size value was 3.9 µm while NPs average size value was 500 nm (**Figure 2.3.4**).

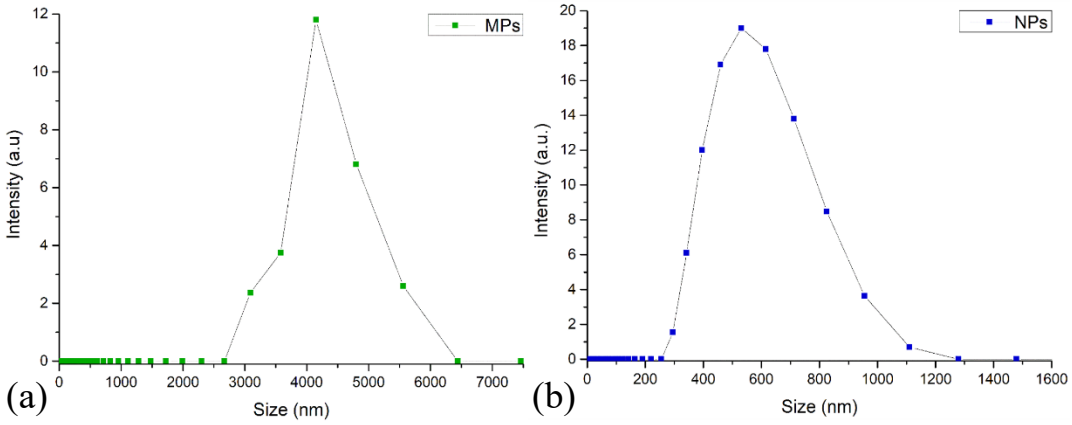

Figure 2.3.4 Dynamic light scattering (DLS) measurements of MPs (a) and NPs (b).

Concerning EXs analyses, both DLS and NTA characterization methods showed EXs to have a uniform and narrow size distribution, with 130 nm as most frequent value. In addition, NTA measurements allowed to quantify an EXs average concentration equal to $1.76 \cdot 10^{10}$ particles/mL (ranging from $1.64 \cdot 10^{10}$ up to $1.88 \cdot 10^{10}$ particles/mL), while DLS analysis provided an average zeta potential value of -9.6 mV.

Finally, in order to simulate EXs behaviour when the electric field was applied into the separation chamber, MPs and NPs employed in preliminary µFFE experiments were chosen with negative surface potential values similar to EXs ones. Due to this, MPs and NPs were selected having zeta potential of -12.2 mV and -18.9 mV, respectively (**Table 2.3.5**).

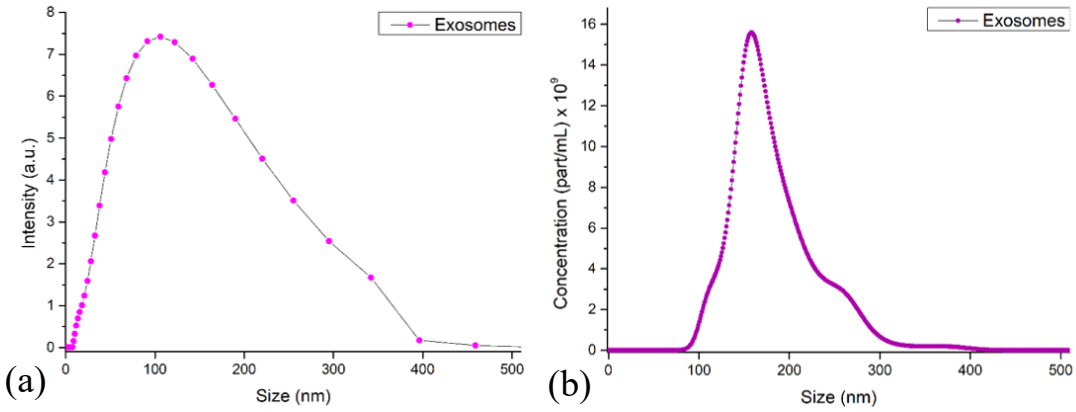

Figure 2.3.5 Exosomes size measurements: (a) Dynamic light scattering (DLS) analysis and (b) Nanoparticle tracking analysis (NTA).

Sample	Zeta Potential (mV)
MPs	-12.2 ± 1.9
NPs	-18.9 ± 1.4
EXs	-9.2 ± 1.0

Table 2.3.5 DLS zeta potential measurements.

An additional characterization on NPs dispersed in HEPES was performed to define the wavelength value to set during the UV-Vis analysis. Thus, an absorbance spectrum was executed between 280 nm and 430 nm through the UV-Vis instrument. As illustrated in **Figure 2.3.6**, NPs showed a maximum at 297 nm.

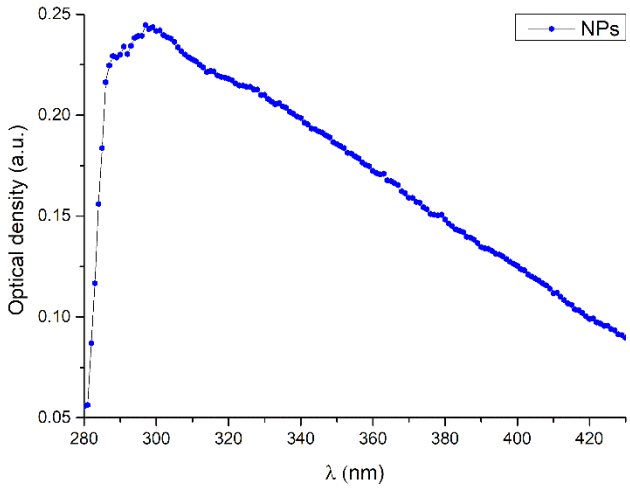

Figure 2.3.6 Optical density of 500 nm carboxylated NPs.

Finally, as reported before, to provide a correct quantification of particles concentrations at each outlets, linear calibration curves were determined for each class of M/NPs dispersions. In details, knowing the initial concentration of M/NPs

batches, a series of defined dilutions were prepared. From these absorbance values, after having subtracted the background signal, it was possible to achieve a correlation between the absorbance of the dispersion and the M/NPs concentration by applying a liner fitting for the evaluation of the regression equation.

Figure 2.3.7 reports linear calibration curves of MPs and NPs dispersions, with relative correlation coefficients R^2. These values provide a statistical measure of how well the regression equations approximate the real data points and when R^2 value was equal to 1 a perfect regression prediction fitting with data was achieved. In details, for the MPs dispersion R^2 was 0.9998 while for NPs one it was 0.9956. Thus, since R^2 value either for MPs and NPs was near to 1, it expressed that regression equations fit properly with the data.

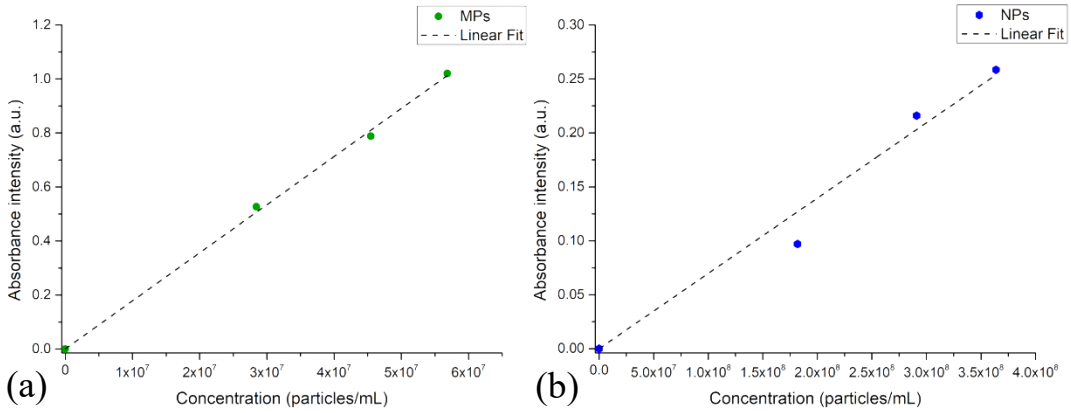

Figure 2.3.7 Calibration curves: (a) MPs regression equation $y = 1.78 \times 10^{-8}x$, (b) NPs regression equation $y = 6.98 \times 10^{-10}x$.

2.3.6 Flow confinement test

Focusing on the µFFE device design, buffer inlet channels were sketched to surround the analyte channel in order to forward the analyte solution in the centre of the separation chamber during experiments and to control the injected stream width. Then, tests were carried out to evaluate the optimal flow rate value to obtain the buffer flow confinement. In details, tests were performed by using HEPES 20 mM as buffer solution and an orange food dye diluted in HEPES 20 mM as analyte.

At the beginning, analyte and buffer flow rates were imposed equal, then the buffer flow rate was doubled with respect to the analyte one. Therefore, the buffer confinement was verified both at 1:1 and at a 2:1 buffer:analyte flow rate ratio. Observing **Figure 2.3.8** it is possible to notice how an increase of the buffer solution flow rate value induced a narrower flow confinement effect, leading to a high µFFE separation performance. Finally, to perform µFFE tests within 10 min, the best performance for the buffer confinement was verified at 20 µL/min for the buffer

solution and 10 µL/min for the analyte one, then these values were used as flow rates for further experiments.

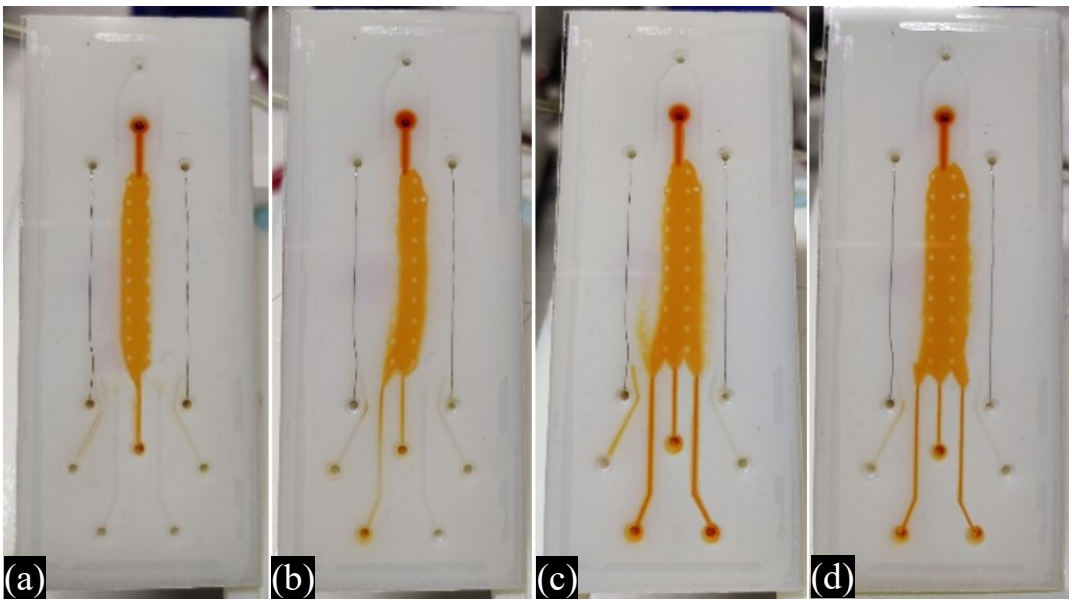

Figure 2.3.8 Optical photograph of the buffer flow confinement into the separation chamber: (a) buffer flow rate 20 µL/min and analyte flow rate 10 µL/min, (b) buffer flow rate 10 µL/min and analyte flow rate 10 µL/min, (c) buffer flow rate 10 µL/min and analyte flow rate 5 µL/min and (d) buffer flow rate 5 µL/min and analyte flow rate 5 µL/min.

2.3.7 Micro and Nanoparticles test

Firstly, MPs were dispersed in HEPES 20 mM and concentrated at 5.68×10^7 particles/mL. They were inserted in the µFFE device from the analyte inlet where they were successfully deviated in the separation chamber by the application of the electric field. Then, samples collected at different outlets were characterized by UV-Vis analysis, as described previously.

Preliminary tests investigated a range of applied voltages (ΔV) to set to the electrodes to define the optimized ΔV value to perform a significant MPs deflection into the µFFE device. Due to this, **Figure 2.3.9** illustrates the percentage of MPs observed at each outlet at a defined ΔV. Thus, at $\Delta V = 0$, when there was no electric field into the separation chamber, all MPs were collected in the central outlet (outlet#3) due to the buffer flow confinement effect, as expected. Whereas, increasing ΔV value at electrodes involved an enhancement of MPs collection at the external outlet (outlet#1) near the V+ electrode. This attraction derived from the fact that MPs were characterized by negative surface charges resulting in an average value of -12.2 mV. Thus, for voltages equal or higher than 40 V MPs were mostly found in the external outlet (outlet#1), instead a MPs spreading from the central outlet (outlet#3) to the external one (outlet#1) was detected at $\Delta V = 30$ V. In fact, in correspondence of this voltage value, MPs were found in three outlets (outlet#3, outlet#2, outlet#1) at concentrations equal to 47%, 16% and 37% respectively.

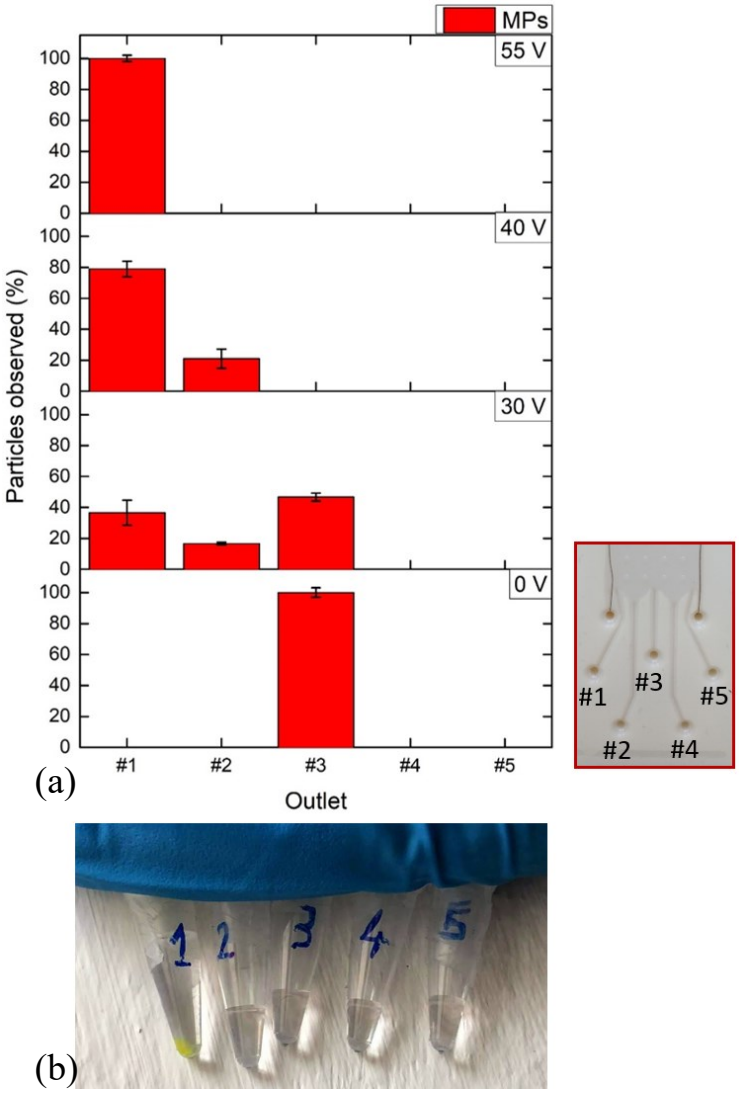

Figure 2.3.9 MPs collections at the outlets of the glossy μFFE device by setting a buffer flow rate of 20 μL/min and an analyte flow rate of 10 μL/min for 10 min: (a) MP outlets collections for ΔV = 0, 30, 40, 55 V where the corresponding outlets are reported in the red box on the right and (b) optical photograph of outlets collected when 55 V were applied to the electrodes.

After that, the μFFE device performance was evaluated with a mixed population of M/NPs, composed by a 1:1 MPs:NPs ratio, characterized by different sizes and negative surface charge values as reported before. Results accomplished with the mixed population reported a similar trend with respect to experiments conducted with MPs as illustrated in **Figure 2.3.10**. The final distribution of the M/NPs are reported as a function of the different applied voltage/outlet. In details, M/NPs distributions were analysed for the following ΔV values: 30 V, 35 V and 40 V. At a lower voltage value of 30 V, M/NPs were mostly collected both in the external outlet (outlet#1) and in the central one (outlet#3). Then, a partial shift of particles collection was observed at 35 V, where particles were mostly found in the outlets near the +V electrode (outlet#1 and outlet#2). Indeed, the 49% of MPs and 74% of NPs were detected at outlet#1. Finally, when 40 V were applied to the

electrodes, the majority of particles, 79% for MPs and 100% concerning the NPs were collected in the external outlet (outlet#1).

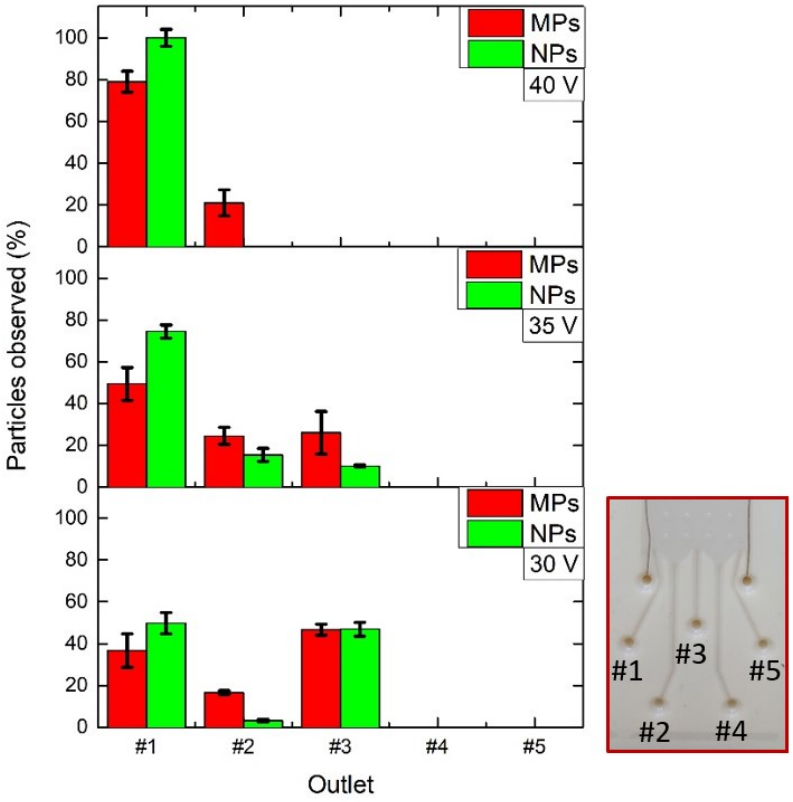

Figure 2.3.10 M/NPs collections at the outlets of the glossy µFFE device by setting a buffer flow rate of 20 µL/min and an analyte flow rate of 10 µL/min for 10 min: M/NPs outlets collections for ΔV = 30, 35, 40 V. The corresponding outlets are reported in the red box on the right.

To end, a further proof of the µFFE device performance was given by calculating the collected number of M/NPs at outlet#1, outlet#2 and outlet#3 when different voltages were applied to the electrodes (**Figure 2.3.11** and **Figure 2.3.12**). Focusing at outlet#1 and considering the exact residual volume of solutions collected at different applied voltages, on the basis of the linear calibration curve, it was possible to determine the collected number of particles (**Figure 2.3.11**). In detail, the number of M/NPs increased proportionally with the applied voltage at the electrodes up to 40 V. At a higher voltage, ΔV = 55 V, a drift toward the electrode channel occurred. This was determined by comparing the number of M/NPs collected at outlet#1 when 55 V were applied at the electrodes to the number of M/NPs of the initial 100% concentrated solution normalized by each specific particle calibration curve. Results reported this ratio to be equal to 87% for MPs and 84% for NPs. This is because a little amount of particles passed over the partition bars toward the +V electrode channel.

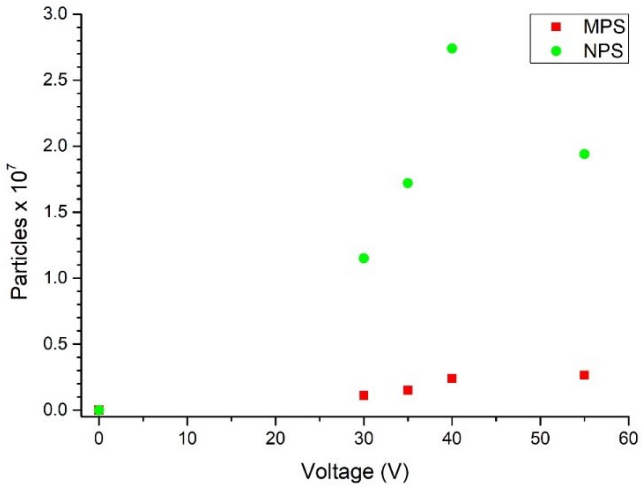

Figure 2.3.11 Number of M/NPs collected at outlet#1 when ΔV = 0, 30, 35, 40, 55 V were applied at the electrodes.

These results demonstrated the ability to modulate the percentage of particles observed as a function of the applied electric field. In addition, considering the amount of M/NPs diluted in the buffer solution during the device loading, it was possible to consider and evaluate the reconcentration of M/NPs by calculating the number of particles at the outlets with respect to the collected volume. A maximum 8.3× reconcentration factor of the M/NPs was obtained at 40 V. These are encouraging results that demonstrate the versatility of the device to tune the concentration of a M/NP population at a specific outlet in a reduced microliter range volume.

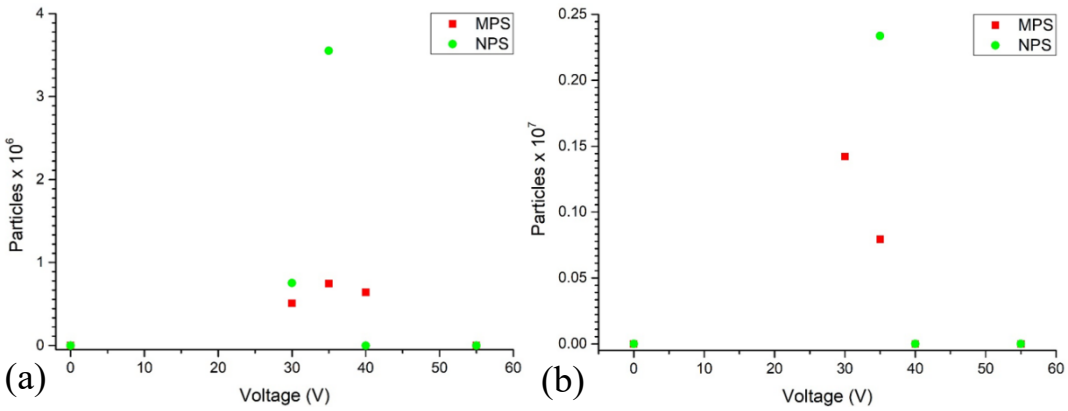

Figure 2.3.12 Number of M/NPs collected when ΔV = 0, 30, 35, 40, 55 V were applied at the electrodes: (a) outlet#2 and (b) outlet#3.

2.3.8 Biological test

The μFFE biological tests were performed firstly with EXs as analyte solution and then with a mixed population of EXs and NPs. **Figure 2.3.13** shows the percentage of EXs observed at the different applied voltage/outlets. At lower voltage value of 30 V EXs were mostly collected at the outlet#2 with a percentage equal to 89%. A similar trend was obtained applying 35 V at the electrodes were the 80% of EXs were found in the outlet#2. Moreover, at this applied voltage, a partial deflection of EXs to the external outlet (outlet#1) was detected. In fact, the number of EXs collected in that outlet (outlet#1), increased from 2% to 10% when 30 V and 35 V were applied to the electrodes, respectively.

Afterwards, a notable shift of EXs collection was observed at $\Delta V = 40$ V, where the 33% and 46% of EXs were found in the outlet near the +V electrode (outlet#1) and in the central outlet (outlet#3), respectively. A possible reason of why EXs at 40 V were located in the central outlet (outlet#3) could be given by the fact that this voltage can damage EXs thus inducing a variation in their properties, such as their morphological aspect or their surface characteristics. In fact, structural changes or degradations of EXs have been already observed in other isolation methods such as ultracentrifugation or depending on their storage and working temperature conditions [117][118].

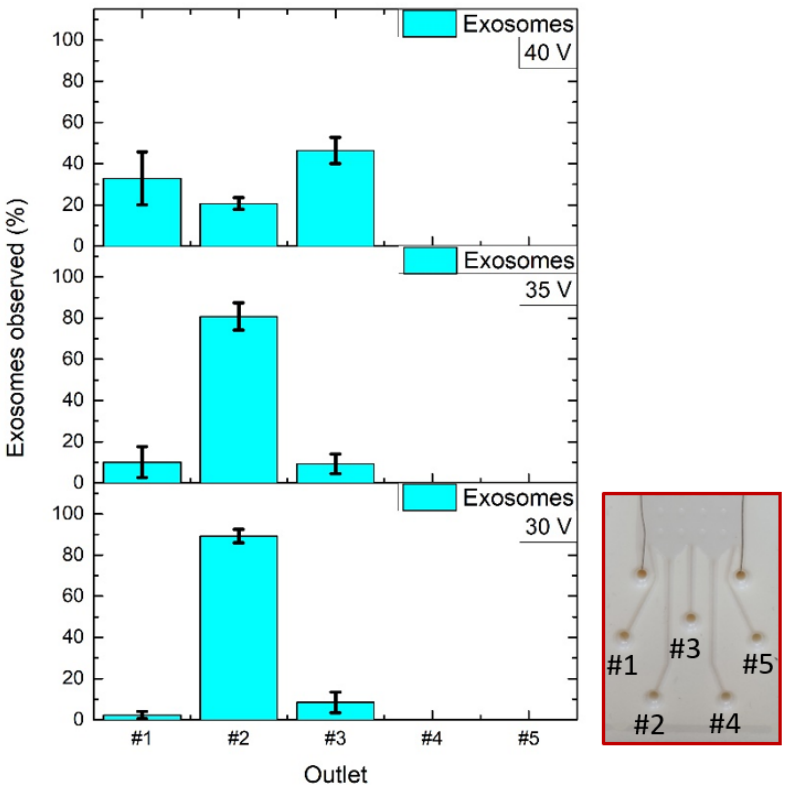

Figure 2.3.13 Exosome (EXs) collections at the outlets of the glossy μFFE device by setting a buffer flow rate of 20 μL/min and an analyte flow rate of 10 μL/min for 10 min when ΔV = 30, 35 and 40 V were applied at the electrodes. The corresponding outlets are reported in the red box on the right.

During EXs experiments performed at 40 V, while NTA size analyses on EXs collected at the outlet#2 and outlet#1 presented same dimensions of those inserted at the analyte inlet, EXs found at outlet#3 showed samples characterized by different dimensions. In details, in the central outlet (outlet#3) were found bigger EXs possessing a double size average value with respect to those found at the outlets (**Figure 3.3.14**).

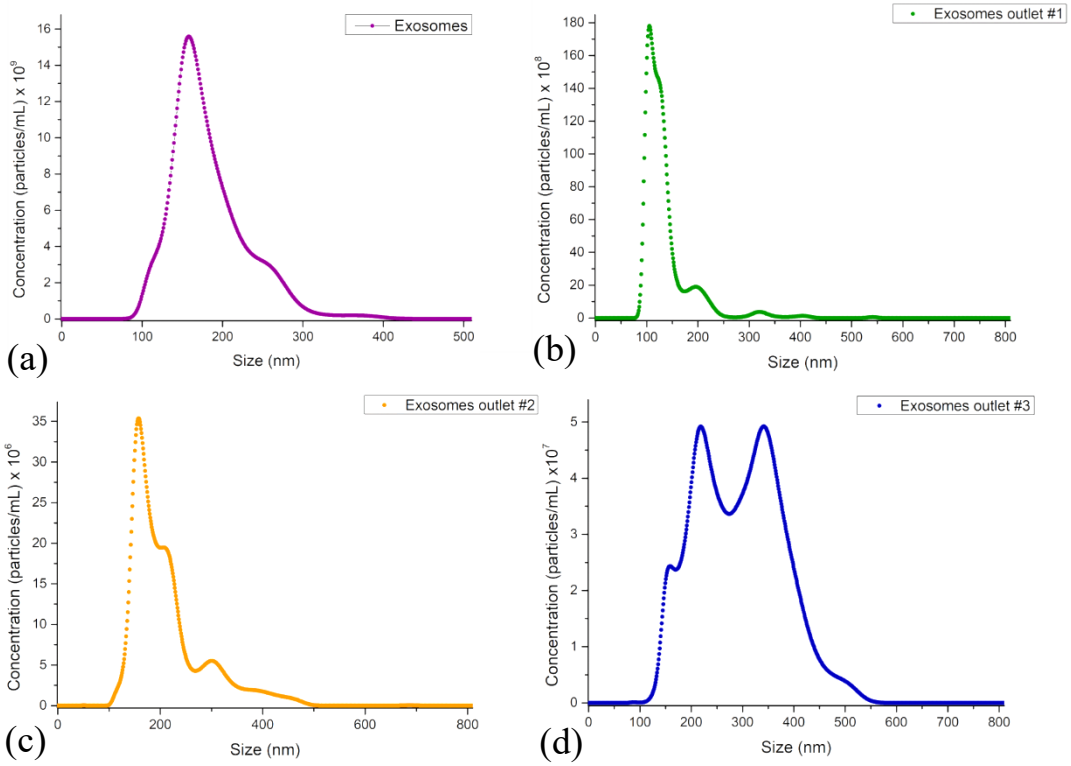

Figure 2.3.14 Exosomes NTA analyses: (a) EXs inserted into the µFFE device, (b) EXs collected at outlet #1, (c) EXs collected at outlet #2 and (d) EXs collected at outlet #3.

Finally, a preliminary test was performed with a mixed population composed by EXs and NPs in 1:1 EXs:NPs ratio. **Figure 3.3.15** reports the EXs and NPs percentages observed when 30 V were applied at the electrode. In detail, the majority of EXs, equal to 53%, were collected at outlet#2 while the majority of NPs observed, corresponding to 45%, were found at the outlet near the +V electrode (outlet#1), thus demonstrating the µFFE performance both with synthetic and biological samples.

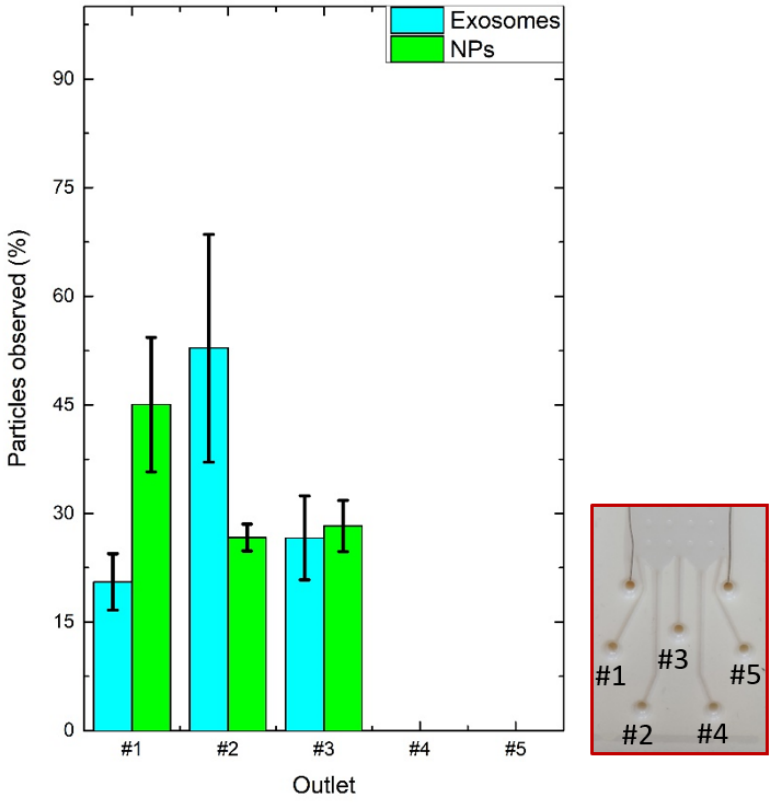

Figure 2.3.15 EXs and NPs collections at the outlets of the glossy μFFE device by setting a buffer flow rate of 20 μL/min and an analyte flow rate of 10 μL/min for 10 min when ΔV = 30 V were applied at the electrodes. The corresponding outlets are reported in the red box on the right.

2.4 Conclusion

In this work we evaluated the manufacturing process and the particle deviation performance of a μFFE 3D printed LOC. 3D printing technology allows the exploitation of low-cost materials and an easy introduction of further design updates with limited re-work time. Due to this, modifying a preliminary design, an enhanced 3D printed microfluidic device, characterized by threaded fluidic fittings integrated on the microfluidics backside in correspondence to inlet and outlet accesses, was developed.

Devices were manufactured employing two different types of surface finish: the glossy and the matte one. Thus, to evaluate which was the best choice, features dimensions such as lengths, widths and heights were deeply investigated through optical and profilometer analyses and compared to the CAD dimensions. Finally, glossy surface finish was selected to manufacture μFFE devices for separation tests, since their features were reproduced with a 5% accuracy related to the CAD dimensions and surface roughness was negligible with respect to features dimensions.

A novel approach was proposed for the μFFE performance assessment using M/NPs dispersed in HEPES characterized by different dimensions, surface charges and fluorescent dyes. Following this, it was possible to quantify the M/NPs collection at each outlet by exploiting UV−Vis technique, when different voltages at the electrodes were applied. Thus, demonstrating the possibility to tune the concentration of a population of either single and different species of MPs and NPs in a specific outlet at a defined voltage by accumulating them in a microliter volume range. These propaedeutic experiments allowed for successful preliminary biovescicles tests using FBS EXs. Finally, a preliminary test was performed with a mixed population composed by EXs and NPs demonstrating the μFFE performance both with synthetic and biological samples.

Further work will be focused on redesign the μFFE layout since it presented a limited number of outlets. In addition, to optimize particles or biological samples separation and concentration, the investigation of fine ΔV tuning and testing device's performance with different solutions and pH buffers will be executed.

Chapter 3

Bulk acoustic wave device

3.1 Introduction

3.1.1 State-of-the-art of bulk acoustic wave devices

In recent years, acoustophoresis has been applied in many challenges in biomedical research, as clinical and diagnostic fields[119][120]. Indeed, the utilization of ultrasounds in microfluidic systems generate forces that can separate or trap particles and cells, gain the control of their trajectories or encapsulate them in droplets[80][121][122]. By this approach, particles subjected to an ultrasonic field, generated via bulk acoustic waves (BAW) or surface acoustic waves (SAW), scattered or are impinged by field waves, allowing the creation of an acoustic radiation force able to move particles towards the surrounding medium (**Figure 3.1.1**)[123][124].

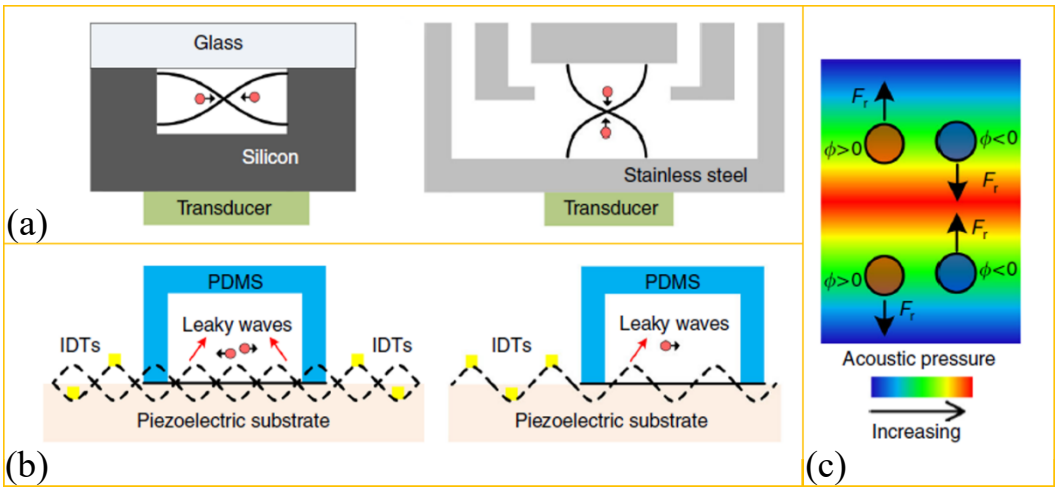

Figure 3.1.1 Acoustophoresis: (a) Bulk acoustic wave devices, (b) Surface acoustic wave devices and (c) illustration of acoustophoresis working principles. Image from[123].

BAW devices are promising tools to separate blood components throughout a continuous and a biocompatible approach, mainly due to their simply design and high throughput characteristics. Preliminary studies on BAW devices performed with micro particles of different sizes demonstrated their separation performances either in water-based[116][125][126] and whole blood solutions[127][128]. Then, following these promising results, further BAW devices displayed high separation efficiencies by analysing lipids[129], erythrocytes[130], platelets[131] and mononuclear cells (i.e. lymphocytes and monocytes)[132] from whole blood. Separation of red blood cells from plasma allowed the application of BAW devices in clinical practice as blood washing or plasmapheresis[133].

Regarding diagnostic tools, BAW devices proved their application by discriminating dead cells from live ones[134]. Then, high performances resulted either for separating and concentrating different tumor cells from blood[135] or

white blood cells[136], as well as mammalian cells from mixtures of healthy and apoptotic cells[137] handling the same chip.

Finally, BAW devices validated their roles also throughout the identification of pathogens and sepsis diagnosis. For instance, *Escherichia coli* separation and enrichment from blood samples has been already demonstrated by different BAW devices[121][138]. Moreover, these latest devices, exploited acoustic forces to trap analytes, allowing to perform PCR-based[139][140] or bacteriophage-based luminescence[141] assays in the same microfluidic platform.

3.1.2 Bulk acoustic wave theory

Commonly, the acoustic radiation force is divided into two components: primary and secondary radiation forces. Meanwhile primary forces derive from the interaction between the incident wave and particles in the suspended medium, second ones in contrast to the primary force, refer to scattered wave interactions with other particles[142][119] [143].

Since in this chapter a BAW device able to separate cells, micro and nanoparticles, is presented, a brief introduction on how it works is reported in the following.

At first, BAW devices must possess a basic configuration composed by a microfluidic channel with two parallel and opposing walls to perform acoustophoresis. Indeed, these elements not only are fluidic boundaries for the flow, but also behave as reflectors (acoustic boundary) for waves propagating in the fluid. Thus, when bulk waves reflected at the fluid/structure interface, a superposition of an incident and a reflected propagating wave in the microfluidic channel results in an ultrasonic standing wave field[144][145][146]. Therefore, when this wave field is established in the microfluidic channel, suspended particles moves to its pressure nodes or anti-nodes due to the primary acoustic radiation force and mechanical characteristics (i.e. size, density, compressibility) of particles and surrounding fluid. This force acting on compressible spherical objects in a standing wave field, referring from literature[147][148][149][150][151], can be defined as:

$$\mathbf{(4)} \quad \boldsymbol{F_R = -\left(\frac{\pi p_0^2 V_p \beta_p}{2\lambda}\right) \phi(\beta,\rho) sin\left(\frac{4\pi x}{\lambda}\right)}$$

$$\mathbf{(5)} \quad \boldsymbol{\phi(\beta,\rho) = \frac{5\rho_p - \rho_m}{2\rho_p + \rho_m} - \frac{\beta_p}{\beta_m}}$$

where p_0 is the acoustic pressure derived from the standing waves, V_p, β_p and ρ_p are the volume, the compressibility and the density of particles, meanwhile β_m and ρ_m are the compressibility and density associated to the surrounded fluid and finally, ϕ, λ and x are the acoustic contrast factor, wavelength of the acoustic wave and distance from a pressure node, respectively. Thus, acoustic primary force acts on particles possessing a diameter lower than the acoustic wavelength and moving them toward the node or the anti-node of the standing wave field depending if the acoustic contrast factor value is positive or negative, respectively.

In microfluidic systems, dominated by low Reynolds number, one has also to take into account another type of force acting on a particles suspended in an aqueous solution. This force, given by the viscous attenuation of the suspended medium, corresponds to the Stokes drag force and it is defined as[152]:

$$\mathbf{(6)} \quad \boldsymbol{F_D = -6\pi\eta_m a_0 v_p}$$

where η_m corresponds to the fluid viscosity while a_0 and v_p refer to size and speed of particle, respectively.

Thus, since the primary radiation force is proportional to the volume of particles meanwhile the drag force is proportional to its radius, as particles size decreases Stokes force prevails over the acoustic one becoming the predominant phenomenon acting on particles in the systems. Therefore, equalizing the primary acoustic radiation force and the Stokes one, it is possible to determine the critical particle size diameter ($2a_0$) below which particles cannot be collected at the pressure node of the standing wave field[152][153][154][155]:

$$\mathbf{(7)} \quad \boldsymbol{2a_0 = \sqrt{\frac{3\eta_m}{\phi\rho_m\pi f}}}$$

where f refers to the frequency associated to the acoustic wavelength.

Moreover, solving the differential equation derived from balancing the previous forces and by separating y and t components, one can also derive the analytical expression for the transverse particle path[156][157][158]:

$$\mathbf{(8)} \quad \boldsymbol{y(t) = \frac{1}{k} arctan\left\{tan[ky(0)] exp\left[\frac{4\phi}{9\eta_m}(kr)^2 E_{ac} t\right]\right\}}$$

where $y(0)$ is the transverse position at time $t = 0$, $k = \frac{2\pi}{\lambda}$ is the wave number along the y-component and E_{ac} corresponds to the acoustic energy density of the system. Finally inverting the above expression one can determine the acoustic energy density needed to move particles from any initial position $y(0)$ to the pressure node of the system $y(t)$:

$$\mathbf{(9)} \quad \boldsymbol{E_{ac} = \frac{9\eta_m}{4\phi(kr)^2 t} ln\left[\frac{tan[ky(t)]}{tan[ky(0)]}\right]}$$

Then, knowing the acoustic energy one can also determine the pressure amplitude into the microfluidic channel by inserting this value in equation **(4)**:

$$\mathbf{(10)} \quad \boldsymbol{p_a = 2\sqrt{E_{ac}\rho_m c_m^2}}$$

where c_m refers to the surrounded medium sound velocity where particles are suspended.

3.2 Materials and methods

3.2.1 Design

The design of the BAW device presented in this chapter corresponds to a transversal resonator. In this configuration the piezoelectric element, which transforms a sinusoidal voltage to a mechanical vibration at a defined frequency[159], was arranged underneath the microfluidic channel of the device.

Therefore, in a transversal resonator the microfluidic device is excited by a characteristic frequency that leads to the formation of an ultrasonic standing wave across the microchannel width perpendicular to the direction of actuation. This frequency matches the half wavelength criterion with respect to the channel width. In detail, in the developed BAW device first resonance modes, characterized by a pressure node along the centre of the microfluidic channel and pressure anti-nodes along its side walls, were exploited (**Figure 3.2.1**). In this way, particles and cells characterized by a positive acoustic contrast factor[160], the ones illustrated in this chapter to evaluate the BAW chip performance, were collected at centre of the microfluidic channel.

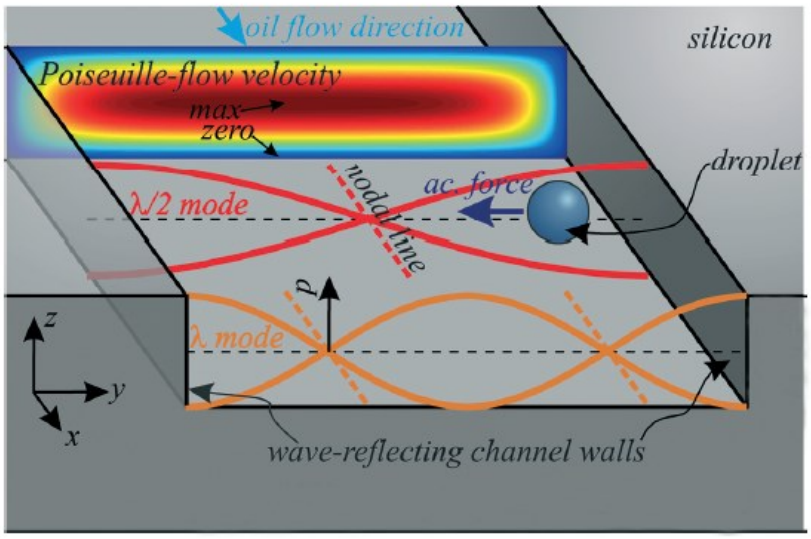

Figure 3.2.1 Sketch of resonance modes in BAW resonator configuration. Image from[144].

Then, according to literature[116][145][161][129], the width of the microfluidic channel w_{ch} was designed as:

(11) $$w_{ch} = \frac{\lambda_{med}}{2}$$

where λ_{med} corresponded to the wavelength of the acoustic wave in a characteristic suspending medium. It derived from the ratio between the sound speed of the suspending medium c_{med} and the resonant frequency f of the device.

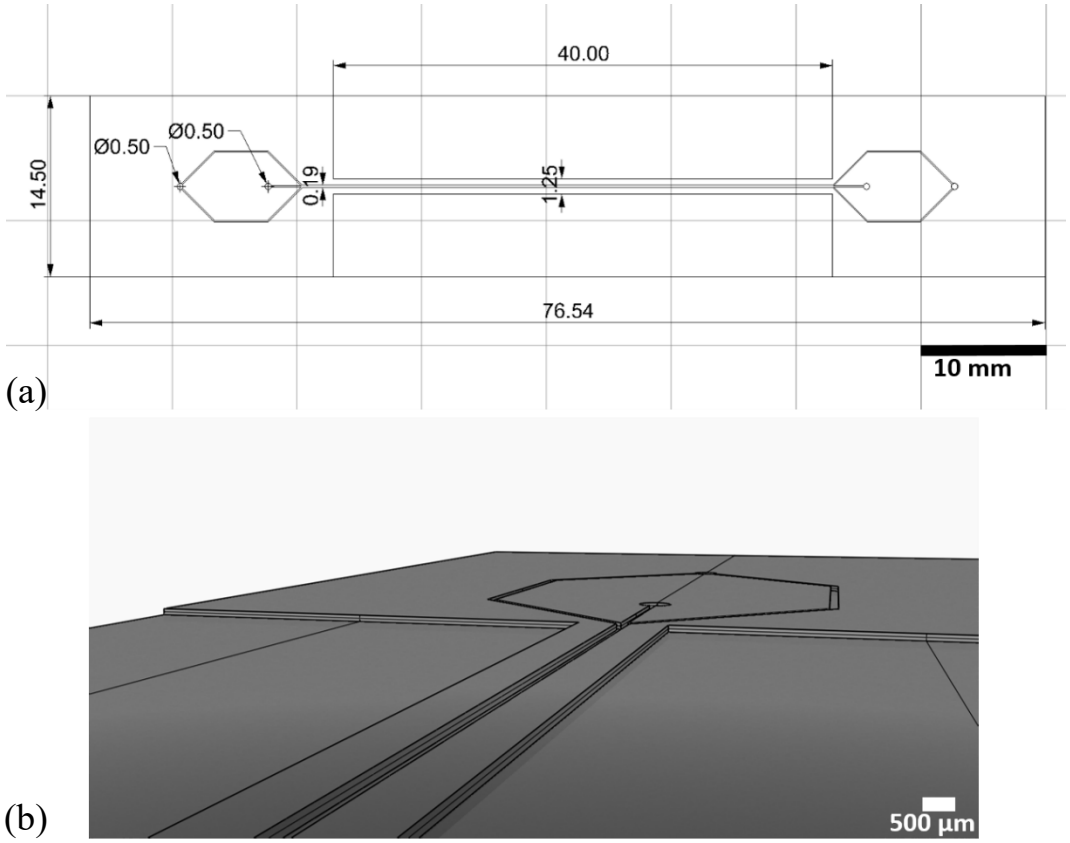

Figure 3.2.2 CAD of the BAW device: (a) 2D draw with nominal CAD dimensions and (b) 3D channel cross section design.

Thus, evaluating water as suspended medium[153] and a piezoelectric element frequency working in the 4 MHz-range it was possible to define device dimensions. In detail, BAW chip was defined by the following dimensions: 14.50 mm in width, 76.54 mm in length and with a height of 1.05 mm. It consists of two symmetric inlets and outlets, with 500 µm of hole diameter, and a straight channel 40 mm long with a rectangular cross section 190 µm wide and 95 µm deep (**Figure 3.2.2**). In correspondence to the straight channel, device walls width presented narrower dimensions to allow for the formation of the standing wave field across the microfluidic channel[156]. This value, equal to an even number of the acoustic wavelength, was imposed to be 530 µm.

Finally, exploiting the equation **(7)** it was possible to define the analytical value relative to the minimum particles diameter that could be collected at the node of the microfluidic channel. This value was 1.6 µm.

3.2.2 Device fabrication

As mentioned before, since this type of BAW resonator relied on reflections between channel walls, to manufacture them high characteristic acoustic impedance materials must be considered[161]. Due to this, the bottom substrate of the BAW device was manufactured in silicon by using a standard silicon microfabrication technique, since a precise channel structure with vertical walls was required.

A 4-inch n-type silicon wafer with (100) orientation and 0.35 mm thick finished with 1 μm of thermal SiO_2 was used. Firstly, the adhesion promoter photoresist (Ti Prime, Microchemicals GmbH) was coated on the silicon wafer by using a spin coater (Spinner 150 Wafer Spinner) by setting 5 seconds at 500 rpm and 30 seconds at 4000 rpm to guarantee a perfect adhesion between the silicon surface and the photoresist used as mask. Then, a soft bake step occurred on a hot plate at 120°C for 2 minutes. Next, the wafer was spin coated by a positive photoresist AZ1518 (Microchemicals GmbH) by setting 5 seconds at 500 rpm and 30 seconds at 4000 rpm to define a mask characterized by an average thickness of 1.41 μm. The photoresist was exposed for 10 seconds to standard UV photolithography by means of double side mask aligner (Neutronix Quintel NXQ 4006) used in contact mode, ensuring the correct alignment between the photoresist and the desired mask patterns. Next, the photoresist was developed using a solution of 1:4 AZ400K developer (Microchemicals GmbH) in deionized water for 40 seconds, then rinsed twice with deionized water and dried with a nitrogen flux. After that, a Buffer Oxide Etching (BOE) was performed for 15 minutes to remove the thermal oxide in the unwanted area and the microchannel etching was completed by Deep Reactive Ion Etching (DRIE) (Oxford Plasmalab 100 System). A Bosch® process was performed to obtain an about 90 μm deep microchannel and hollows along it with highly vertical sidewalls, using the following parameters: 1500 W of ICP power, 10 W of RF power, 50 sccm of C_4F_8 for the passivation step extent of 4 s, and 150 sccm of SF_6 for the etch step extent of 7 s, imposing 14 sccm of He backside cooling to maintain 18°C on the wafer in both steps. After that, the etched silicon wafer was submerged into a solution of sulphuric acid and hydrogen peroxide in a 3:1 ratio (v/v) for 5 minutes to remove the residual AZ1518 mask layer, rinsed 3 times in water and dried with a nitrogen flux. A further BOE process was performed to remove the residual thermal oxide after the DRIE step. Devices and inlets/outlets dicing and drilling were achieved by laser etching (50 W G4 Pulsed Fiber Laser, Infra 1064 nm) and finally the device was sealed with a 500 μm thick slice of borosilicate glass (Corning 7740) by anodic bonding (**Figure 3.2.3**).

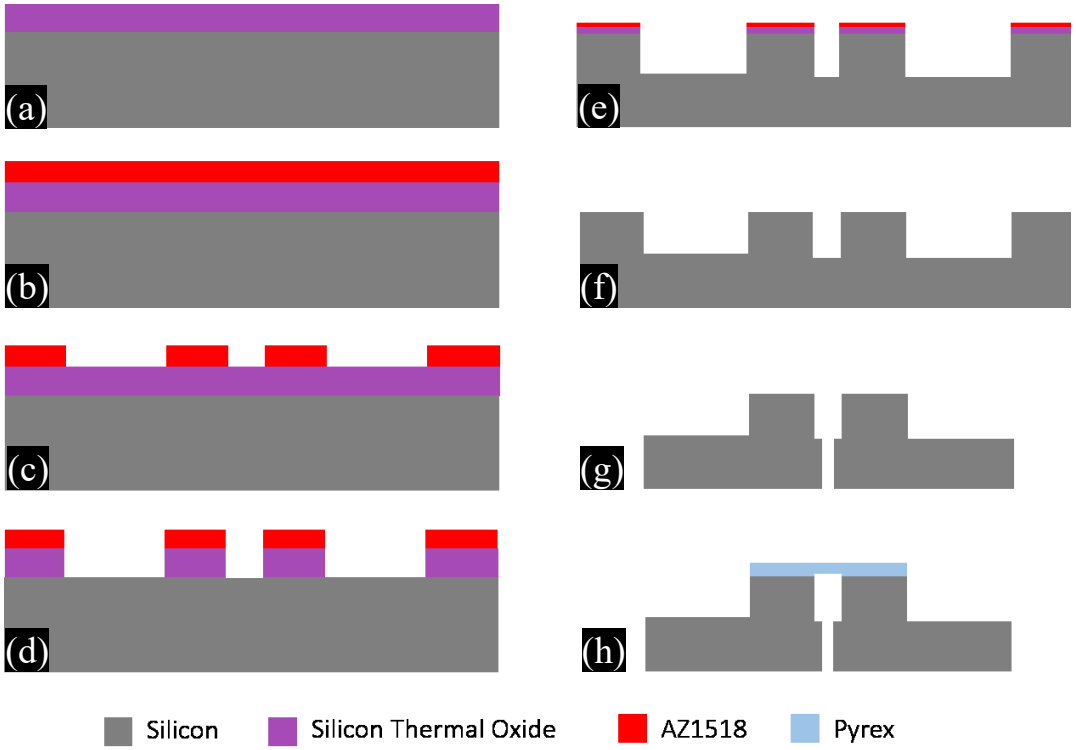

Figure 3.2.3 BAW device process flow: (a) starting substrate cleaning, (b) photoresist spin coating, (c) photoresist exposure and development, (d) buffer oxide etching, (e) silicon deep reactive ion etching, (f) buffer oxide etching, (g) inlets/outlets laser drilling and chip dicing and (h) anodic bonding.

3.2.3 Device assembly

PDMS interconnections were sealed on the bottom of the microfluidic device in correspondence to inlets and outlet ports to ensure a stable connection with PoliUrethane (PU) tubes (SMC OD = 2.0 mm, ID = 1.2 mm) and the device. The ultrasonic standing waves were generated by a piezoelectric plate (CuNi 20x20x0.5 mm^3 with screen printed Ag electrodes from PI) with a nominal resonance frequency of 4 MHz. This element was located on the back side of the microfluidic channel, to ensure a continuous flow of separated particles. Such arrangement between the microfluidic device and the piezoelectric plate allowed a large contact surface area, empowering a good coupling of the acoustic energy into the BAW device[116]. Furthermore, to improve acoustic coupling between the transducer and the rear side of the microfluidic channel, a thin layer of ultrasound gel (Shockwave Gel from ELvation Medical GmbH) was employed. Indeed, an ultrasound gel, not only minimizes the acoustic losses but also allows using the same transducer several times and to move it along the microfluidic channel[129].

3.2.4 Device characterization methods

Field emission scanning electron microscopy (Zeiss Supra 40 FE-SEM) and optical microscope (Leica DVM 2500) images were acquired to analyse the cross

section of the microfluidic channel and to inspect the device dimensions during fabrication steps. Finally, an out-of-plane vibrational characterization of the transducer was performed by a scanning laser-Doppler vibrometry (Polytec MSA-500). This result served to find the exact resonance frequency of the BAW device. Indeed, by imposing the previous found frequency values one by one to the waveform generator and monitoring particles inside the microfluidic channel through the microscope, when the flow rate was ineffective, it was possible to define the exact resonance frequency of the microfluidic channel. In detail, this one was determined when particles stable in water dispersion moved to the node of the standing wave acoustic field aside from the voltage value applied at the piezoelectric element.

3.2.5 Experimental Setup

A customized experimental setup, composed by different elements, was assembled and it is illustrated in **Figure 3.2.4**. Tests presented in this chapter were performed exploiting only one inlet access. In details, through the PDMS interconnection the device inlet was joined to the PU tube to a plastic syringe (Terumo syringe, 2.5 mL), where a syringe pumping system (Harvard Apparatus 11 Plus) was used to inject the analyte solution. The piezoelectric element was actuated by applying a harmonically oscillating peak-to-peak voltage (V_{pp}) generated by a waveform generator (Agilent 33220A). In particular, the voltage was amplified by 50 dB by a radio frequency (RF) power amplifier (EI Ldt. 2100L 10 KHz-12MHz, 100W) connected to a dummy load terminator (50 Ω, 100 W). During the experiments the microfluidic channel was monitored and time-lapses were acquired through a sCMOS camera (Hamamatsu) of a fluorescence microscope (Nikon Eclipse Ti-E Inverted) with a 4x objective lens.

Before each experiment, the device was firstly washed with a 70% ethanol solution (v/v) at a flow rate of 30 µL/min for 10 min and then rinsed twice with bi-distilled Water (MilliQ, from now water) employing the same settings of flow rate and time. Between etch run the device was rinsed with water at a flow rate of 30 µL/min for 10 minutes. Regarding proof-of-concept experiments, since cells were dispersed into a Phosphate buffered saline (PBS) solution at 7.4 pH (Sigma-Aldrich), last washing steps either before the experiment and between each run were performed with PBS.

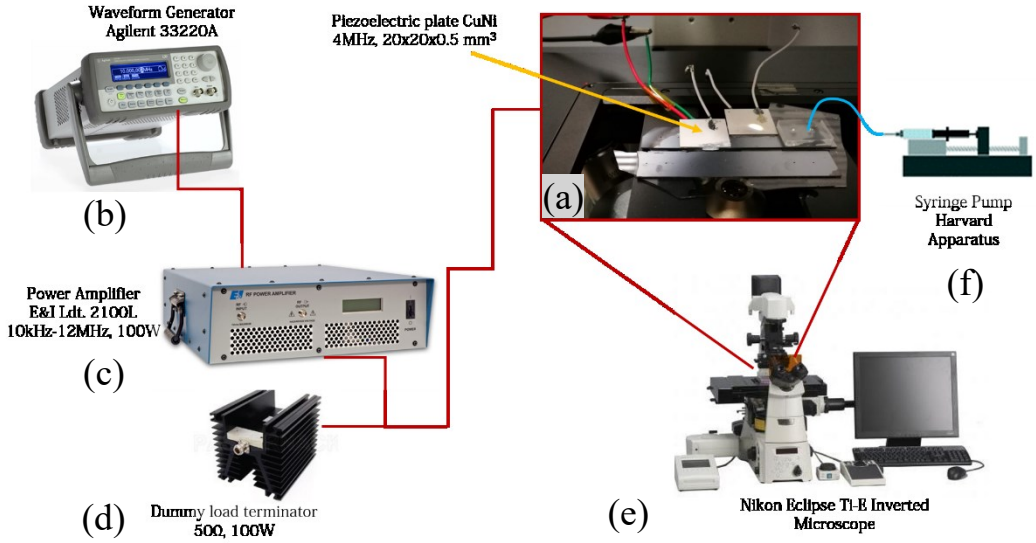

Figure 3.2.4 Experimental setup: (a) BAW device and transducer elements in which: the light blue line indicates the MPs solution and the red one the electrical connections to actuate the piezoelectric element; (b) waveform generator, (c) RF power amplifier, (d) dummy load, (e) fluorescence microscope, (f) syringe pump.

3.2.6 Micro and Nanoparticle samples

To evaluate the performance of the BAW device, different analytes, characterized either by a single type and a mixed population of particles, were employed. Due to this, 4 µm fluorescent sulfated polystyrene micro particles (from now on called 4MPs) (from FluoSpheres™) diluted in water with 0.01% Tween20 (Sigma-Aldrich) were used with concentrations equal to 5.68×10^6 particles/mL, 1.14×10^6 particles/mL and 5.68×10^5 particles/mL. 1 µm fluorescent sulfated polystyrene micro particles (from now on called 1MPs) (from FluoSpheres™) diluted in water with 0.01% Tween20 were employed with a concentration of 1.00×10^6 particles/mL. Finally, the mixed population of micro and nanoparticles was characterized by 4MPs and 500 nm fluorescent carboxylated polystyrene nanoparticles (from now on called NPs) (from Magsphere Inc.) diluted in water with 0.01% Tween20. In details, 4MPs batch concentration was equal to 5.68×10^5 particles/mL, while NPs one corresponded to 3.64×10^5 particles/mL.

3.2.7 Biological samples

Cells employed for proof-of-concept experiments were HL-60 cells (ATCC® CCL-240™) obtained from an acute promyelocytic leukemia patient. Cells were grown in suspension and they were maintained in Iscove's Modified Dulbecco's Medium (Sigma-Aldrich) supplemented with 20% heat inactivated FBS (Sigma-Aldrich), 1% L-Glutammine (Sigma-Aldrich), 100 units/mL Penicillin and 100 µg/mL Streptomycin (Sigma-Aldrich) in 25-75 cm^2 non treated cell culture flasks (Corning) in cell incubator at 37 °C in a humified atmosphere containing 5% CO_2.

To perform experiments, the following protocol was employed to label cells. Firstly, cells were counted and a certain number of cells were pelleted by centrifugation at 130 g for 5 minutes and resuspended in 500 µL of PBS to reach one of the desired densities between 5.00×10^6 cells/mL, 1.00×10^6 cells/mL and 5.00×10^5 cells/mL. Then, plasma membranes of cells were labelled with WGA (Wheat Germ Agglutinin) conjugated with Alexa Fluor 647 dye (Thermo Fisher). In detail, 2.5 µL of WGA (1 mg/mL, w/v) were added to cells in PBS solution to reach a concentration of 5 µg/mL, as recommended by the manufacturer and they were placed in an orbital shaker at 37°C setting 50 rpm for 10 minutes in dark. Later, as washing step to remove the unlabelled dye, cells were centrifuged at 130 g for 5 minutes and resuspended in 500 µL of PBS (**Figure 3.2.5**).

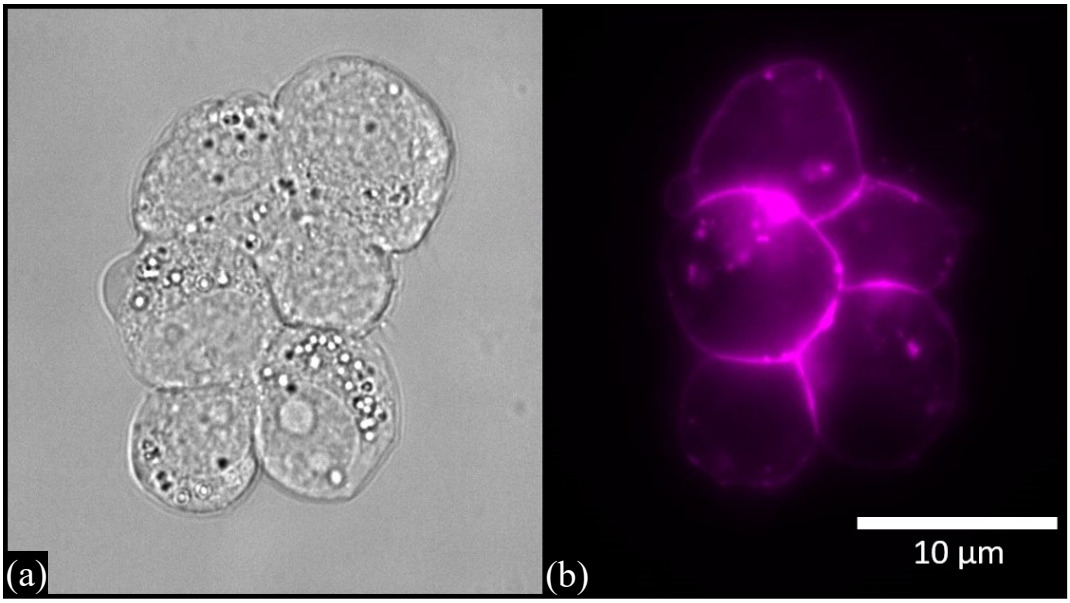

Figure 3.2.5 HL60 cells at fluorescence microscope image: (a) bright field acquisition and (b) NIR filter acquisition.

3.2.8 Focusing characterization methods

Various conditions were taken into account to evaluate the performance of the BAW device to focalize either particles and cells at the node of the acoustic standing wave when the device was stimulated at its resonance frequency. In detail, the focusing capability of the BAW device was performed with a constant resonant frequency and by varying for each test one of the following parameters: samples concentration or type, flow rate and applied voltage at the piezoelectric element.
The performance of the BAW device was determined by analysing samples collected at the outlets by two different approaches. In the first one, the focusing was defined as the ratio between the absorbance of elements collected at the central outlet solution (node) and the total absorbance of elements derived from the absorbance of elements at the two outlets. In detail, absorbance values were quantified by a UV-Vis characterization as already explained for the µFFE device (see **2.2.5**). Due to this, calibration curves of cells and cells mixed with particles

were performed setting 650 nm as impinging wavelength for evaluate cells absorbance values. Whereas, concerning particles absorbance characterizations were used the previous calibration curves (see **2.2.5**).

The other way to evaluate the ability to collect particles at the node was performed by analysing images acquired during a time-lapse by exploiting the Co-localization program (Nis-Element from Nikon) of the fluorescence microscope. By this, samples analysis was available when thresholds between background fluorescence intensities and samples sizes were defined. Thus, with this approach the focusing was defined as the ratio between the counted elements localized at the centre of the microfluidic channel (node) and the counted elements in the microfluidic channel. Time-lapses were implemented for 50 seconds: images were acquired every 300 milliseconds with an exposure time of 9.8 milliseconds in the green channel (FITC-A filter) regarding 4MPs. HL-60 cells time-lapses were implemented for 30 seconds; thus images were acquired every 50 milliseconds with the same exposure time in the near infrared (NIR) channel (Cy5-4040C filter). Finally, for the mixed population of 1MPs and HL-60 cells time lapses were acquired every 30 milliseconds setting an exposure time of 9.8 milliseconds in the green channel for the 1MPs and an exposure time of 20 milliseconds in the NIR channel for the HL-60 cells. Regarding NPs, it was not possible to acquire time-lapse characterizations since the resolution limit of the 4x objective lens (1.63 μm/pixel).

During tests performed with HL-60 cells, a third approach was applied to evaluate the performance of the BAW device. This was done by manually counting cells collected at the outlets through a counting chamber Bürker. Briefly, 10 μL of the cell suspension were placed in the Bürker chamber, cells were manually counted as cell density, intended as number of cells/mL, and thus the total number of cells collected in the two outputs and the percentage of focalization were assessed[162].

To end, experiments with the same conditions were repeated at least three times, thus error bars were reported according to the acquired data over the repetitions.

3.2.9 Experimental determination of the acoustic energy

The experimental value of the acoustic energy density was defined by analysing the transient acoustophoretic focusing of particles[152][156]. Thus, time-lapses of 4MPs concentrated at 5.68×10^7 particles/mL were implemented for 2 minutes meanwhile the ultrasounds were turned off (V_{pp} = 0 V) and on (V_{pp} = 52.92 V). Images were acquired every 500 milliseconds with an exposure time of 9.8 ms in the green channel. Then, these videos were elaborated by an open source video analysis software called *Tracker 2.6* (from open source physics by PD. Brown), which allowed to extract the analytical expression of transverse path *y(t)* of each particle captured in the video frame to frame. Then, mediating the list of (t, y)-coordinates of 20 particles paths for the defined time needed to move particles at

the nodes and solving the equation **(8)** it was possible to estimate the acoustic energy density value.

Finally, knowing the acoustic energy density value, by applying the equation **(10)** it was also possible to determine the pressure amplitude in the BAW device.

3.3 Results and discussion

3.3.1 Device morphological analysis

Morphological analyses on BAW device were performed to evaluate features dimensions. As first step, during the fabrication process, optical images of AZ1518 photoresist were acquired after developing the mask to check a correspondence between the mask pattern and the design one (**Figure 3.3.1**).

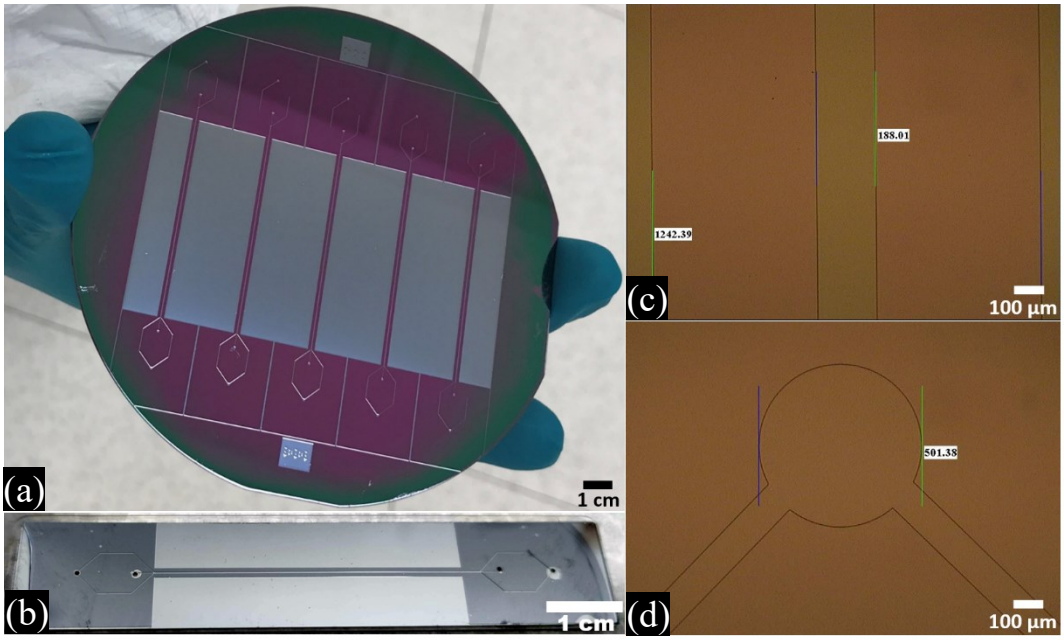

Figure 3.3.1 Optical photographs capture during the BAW fabrication process: (a) BAW devices on silicon wafer after DRIE, (b) final BAW device (c) inset of microchannel and wall width measurements performed through an optical microscope with a 10x objective lens and (d) inset of access port measurement performed through an optical microscope with a 10x objective lens.

A comparison between the real microchannel and walls dimensions and the design ones was performed analyzing cross-section FE-SEM images of BAW device (**Figure 3.3.2**). In details, the microfluidic channel of the BAW device possessed a width average value of 198.73 ± 3.60 µm and a height mean value equal to 87.13±2.16 µm. Meanwhile, walls width average value was 517.81±14.63 µm.

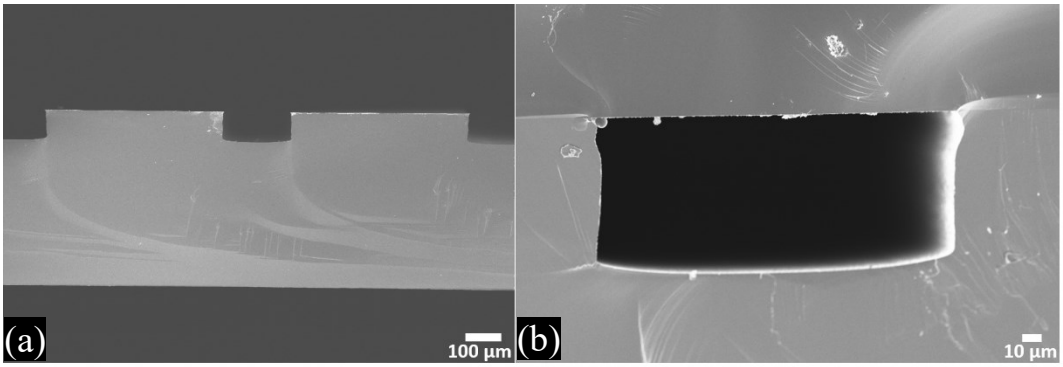

Figure 3.3.2 Cross section FESEM images of BAW device: (a) silicon part of the device, magnification 200x and (b) cross section of the assembled device, magnification 1000x.

Thus, the microfluidic channel of the BAW device was characterized by a rectangular cross section having a larger width dimension and a smaller height value respect to the CAD ones as depicted in **Table 3.3.1**.

BAW device		
Features	**CAD (µm)**	**Device mean value (µm)**
Channel width	190.00	198.73
Channel height	95.00	87.13
Wall width	530.00	517.81

Table 3.3.1 CAD dimensions versus real values.

Figure 3.3.3 illustrates the out-of-plane vibrational characterization of the transducer performed by a scanning laser-Doppler vibrometry. Considering the range of frequencies where was detected the maximum displacement of the transducer, it was possible to define the resonance frequency of the BAW device. Indeed, imposing these frequencies values one by one to the waveform generator and monitoring particles inside the microfluidic channel through the fluorescence microscope, when the flow rate was ineffective, it was possible to find the exact resonant frequency of the microfluidic channel. This one was 4.623 MHz. At this frequency value, particles stable in the surrounded water solution moved to the node of the standing wave acoustic field, thus at the centre of the microfluidic channel, aside from the voltage value applied at the piezoelectric element.

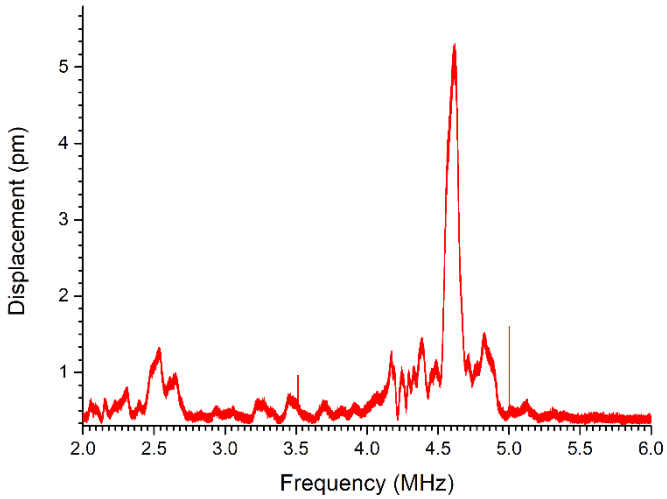

Figure 3.3.3 Measurement of the displacement of the piezoelectric element performed throughout the laser-Doppler vibrometry instrument.

3.3.2 Focusing test with micro particles

At the beginning, focalization tests were performed employing a single type of particles to investigate one by one the optimal setting values to impose to reach the maximum achievable collection of particles at the pressure node of the BAW device. Thus, referring from literature[116][156], a first set of experiments was performed with 4MPs concentrated at 5.68×10^6 particles/mL dispersed in water and injected at different flow rates. Tests were carried out applying 50.59 V_{pp} to the transducer by actuating the microfluidic channel at its resonance frequency. As showed in **Figure 3.3.4(a)** focusing values, characterized throughout a UV-Vis analysis, at low flow rates lead to an increased collection of particles at the pressure node of the standing acoustic wave field. Indeed, at 1 µL/min it was 91%, while for 3 µL/min and 10 µL/min it corresponded to 72% and 65%, respectively. A further proof of this focusing trend at different flow rates, was also detected by the image analysis, where for each experiment, thus each time-lapse, values were mediated evaluating 20 equidistant images of a time lapse (**Figure 3.3.4(b)**). In this case the focusing percentage values were 96% at a flow rate of 1 µL/min, 78% for a flow rate equal to 3 µL/min and 51% when 4MPs moved at 10 µL/min. This is because low flow rates leaded suspended particles to be subjected to the ultrasound field for a longer time period while travelling through the microfluidic channel, allowing more particles to reach the pressure node[119].

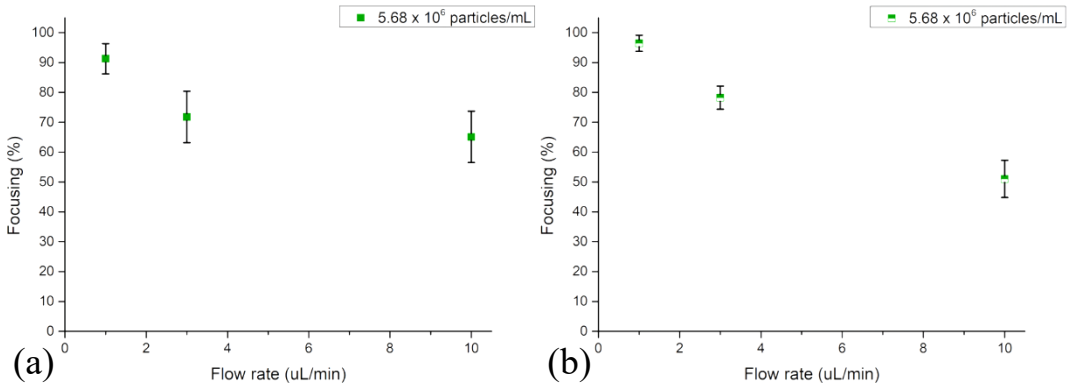

Figure 3.3.4 Focusing performance of the BAW device with 4MPs concentrated at 5.68×10^6 particles/mL injected at 1 µL/min, 3 µL/min and 10 µL/min: (a) UV-Vis characterization and (b) image analysis. Experiments were performed applying 50.59 V_{pp} at the transducer meanwhile the device was actuated at its resonance frequency of 4.623 MHz.

A similar trend of particles collected at the node of the BAW device, when different flow rates were examined, was noticed by exploiting two other 4MPs concentrations. Leaving other settings constant, tests accomplished with different particles concentrations, showed that lower concentrations promoted a higher collection of particles at the node of the microfluidic channel (**Figure 3.3.5**).

An increased collection of 4MPs at the node of the microfluidic channel was detected at 3 µL/min and 1 µL/min. Indeed, the 100% and the 96% of focusing percentage values were characterized via the UV-Vis method when 4MPs concentrated at 1.14×10^6 particles/mL and 5.68×10^5 particles/mL were injected at 1 µL/min. At 3 µL/min these values, performed throughout the UV-analysis were 80% and 93%, for 4MPs concentrated at 1.14×10^6 particles/mL and 5.68×10^5 particles/mL, respectively. These results were confirmed by the image analysis, with a maximum discrepancy of 6% detected between the two characterization methods average values.

Focusing percentage values of the BAW device at 10 µL/min were 68% and 75% for a concentration equal to 1.14×10^6 particles/mL and 5.68×10^5 particles/mL through the UV-Vis analysis. A comparable range of focusing values, equal to 70% and 71% were obtained via image analysis characterization when the following concentrations 1.14×10^6 particles/mL and 5.68×10^5 particles/mL were injected in the device, respectively.

Then a negative effect on the device's focusing performance was correlated to higher concentrations, when particles collected at the pressure node saturated it causing an increase of inter-particle forces and thus requiring a stronger acoustic force[163][146][164].

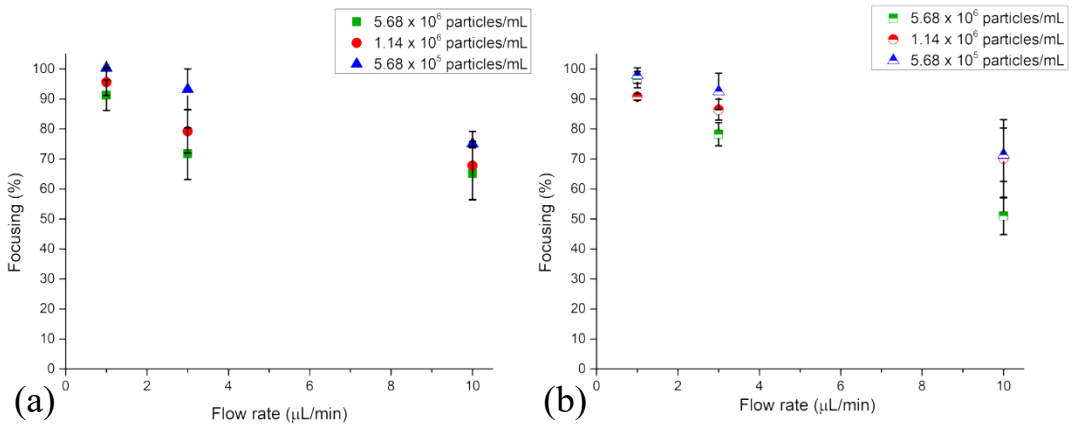

Figure 3.3.5 Focusing performance of the BAW device as a function of flow rates and 4MPs concentrations: (a) UV-Vis characterization and (b) image analysis. Experiments were performed with 4MPs concentrated at 5.68×10^6 particles/mL, 1.14×10^6 particles/mL and 5.68×10^5 particles/mL. During the experiments 4MPs were injected at 1 µL/min, 3 µL/min and 10 µL/min, while 50.59 V_{pp} was applied at the transducer when the device was actuated at its resonance frequency of 4.623 MHz.

A second set of tests observed how changed the focusing performance of the BAW device when the following voltages were applied to the piezoelectric element: 56.92 V_{pp}, 50.59 V_{pp}, 37.95 V_{pp}, 25.29 V_{pp} and 12.65 V_{pp}. During these experiments 4MPs, concentrated at 5.68×10^5 particles/mL, were injected at 3 µL/min when the microchannel was actuated at its fundamental resonance frequency.

As reported in **Figure 3.3.6** either by UV-Vis characterization and image analysis, higher voltages were associated to higher focusing values. In details, when 12.65 V_{pp} were applied to the piezoelectric element, the focalization was 57% for the UV-Vis analysis and 64% via the image one, while when 56.92 V_{pp} were set to the transducer the 97% of particles converged to the pressure node of the microfluidic channel, as determined by both characterization techniques. At intermediate voltage values applied to the transducer, that is to say 25.29 V_{pp} and 37.95 V_{pp}, focusing values were 67% and 75% for the UV-Vis characterization, while through image analysis they were 68% and 85%, respectively.

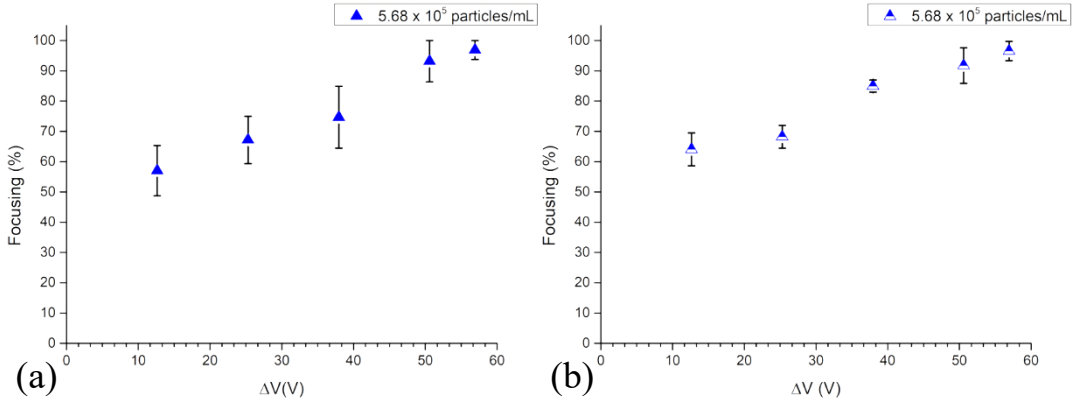

Figure 3.3.6 Focusing performance of the BAW device as a function of applied voltages at the transducer: (a) UV-Vis characterization and (b) image analysis. During the experiments 4MPs concentrated at 5.68×10^5 particles/mL were injected at 3 µL/min into the device actuated at its resonance frequency of 4.623 MHz, while 56.92 Vpp, 50.59 Vpp, 37.95 Vpp, 25.29 Vpp and 12.65 Vpp were applied at the transducer.

Finally evaluating the focusing values illustrated in (**Figure 3.3.5** and **Figure 3.3.6**), it is possible to affirm that both UV-Vis characterization and images analysis were useful approaches able to describe the focalization performance of the BAW device with a maximum value discrepancy of 10%.

In addition, observing the time-lapse images it is possible to notice that as long as particles concentration decreased, the acoustic force increased inducing particles to accumulate in a narrower band along the pressure node (**Figure 3.3.7**). An analogous effect was observed also when the voltage applied to the piezoelectric element increased, indeed, narrower band along the pressure node was detected at higher voltages.

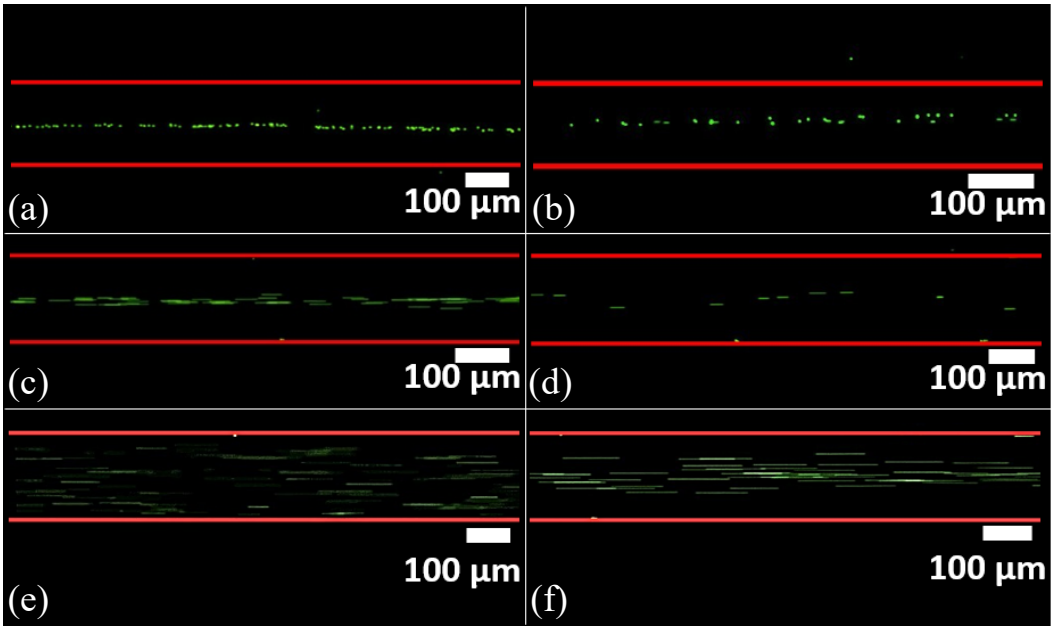

Figure 3.3.7 Frame of time-lapse acquired during the acoustophoretic test, when 4MPs were employed at different concentrations and flow rates: (a) 4MPs concentrated at 5.68×10^6 particles/mL were injected at 1 µL/min, (b) 4MPs concentrated at 1.41×10^6 particles/mL were injected at 1 µL/min, (c) 4MPs concentrated at 5.68×10^6 particles/mL were injected at 3 µL/min, (d) 4MPs concentrated at 1.41×10^6 particles/mL were injected at 3 µL/min, (e) 4MPs concentrated at 5.68×10^6 particles/mL were injected at 10 µL/min and (f) 4MPs concentrated at 1.41×10^6 particles/mL were injected at 10 µL/min. Experiments were performed applying 50.59 V_{pp} at the transducer, while the device was actuated at its resonant frequency of 4.623 MHz. Images acquired with 4x objective lens with an exposure time of 9.8 ms.

Further focalization tests were carried out to check experimentally the critical particles diameter $2a_0$ derived from the equation **(7)**. Indeed, particles owing a size below $2a_0$ value cannot be collected at the pressure node of the microfluidic channel because primary acoustic force becomes weaker compared to Stokes drag force, as already discussed. Thus, for these experiments a solution of 1MPs was selected, since from analytical evaluation the critical particles diameter was 1.6 µm. Then, 1MPs concentrated at 1.00×10^6 particles/mL were injected at 1 µL/min into the BAW device actuated at its resonance frequency when different voltages were applied to the piezoelectric element. In details, voltages values were chosen accordingly to the maximum collection of particles at the node of the BAW device

from previous experiments, thus 50.59 Vpp and 56.92 Vpp. Both cases showed up a low focalization value in accordance with the analytical result, indeed it corresponded to 46% and 47% when 50.59 Vpp and 56.92 Vpp were applied to the transducer, respectively (**Figure 3.3.8**). Therefore, last results stated that this design cannot be employed to focalize particles characterized by sizes equal or below 1.6 µm at the pressure node of the device.

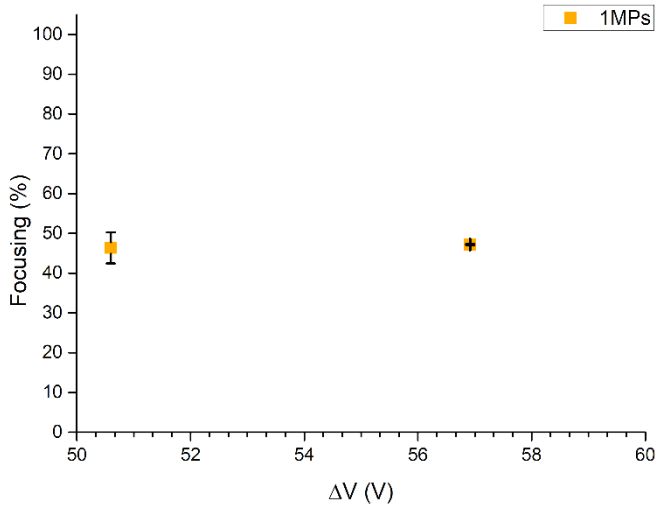

Figure 3.3.8 UV-Vis characterization of focusing performance of the BAW device with 1MPs concentrated at 1.00×10^6 particles/mL injected at 1 µL/min when the device was actuated at its resonance frequency of 4.623 MHz. Experiments were performed applying 50.59 V_{pp} and 56.92 V_{pp} at the transducer.

3.3.3 Focusing test with micro and nanoparticles

A further proof regarding the experimental evaluation of the critical particles diameter $2a_0$ was defined analyzing the BAW device performance when a mixed population of 4MPs and NPs concentrated at 2.84×10^5 particles/mL and 1.82×10^5 particles/mL, respectively, was used. In detail, the mixed population of particles was fluxed at a flow rate of 1 µL/min into the chip, while it was actuated at its resonance frequency when 50.59 Vpp or 56.92 Vpp voltages were applied to the piezoelectric element. As illustrated in **Figure 3.3.9**, focalization values related to 4MPs were 59% at 50.59 Vpp and 69% at 56.92 Vpp, while for the same applied voltages NPs focusing percentage values corresponded to 48% and 52%. Thus, even if NPs focusing performance appeared to be higher compared to the 1MPs one, this was due to the fact that NPs mixed with 4MPs interacted with them and so they are affected by the presence of micro particles and vice versa (i.e. surfaces electrostatic interactions, scatterings, second order radiation forces)[163]. Indeed, evaluating the focusing value only for the 4MPs population, concentrated at 5.68×10^5 particles/mL and injected at 1 µL/min when 50.59 Vpp was applied at the

transducer, it was 97%, a higher value related to 59% obtained when a mixed population was employed.

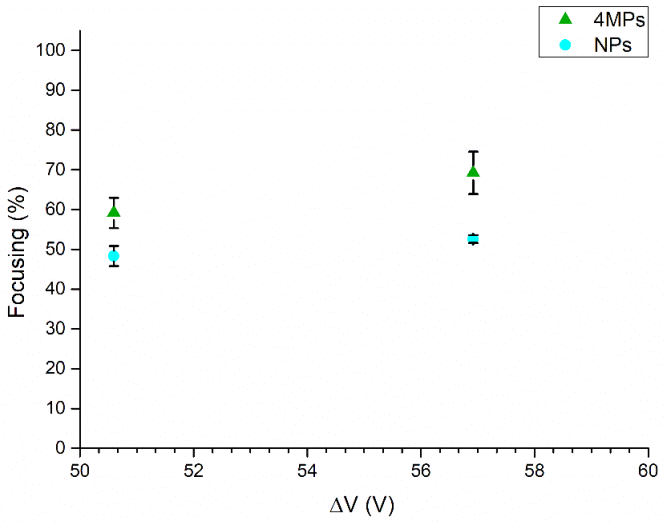

Figure 3.3.9 UV-Vis characterization of focusing performance of the BAW device when a mixed population of 4MPs concentrated at 2.84×10^5 particles/mL and NPs concentrated at 1.82×10^5 particles/mL were injected at 1 µL/min into the device, which was actuated at its resonance frequency of 4.623 MHz. Experiments were performed applying 50.59 V_{pp} and 56.92 V_{pp} at the transducer.

3.3.4 Measuring the acoustic energy

As mentioned before, from the analytical expression of the transverse path y(t) it was possible to estimate the acoustic energy density. **Figure 3.3.10** displays different transverse paths y(t) of particles inside the microfluidic channel of the BAW device acquired in a defined focal plane of the 4x objective lens. In detail, paths y(t) were highlighted by blank circles of different colors in a time lapse extracted from the *Tracker 2.6* video analysis tool. Thus, mediating the list of (t, y)-coordinates of particle paths for the defined time needed to move particles from channel walls to the node, and inserting these values to the equation **(8)** allowed to obtained an acoustic energy density value of $7.25 \pm 1.61\ \frac{J}{m^3}$.

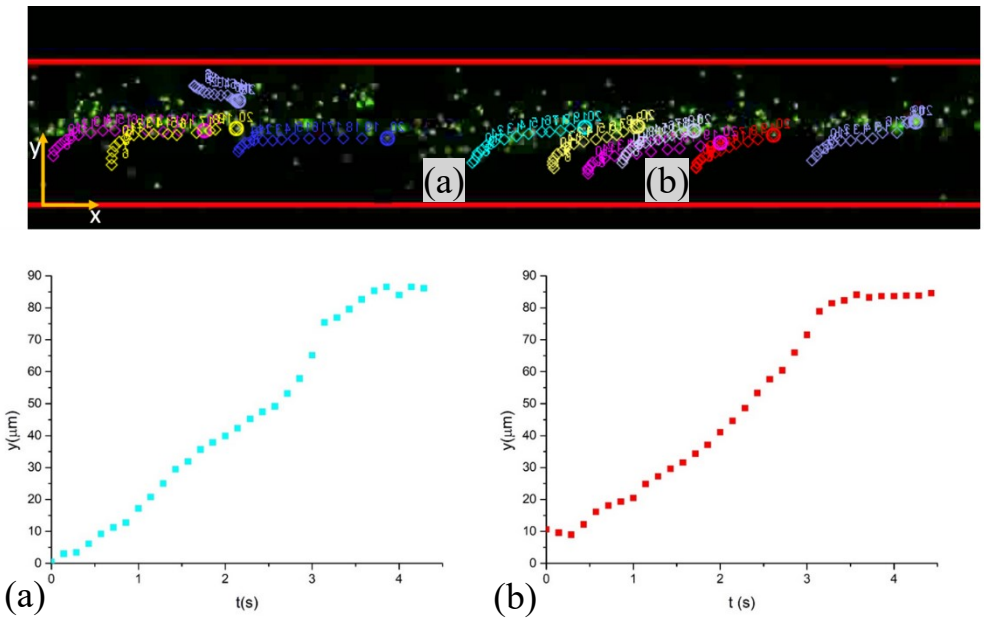

Figure 3.3.10 Tracking of beads paths with the Tracker 2.6 software and measurement of the transverse path y(t) from channel walls to the pressure node of two different beads (a) and (b). Measurements were performed in a specific focal plane of the 4x objective lens of the fluorescence microscope.

Finally, knowing the value of the acoustic energy density it was possible to define the pressure amplitude value inside the microfluidic channel of the BAW device equal to $p_a \approx 0.252\ MPa$.

3.3.5 Comparison between experimental and simulated particles focusing

Exploiting the acoustic energy density derived from the previous section, it was possible to use it to perform numerical tests as validation of certain experimental conditions. Thus, the acoustic energy density was set at 7 Pa and by computing the velocity and the pressure acoustic fields exploiting "Pressure Acoustics" and "The Particle Tracking for Fluid Flow velocities" interfaces of COMSOL Multiphysics® software it was possible to calculate the acoustic radiation force and the Stokes drag force experienced by particles. For each concentration, a fixed number of particles was injected from the inlet every second (29, 57 and 284, respectively) and the particles collected in the central outlet (defined by a region with a width equal to one third of the channel width) were recorded. **Figure 3.3.11** reports a comparison between results obtained experimentally and numerically. In details, a good match with promising percentages of focusing was shown. Increasing the concentration of particles leads to a lower efficiency in focusing either for experimental and numerical tests. This is an unexpected behaviour, since an increasing number of particles leads to a higher possibility of particle-particle forces and thus to aggregation. Considering these aggregates as particles with higher sizes, the acoustic radiation force has to be stronger and move the particles forward the pressure node very quickly. Despite of that, in these tests the acoustic energy

density had not high values, thus probably the particles could have not experienced a strong acoustic radiation force. Thus, they moved slowly to the pressure node and a fraction of the total number of the particles remained at the side of the channel. In spite of this effect, the focusing value was quite high for particles concentration of 5.68×10^5 particles/mL where simulation results were equal to 100% and experimental characterizations were 93%.

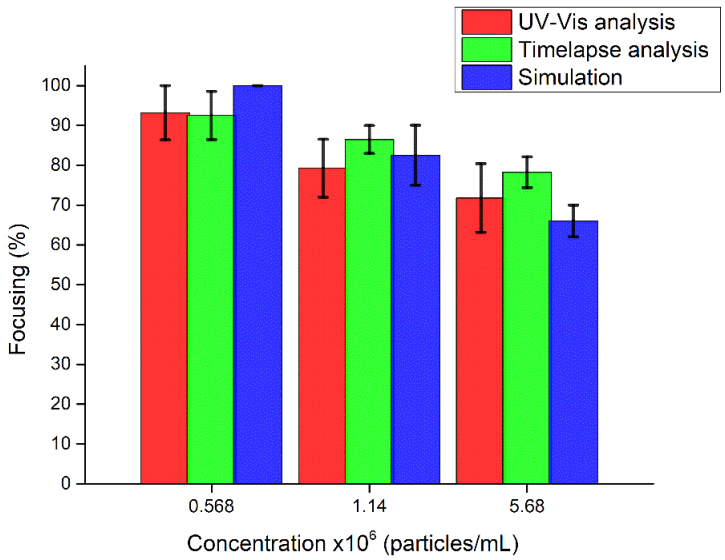

Figure 3.3.11 Comparison of the focusing performance of the BAW device obtained through simulations and experiments when 4MPs at different concentrations 5.68×10^6 particles/mL, 1.14×10^6 particles/mL and 5.68×10^5 particles/mL were investigated. Experimental values were reported characterized either by UV-Vis analysis and image ones.

3.3.6 Proof of concept

Proof of concept experiments were performed firstly with HL-60 cells as sample solution and then with a mixed population of cells and MPs or NPs.

At first, tests were performed with HL-60 cells dispersed in a PBS solution at the following concentrations: 5×10^5 cells/mL, 1×10^6 cells/mL and 5×10^6 cells/mL to evaluate the focusing performance of the device with biological samples. Tests were carried out applying 50.59 V_{pp} to the transducer, actuating the microfluidic channel at its resonant frequency and by injecting the solution of cells at a flow rate equal to 3 µL/min. As depicts in **Figure 3.3.12,** from counting chamber Bürker analysis, focusing performance was verified at all concentrations. Indeed, the 100% of focusing resulted either at 5×10^5 cells/mL and 1×10^6 cells/mL, while at 5×10^6 cells/mL, the highest value of cells concentration, it was 97%, suggesting that at this flow rate value cells were easily collected at the pressure node of the device even at higher concentrations.

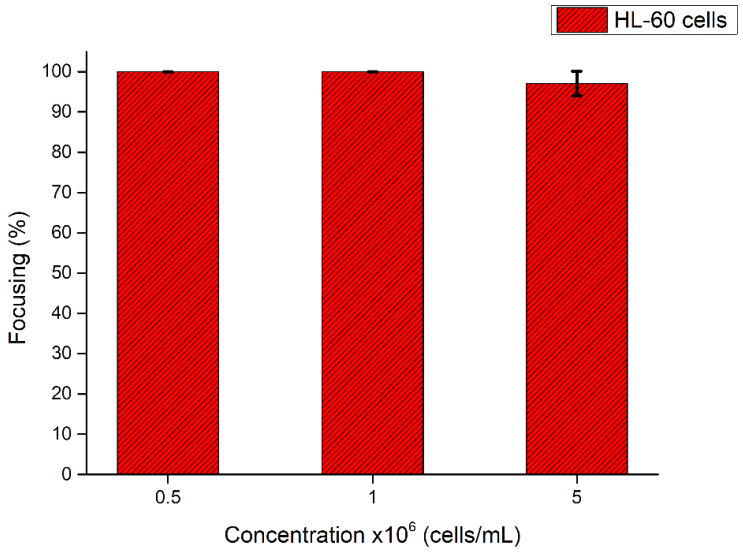

Figure 3.3.12 Focusing performance of the BAW device as a function of cells concentrations from counting chamber Bürker analysis. Cells were injected at 3 µL/min when 50.59 V_{pp} were applied to the transducer while the device was actuated at its resonance frequency of 4.623 MHz.

A validation of the focusing capability of the BAW device with cells tested with a concentration of 5×10^6 cells/mL, was also demonstrated through a UV-Vis characterization and image analysis. In detail, this cells concentration was selected among the other ones either to compare this result with ones obtained with micro and nanoparticles tests and to collect a higher number of cells at the outlets after focalization tests, so to better characterize them in the optics of developing this device as a LOC.

Before performing UV-Vis characterization, as already mentioned for particles analysis (see **2.3.5**), a linear calibration curve was determined for HL-60 cells to provide a correct quantification of cells concentration at each outlets (**Figure 3.3.13**). In detail, the regression equations fit properly with the data since the R^2 value was 0.9911.

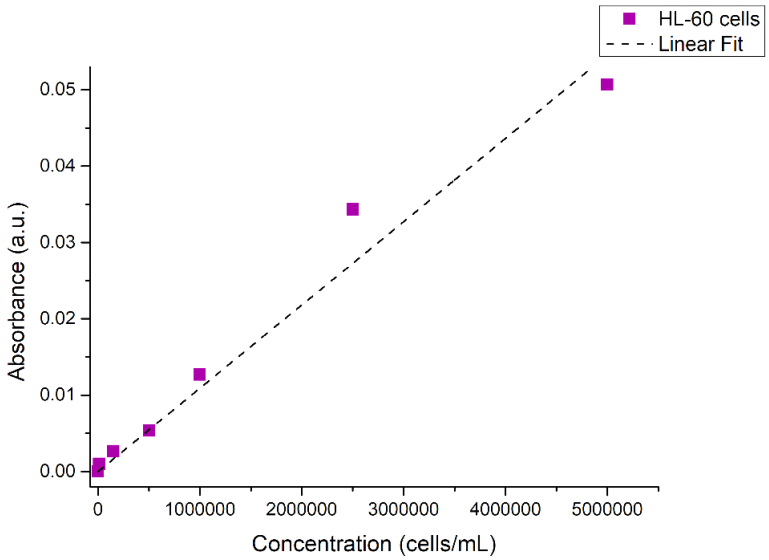

Figure 3.3.13 Calibration curve of HL-60 cells with regression equation $y = 1.09 \times 10^{-8}x$.

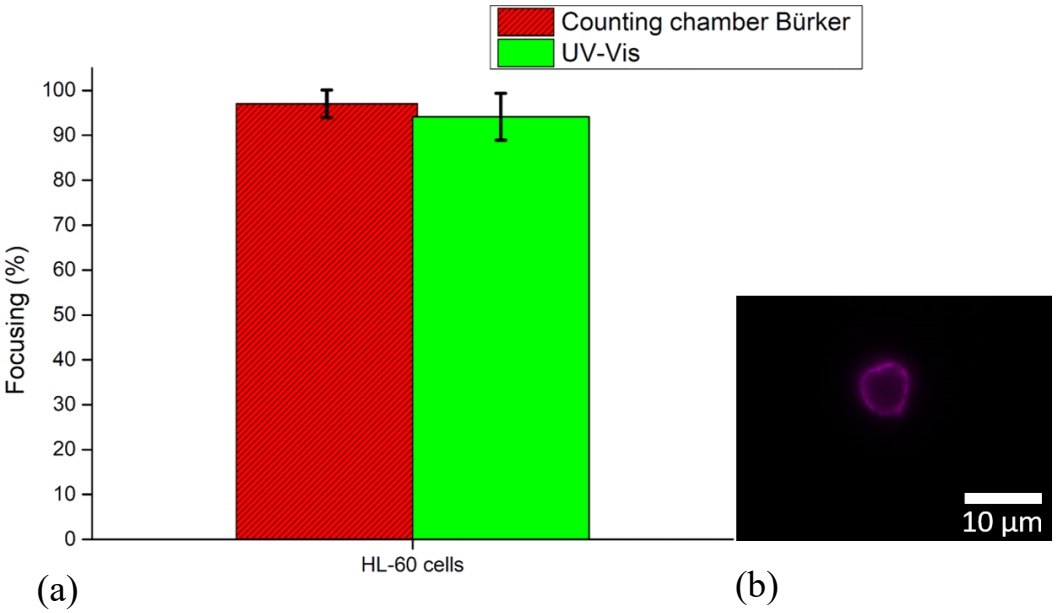

Figure 3.3.14 (a) Focusing performance of the BAW device from counting chamber Bürker analysis and UV-Vis characterization. HL-60 cells concentrated at 5×10^6 cells/mL were injected at 3 µL/min when 50.59 V_{pp} was applied to the transducer while the device was actuated at its resonance frequency of 4.623 MHz. (b) Fluorescence image of HL-60 cell collected at the outlet after the execution of the acoustophoretic test, using 4x objective lens with an exposure time of 20 ms.

Thus, as showed in **Figure 3.3.14**, also from UV-Vis characterization cells were focalized with a percentage value of 94%, validating the previous analysis method, by which the 97% of cells collected at the outlets were focalized at the pressure node. Finally, a further proof was given by the time-lapse image analysis, where cells were acquired in line at the center of the microfluidic channel when the acoustic field was applied (**Figure 3.3.15**).

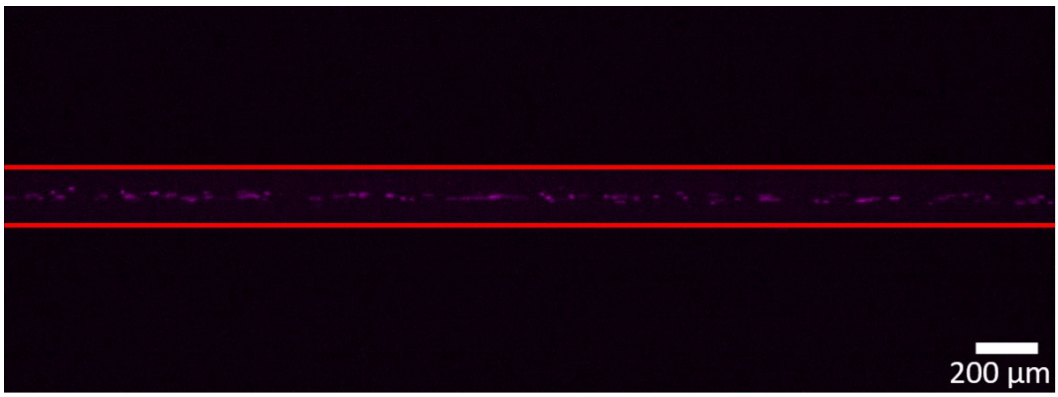

Figure 3.3.15 Frame of time-lapse acquired during the acoustophoretic test, when HL-60 cells concentrated at 5×10^6 cells/mL were injected at 3 µL/min when 50.59 V_{pp} was applied to the transducer while the device was actuated at its resonance frequency of 4.623 MHz. Image acquired with 4x objective lens with an exposure time of 30 ms.

Afterwards, due to the good focalization performance of the BAW device detected when HL-60 cells concentrated at 5×10^6 cells/mL were used, it was investigated at an increased flow rate. In details, experiments were performed leaving the same parameter of applied voltage as previous tests, while a flow rate value of 20 µL/min was imposed. Therefore, the capability of the device to focus cells at the pressure node was evaluated either through a UV-Vis analysis and a counting chamber Bürker analysis. **Figure 3.3.16** reports focusing values of 92% and 88% from UV-Vis analysis and counting chamber Bürker one, respectively. These encouraging data demonstrated that the device could be used to collect an increased number of cells in a reduced time without affecting the focusing capability.

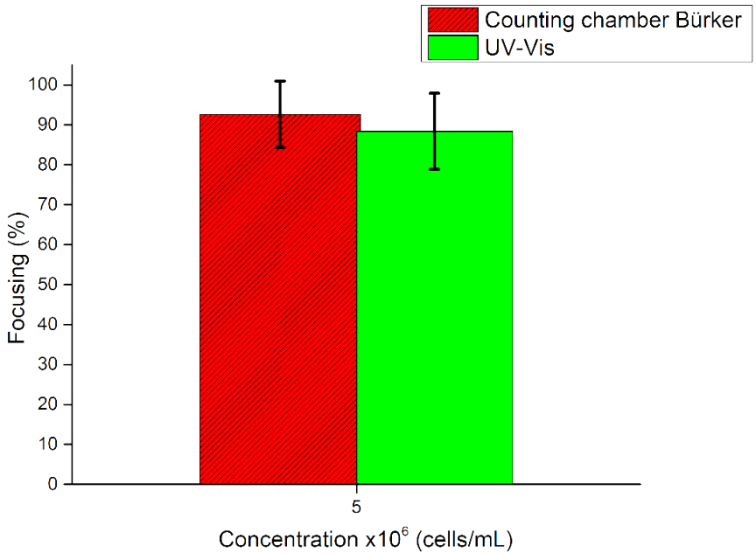

Figure 3.3.16 Focusing performance of the BAW device from counting chamber Bürker analysis and UV-Vis characterization. HL-60 cells concentrated at 5×10^6 cells/mL were injected at 3 µL/min when 50.59 V_{pp} was applied to the transducer while the device was actuated at its resonance frequency of 4.623 MHz.

Further tests were performed with a mixed population composed by HL-60 cells and 1MPs at first and then with HL-60 cells and NPs both of them in 1:1 cells:M/NPs ratio.

Since results were obtained through a UV-Vis analysis, also in this case was necessary to supply linear calibration curves of mixed populations. As follows, calibration curves related to cells involved in tests when they were mixed with micro and nanoparticles are reported. Indeed, while absorbance values of micro and nanoparticles curves were the same either when they were evaluated in a single or a mixed population, a little discrepancy between cells absorbance values of relative calibration curves was denoted. These curves, with their relative regression equations are shown in **Figure 3.3.17**. In details, for the mixed population composed by cells and 1MPs solution R^2 corresponded to 0.9983 while for the solution characterized by cells and NPs it was 0.9963.

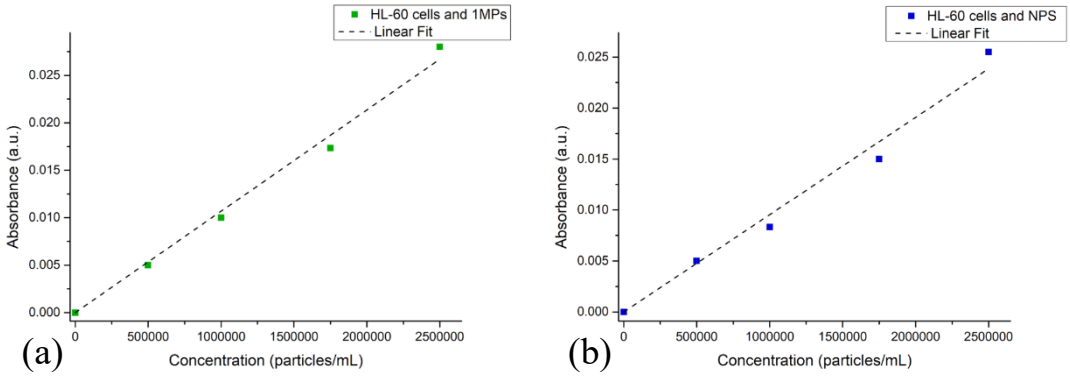

Figure 3.3.17 Calibration curves: (a) HL-60 cells and 1MPs (1:1) with regression equation $y = 1.07 \times 10^{-8}x$ and (b) HL-60 cells and NPs (1:1) with regression equation $y = 9.55 \times 10^{-9}x$.

Tests performed with mixed populations of cells and particles were executed by applying 50.59 V_{pp} to the transducer, actuating the microfluidic channel at its resonance frequency and by injecting solutions at a flow rate equal to 3 µL/min. This last value was preferred to 20 µL/min since by this it was possible to obtain the higher collection of cells at the node of the device. In detail, the mixed population composed by cells and 1MPs, was characterized by HL-60 cells with a density equal to 2.5×10^6 cells/mL and 1MPs concentrated at 2.5×10^5 particles/mL. Instead, the other population was composed by the same density of cells mixed with NPs concentrated at 1.8×10^5 particles/mL.

Also in this case, as demonstrated previously with particles (see **3.3.3**), the manufactured BAW device was not able to collect 1MPs and NPs at the pressure node of the microfluidic channel (**Figure 3.3.18** and **Figure 3.3.19**). Indeed, the percentage of 1MPs and NPs focalized at the node was 52% and 50%, respectively. Concerning focalization values of HL-60 cells, they were 92% when they are mixed with 1MPs and 88% when they are mixed with NPs. Thus, comparing cells focalization results obtained when they were in a mixed dispersion and when there

were only cells dispersed in PBS, a little reduction was observed as in the case of micro and nanoparticles.

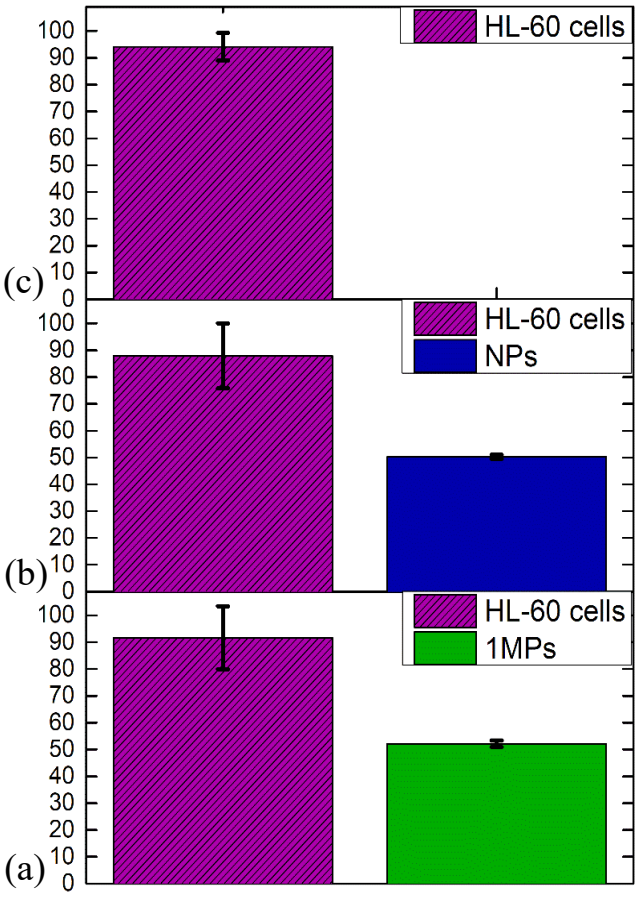

Figure 3.3.18 Focusing performance of the BAW device throughout a UV-Vis characterization: (a) HL-60 cells concentrated at 2.5×10^6 cells/mL, (b) HL-60 cells concentrated at 2.5×10^6 cells/mL mixed with 1MPs concentrated at 2.5×10^5 particles/mL and (c) HL-60 cells concentrated at 2.5×10^6 cells/mL mixed with NPs concentrated at 1.8×10^5 particles/mL. Mixed populations were injected at 3 µL/min when 50.59 V_{pp} was applied to the transducer while the device was actuated at its resonance frequency of 4.623 MHz.

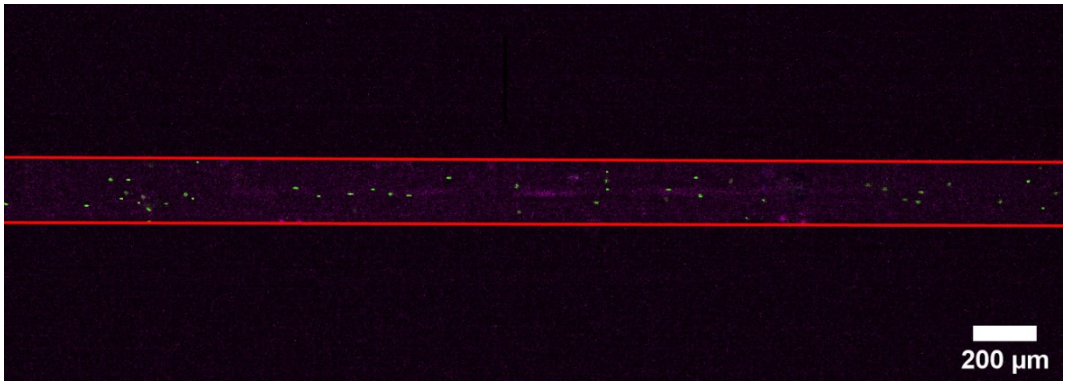

Figure 3.3.19 Frame of time-lapse acquired during the acoustophoretic test, when the mixed population of HL-60 cells concentrated at 2.5×10^6 cells/mL and 1MPs 2.5×10^5 particles/mL were injected at 3 µL/min when 50.59 V_{pp} was applied to the transducer while the device was actuated at its resonance frequency of 4.623 MHz. Image acquired with 4x objective lens with an exposure time of 20 ms for cells and 9.8 ms concerning 1MPs.

To end, latest HL-60 cells focalization results obtained were also characterized by a counting chamber Bürker method, which evaluated a percentage of cells collected at the node equal to 100% in both cases (**Figure 3.3.20**). Apparently focalization average mean values between the two characterization methods presented a higher discrepancy, but considering measurement standard deviations they well fitted. Indeed, UV-Vis measurements, owning lower focusing percentage values presented higher standard deviations and vice versa considering counting chamber Bürker analysis.

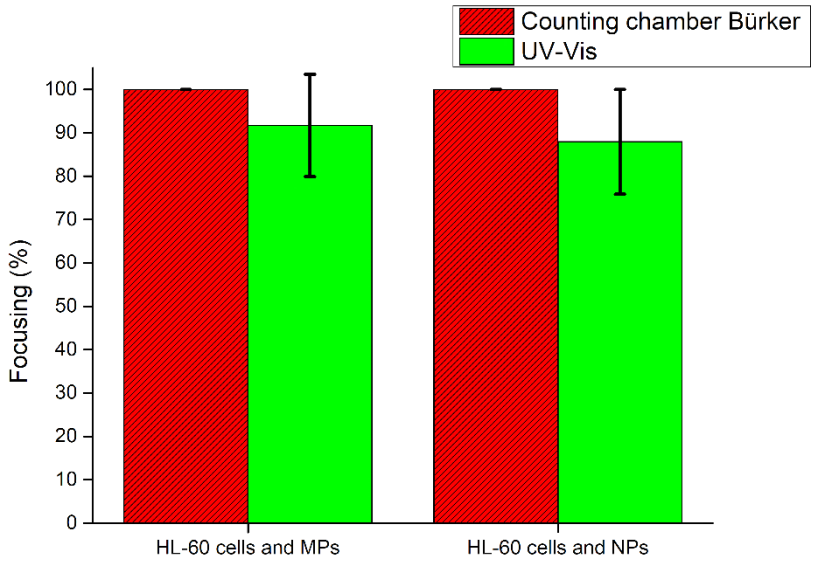

Figure 3.3.20 Focusing performance of the BAW device from counting chamber Bürker analysis and UV-Vis characterization: (a) HL-60 cells concentrated at 2.5×10^6 cells/mL mixed with 1MPs concentrated at 2.5×10^5 particles/mL and (b) HL-60 cells concentrated at 2.5×10^6 cells/mL mixed with NPs concentrated at 1.8×10^5 particles/mL. Mixed populations were injected at 3 µL/min when 50.59 V_{pp} was applied to the transducer while the device was actuated at its resonance frequency of 4.623 MHz.

3.4 Conclusion

This work investigated the separation potentiality of a silicon-based bulk acoustic wave resonator, characterized by a standard fabrication process, as label-free LOC. In details, the focalization performance was evaluated exploiting either polystyrene micro and nanoparticles and adhesion cells as single or mixed populations. Analyzing samples collected at the outlets it was possible to quantify device focalization values, at different setting conditions, either via a UV-Vis characterization and throughout images analysis. Results reported the 97% of collection of micro particles at the node of the microfluidic channel when lower concentration, lower flow rate and higher applied voltage to the piezoelectric element were imposed. In addition, after having calculated the experimental acoustic energy, and imposing this value to the simulated analyses, it was possible to compare micro particle focusing values obtained at different concentrations with simulated ones. These data well fitted the micro particles focalization trend at different sample concentrations, with a maximum discrepancy of 7%.

As suggested from the analytical evaluation of the critical particles diameter, the ability of collecting particles at the node of the microchannel worsen with particles of small sizes, indeed the acoustic force was not able anymore to focalize particles of size equal or below 1.6 μm as demonstrated either when samples were composed by a population of 1 μm particle sizes or when nanoparticles mixed with micro particles were exploited as samples.

Tests performed with cells highlighted an optimal separation performance even at high flow rate. Indeed, a focalization of 92% was evaluated at a flow rate equal to 20 μL/min. Cells focalization performances were demonstrated also when they were used within micro and nanoparticles. In detail, average focalization values moved from 97%, when cells were alone, to 92% or 88% when they were mixed in samples with micro and nanoparticles, respectively.

Finally, since the presented device could be exploited in the future to develop a LOC for the early diagnosis or some specific target therapies, further work will be performed to optimize the separation between different kinds of cells or biomarkers owing different mechanical properties as shapes, sizes and densities. Thus, a buffer sheath fluid or a solution characterized by enhanced densities or viscosities with respect to the sample mechanical characteristics will be investigated.

Chapter 4

Polydimethylsiloxane device

4.1 Introduction

4.1.1 State-of-the-art of polydimethylsiloxane-based microdevices

In the last few decades, polydimethylsiloxane (PDMS), a silicone elastomer with charming properties, has been widely used for fabricating LOC and microfluidic analysis platforms surpassing silicon and glass materials[165][166].

PDMS is a flexible polymer owing isotropic and homogeneous properties composed by mixing a base polymer and a cross linker. Varying the cross linker concentration, it is possible to change physical and mechanical properties of PDMS. In details, PDMS is chemically inert, water impermeable, thermally stable, gas permeable, optically transparent down to approximately 256 nm and biocompatible[167][168][169][170][171]. Currently, it is one of the most actively developed polymers for microfluidic devices production both in academia and industry, since it is easy to handle and manipulate and it requires low-cost fabrication processes such as soft-lithography techniques and further additive manufacturing methods, which enable easy prototyping and mass production[172][173][174][175].

Concerning the biological field, the development of PDMS-based microfluidic devices, thanks to their properties, allows integrating in a cost-effective manner the whole analytical process reducing analysis time, complexity and samples and reagents volumes. In details, PDMS-based LOCs present in literature are used for sample purification, cell culture and analysis, DNA sequencing, molecular tests for nucleic acids and proteins[176][177][178][179]. Moreover, exploiting PDMS mechanical properties, microfluidic devices are also used to develop miniaturized electronic gadget as wearable sensors and to form three-dimensional micro valves and pumps into a microfluidic network[180][181]. Furthermore, recent applications rely on the employment of PDMS-based microfluidic devices either as Organ On a Chip and as biomimetic tools, where the PDMS mimics organs and complex tissues[182][183][184][185](**Figure 4.1.1**).

Thus, due to the promising features of PDMS-based microdevices, the perspective of implementing biomedical compact, rapid, easy-to-use microfluidic molecular tests is still an open challenge. Then in this context, a novel PDMS-based microdevice was developed for the purification and direct detection of microRNA biomarkers and it is presented in this chapter.

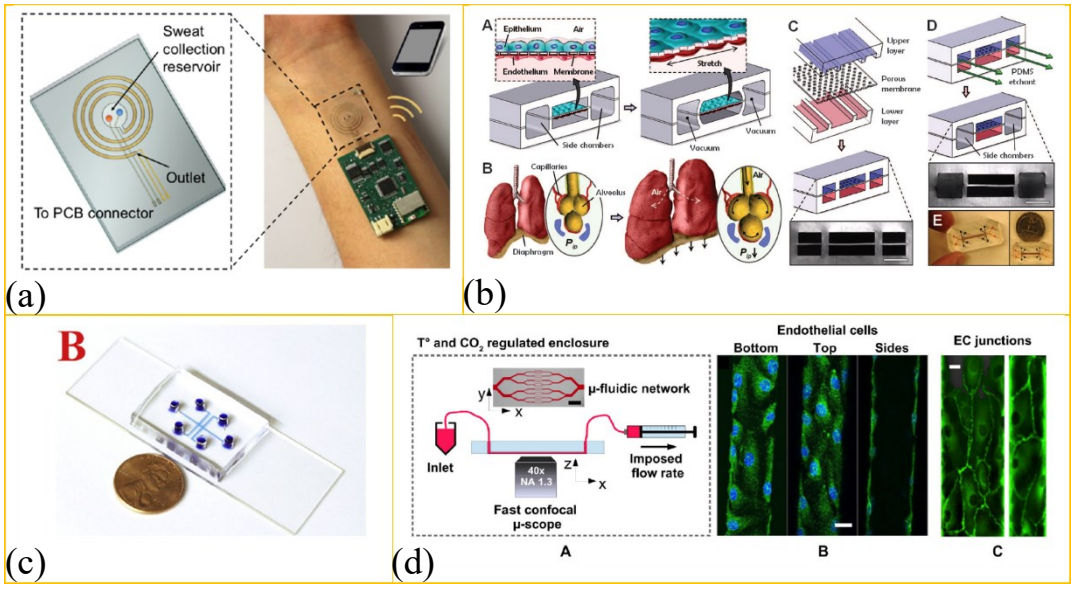

Figure 4.1.1 Examples of PDMS-based microdevices: (a) wearable microfluidic sensing patch. Image from[180], (b) organ on a chip. Image from[182], (c) electrophoresis-grade device. Image from[178] and (d) microvasculature on chip. Image from[185].

4.2 Materials and methods

4.2.1 Design

Microfluidic devices characterized by higher surface-to-volume (S/V) ratio represent an essential aspect in order to adsorb higher amounts of biomarkers. Thus, this chapter reported an enhancement of the previous PDMS-based microdevice [166][177] focused on an increased chip S/V ratio.

Two spiral-shape microdevice configurations provided with different S/V ratios, with the constraint of having a volume equal to 13 µL, were designed by a 3D computer aided design (CAD) software (Rhinoceros®). In details, the first spiral microdevice (from now called Chip A) was designed with a channel characterized by a squared section 200 µm wide and 200 µm deep and with walls spacing width of 200 µm. At the same time, the second microdevice configuration (from now called Chip B) was defined by a rectangular cross section 60 µm wide and 200 µm deep and with walls spacing 150 µm wide. Both spiral-shape configurations were characterized by two inlet/outlet ports having a diameter of 1.5 mm, where one was sketched in the center of the layout while the second one was placed at the periphery (**Figure 4.2.1**).

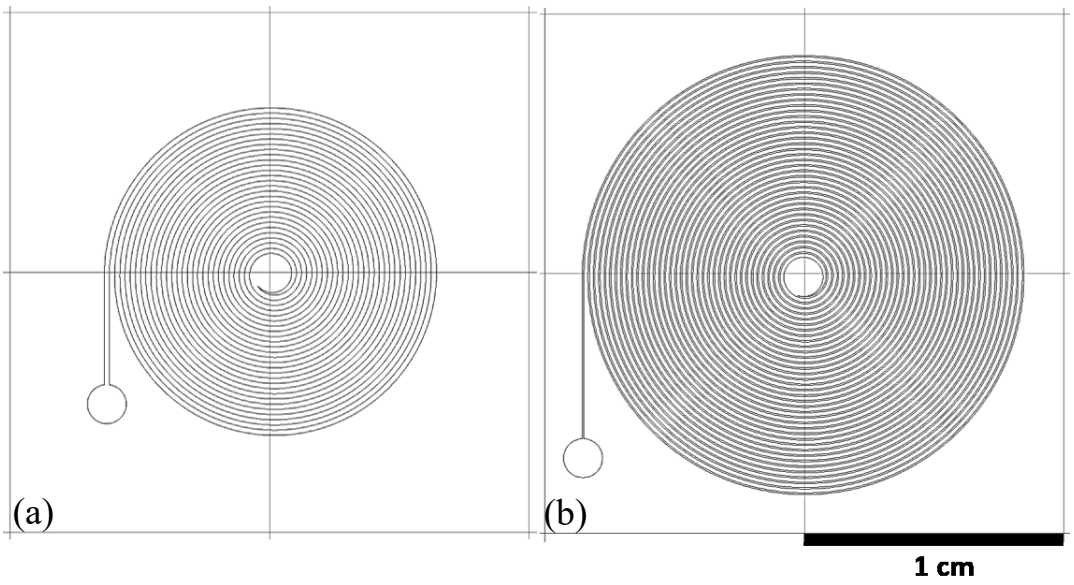

Figure 4.2.1 2D draw of the spiral-shape microdevices: (a) Chip A and (b) Chip B.

As reported in **Table 4.2.1** the two spiral-shape microdevices were defined by a different channel length. While for Chip A it was 650 mm for Chip B it corresponded to 2160 mm. Thus, an enhancement of the S/V ratios of the spiral-shape microdevices compared to the previous PDMS-based microdevice[166][177] was depicted in **Figure 4.2.2** and in **Table 4.2.1**. In details, the increased S/V was evaluated as the quotient between each spiral-shape S/V ratio and the previous

PDMS-based microdevice S/V value. Thus, Chip A was 4.45 times greater than the previous PDMS-based microdevice, while Chip B 9.63 times bigger.

Dimensions	Previous microdevice	Chip A	Chip B
Surface (S) (mm^2)	58.50	261.54	561.73
Volume (V) (μL)	13.00	13.07	12.96
S/V (1/mm)	4.5	20.01	43.35
$(S/V)/(S/V_{previous\ microdevice})$	1	4.45	9.63

Table 4.2.1 Geometrical characteristics of: previous PDMS-based microdevice, Chip A and Chip B.

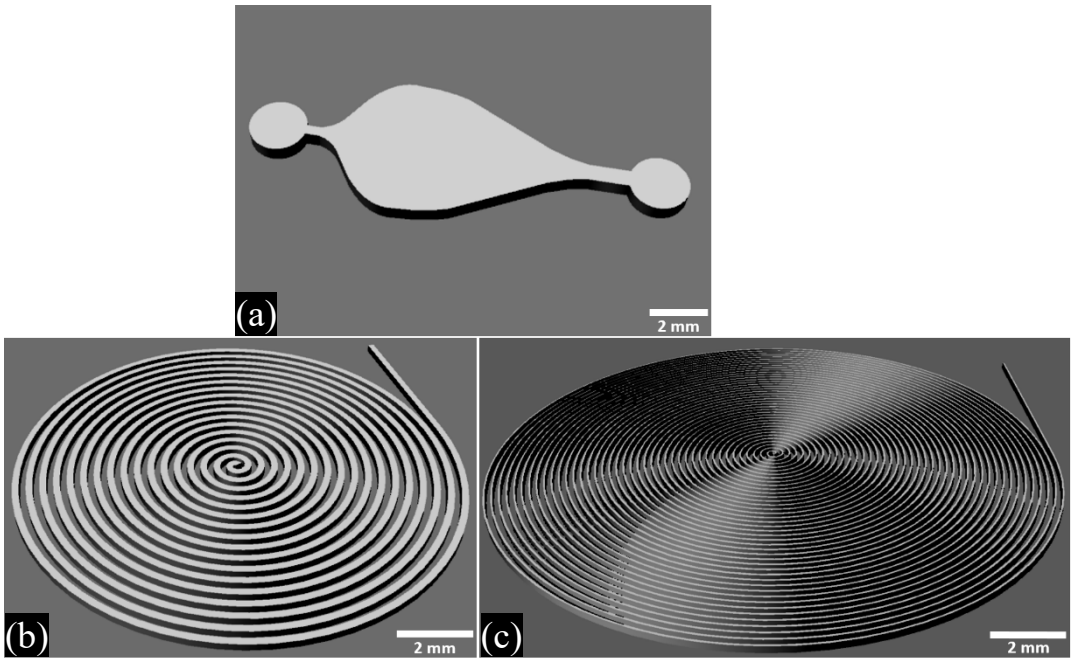

Figure 4.2.2 3D CAD designs: (a) previous PDMS-based microdevice, (b) Chip A and (c) Chip B.

4.2.2 Device fabrication

Both microfluidic devices were fabricated as follows: firstly, the PDMS (SYLGARD® 184 elastomer) microfluidic pattern was obtained through a mold-casting step and finally it was bonded on a silicon support coated by a thin layer of PDMS.

Therefore, the fabrication of PDMS microfluidic devices began with the preparation of the SU-8 mold (see **Appendix B** for silicon mold). A silicon wafer support was coated by SU-8 3005 (Microchemicals GmbH) using a spin coater (Spinner 150 Wafer Spinner) by setting 10 seconds at 500 rpm and 60 seconds at 2000 rpm. Then a soft bake process was run in two thermal steps: the first one at 65 °C for 8 minutes and the second step at 95 °C for 80 minutes, both performed on

the hot plate. Next, the SU-8 was exposed for 30 seconds to standard UV photolithography by means of a double side mask aligner (Neutronix Quintel NXQ 4006) used in contact mode, ensuring the correct alignment between the SU-8 and the desired mask patterns. As the previous soft bake step, the post bake was characterized by two thermal steps: the first at 65 °C for 5 minutes and the second one at 95 °C for 25 minutes, on a hot plate. After that, to obtain the finished mold, the SU-8 was developed using Propylene glycol methyl ether acetate (PGMEA) for 20 seconds, then rinsed with 2-propanol (Sigma-Aldrich) and dried with a nitrogen flux. Finally, the released SU-8 features were hard baked at 170 °C for 15 minutes to stabilize them and to ensure the complete removal of the solvent.

To guarantee the correct PDMS detachment from the mold, a silanization step was applied on the SU-8 surface employing trichloromethylsilane (CH_3SiCl_3) and toluene in a 1:10 ratio. Thus, before silanization, an O_2 plasma treatment was performed on the mold surface by setting 300W and an O_2 flux equal to 30% for 1 minute. Next, mold surfaces were silanized through a wet phase for 4 hours, rinsed with 2-propanol and then dehydrated on a hot plate at 170 °C for 10 minutes. Finally, the mold casting of both spiral microfluidic patterns was performed by pouring the PDMS on the mold and the curing step was accomplished on a hot plate at 120 °C for 15 minutes. Before that, PDMS was prepared by manually merging the pre-polymer and the curing agent in a 10:1 ratio and degassing it. Next, the freshly cured spiral patterns were manually detached from the mold. Inlet and outlet ports were punched through a biopsy puncher and subsequently chips were cleaned with 2-propanol and dehydrated on a hotplate at 70 °C for 5 minutes.

Meanwhile silicon wafer slices, acting as supports, were pre-cut in squares of two different dimensions (21x21 mm^2 and 24x24 mm^2), cleaned with a solution of sulphuric acid and hydrogen peroxide in a 3:1 ratio (v/v) for 10 minutes, rinsed 3 times in water and dried with a nitrogen flux. After that, silicon slices were coated with a thin layer of PDMS by means of a spin coater (Spinner 150 Wafer Spinner) with the following protocol: 5 seconds at 500 rpm and 60 seconds at 3000 rpm and cured on a hot plate at 120 °C for 5 minutes. The spiral structures were then bonded on the silicon slices through a standard O_2 plasma treatment setting 300 W of power and fluxing the 60% of O_2 for 2 minutes. To conclude, once assembled, microfluidic devices were located in the oven at 90 °C for one hour to improve the bonding between the two components. **Figure 4.2.3** sketched the process flow of the spiral-shape microdevices.

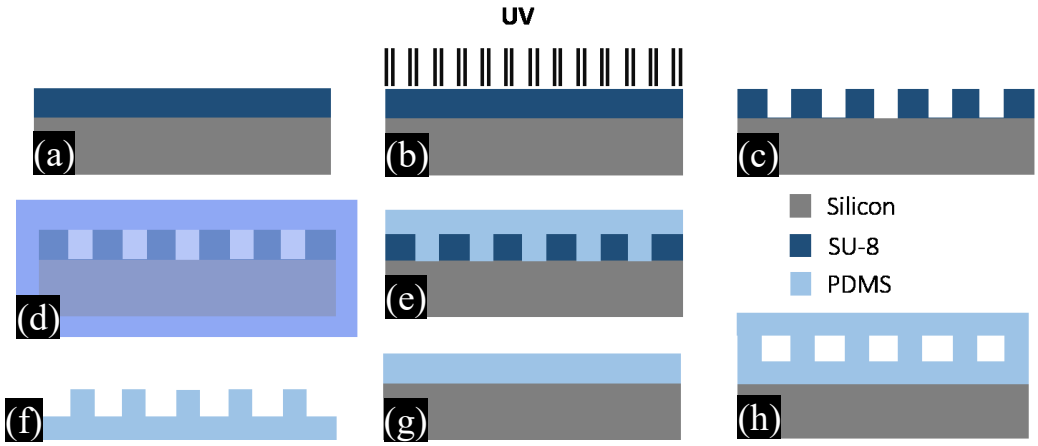

Figure 4.2.3 Fabrication process flow: (a) SU-8 spinning on silicon wafer, (b) SU-8 exposition, (c) SU-8 development, (d) SU-8 mold silanization, (e) PDMS pouring on SU-8 mold, (f) PDMS spiral replica, (g) silicon slice with PDMS thin layer and (h) final device assembled.

4.2.3 Device characterization methods

Device cross sections were characterized both with an optical microscope (Leica DVM 2500) and a field emission scanning electron microscope (Zeiss Supra 40 FE-SEM) to inspect the microchannels dimensions. In particular, to perform FE-SEM analyses, devices were cut perpendicularly to the microfluidic pattern and then metalized with a thin layer of Chromium.

PDMS chemical characterization was carried out by X-ray photoelectron spectroscopy (XPS) using a Kratos Axis Ultra DLD instrument (Kratos Analytical) equipped with a hemispherical analyzer and a monochromatic Al Kα (1486.6 eV) X-ray source, in spectroscopy mode. Slices of PDMS devices were studied with a take-off angle between the analyzer axis and the sample surface of 0°, corresponding to a sampling depth of approximately 10 nm. A charge neutralizer, set at the bottom of the electrostatic input lens systems, was employed to compensate the charge. Then, for each sample, a survey (in the 1300, −5 eV energy range) was recorded inside and outside microchannels in order to examine the presence of impurities derived from the fabrication process. Next, referring to the PDMS value reported in literature [186], survey spectra were aligned setting C 1s core level peak at 284.38 eV. Finally, the quantification, reported as relative elemental percentage, was carried out extracting core levels from the survey spectra. All XPS data were analysed using the software described in Speranza and Canteri [187].

4.2.4 Experimental Setup and on-chip functionalization

Proper PMMA holders were employed to handle PDMS microdevices during each experiment and inlet and outlet fluorinated ethylene propylene (FEP) tubes

(IDEX, OD = 1.6 mm, ID = 0.5 mm) were manually inserted into the device's proper ports. A syringe pump system (Legato 185, KD Scientific,Holliston) was used to inject liquids inside spiral-shape devices to deliver solutions with defined flow rates in all steps of this work. Silanization and washing solutions were preloaded in plastic syringes (Terumo syringe, 2.5 mL), while for microRNAs injection a glass syringe (Hamilton Gastight 1700, 750 µL) was used. Plastic and glass syringes were connected with FEP tubes through standard OmniLok fittings (Omnifit Labware).

Before each test, internal surfaces of microdevices were cleaned via a plasma treatment. In details, an argon plasma was performed by setting a pressure equal to 2 mbar and applying a power of 10.5 W to an RF coil for 2 minutes. Then, the silanization step into PDMS microdevices was achieved with a solution composed by 0.1% (v/v) of (3-Aminopropyl)trimethoxysilane (APTMS) (Sigma-Aldrich) and 0.9% (v/v) of 2-[Methoxy-(polyethyleneoxy)pro-pyl]trimethoxysilane, tech-90, with 6–9 C_2H_4O units (PEG-s) (Fluorochem) diluted in 99.8% (v/v) ethanol (Sigma-Aldrich). In detail, the organosilane mix was fluxed at 10 µL/min to fill the microdevice and once full, it was set in a hot water bath at 60 °C for 5 minutes, meanwhile the organosilane mix solution was continuously injected at a flow rate equal to 2 µL/min (**Figure 4.2.4**). Preliminary silanization experiments were executed at different times in order to find the optimal conditions to have whole internal surfaces functionalized. After that, two cleaning steps removed the excess of organosilane compounds. The first one was performed by infusing a volume of ethanol equal to 10 times the spiral device volume at 25 µL/min, while the second cleaning step was performed using the same setting of the previous one, but instead ethanol in this phase distilled DNAse/RNAse free water was employed (**Figure 4.2.5**).

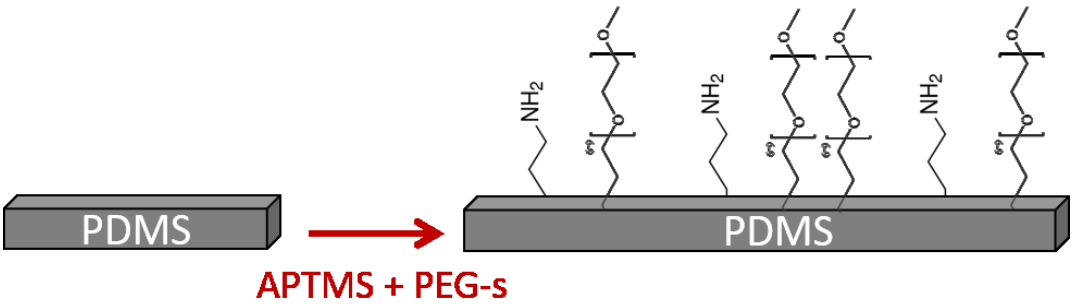

Figure 4.2.4 On-chip functionalization process.

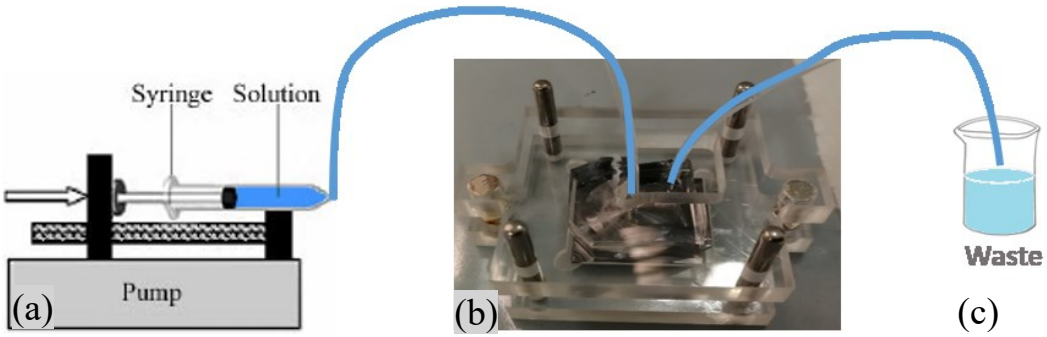

Figure 4.2.5 Experimental setup: (a) syringe pump, (b) PDMS microdevice and (c) beaker for waste.

4.2.5 MicroRNAs functional assay and Real-Time PCR

After having silanized PDMS microdevices internal surfaces, a solution composed by microRNAs was injected into the chip at different flow rates, by changing the microsyringe parameters, to determine the optimal operation conditions both concerning microRNAs injection step and the subsequently washing one.

Therefore, a functional assay with synthetic fluorescently-labelled hsa-miR-1246 (50-TAMRA-AAUGGAUUUUUGGAGCAGG-30, herein named miR-1246-TAMRA) (IDT Integrated DNA Technologies) was performed to investigate chips performances. In detail, the miR-1246-TAMRA spiked firstly in water and then in human plasma, was pumped in the microdevice at a flow rate of 10 µL/min. Then, after a washing step with water at 1 µL/min for 10–15 minutes, the adsorbed microRNAs on chip walls was investigated both by fluorescence and confocal microscopy (

Figure 4.2.6).

Fluorescence characterizations were performed through a microscope (Leica DMLA) equipped with a mercury lamp employing the fluorescence filter L5 (Leica Microsystems). Microdevices were observed with a 2.5x magnification objective and images were acquired with a cooled CCD camera (DFC 420C, Leica Microsystems). The microscope motorized stage was controlled through a BeanShell script running in MicroManager (version 1.4.23, micro-manager.org) to acquire 54 images necessary to recreate an image having the whole spiral patterns. Finally, images analyses and reconstruction of them were executed with the Fiji software [188] and Fiji custom macros.

Confocal imaging was performed with a Leica SP5-II confocal microscope (Leica Instruments) equipped with a helium/neon laser source with an excitation wavelength at 543 nm. Samples were observed utilizing a 20x objective lens and z-stacking mode was set from the top to the bottom of the microchannel. Firstly, PDMS spiral patterns were detached from the silicon support and subsequently chip microchannels were cut with a scalpel at 30° with respect to the normal surface to help the microRNAs visualization on walls. To acquire the TAMRA signal,

fluorophores were excited with the helium/neon laser, using an emission detector wavelength range from 570 to 660 nm.

In addition, a spectrofluorimeter (FluoroMax-4, Horiba Jobin Yvon) was used to measure the unbound microRNAs collected from chips silanized at different times. This was performed by employing an excitation wavelength of 552 nm and recording the emission spectrum from 557 to 700 nm and, finally, values were defined by integrating the area between 580 and 590 nm.

On-chip microRNAs purification and detection were validated with synthetic microRNAs dissolved in distilled DNAse/RNAse free water (named water herein) (Gibco) or in blood plasma. In detail, three different microRNAs were employed: miR-20a (50-UAAAGUGCUUAUAGUGCAGGUAG-30), miR-222 (50-AGCUACAUCUGGCUACUGGGU-30) and miR-320 (50AAAAGCUGGGUUGAGAGGGCGA-30) (IDT Integrated DNA Technologies). Purification of synthetic microRNAs was performed by spiking synthetic microRNAs ranging from 0.1 pg to 1 ng either in water or in human plasma mixed in a 1:1 ratio with APL 1 buffer (QIAamp UCP Pure Pathogen Blood kit, called lysis buffer) (Qiagen).

Human plasma was obtained from blood samples collected from healthy donors into EDTA-treated collection tubes. Concerning plasma preparation, fresh blood was centrifuged at 700 g for 10 minutes to pellet the cell fraction, then the supernatant was collected avoiding contact with the buffy coat. Before employing plasma for experiments, plasma samples were centrifuged at 1000 g for 5 minutes at 4 °C to pellet the debris. Afterwards, the relative amount of synthetic microRNA diluted both in water and in plasma was pumped in the microdevice at a flow rate of 10 μL/min for 20 minutes at room temperature. At this step, the amino-silanized surfaces provided positive charges to the chip channels allowing to attract negative charges settle on the phosphate groups of the injected microRNAs backbones. Then, to remove the excess of microRNAs, a wash step with water was performed at 1 μL/min for 10–15 minutes.

For the microRNAs on-chip analysis, a two-steps protocol based on reverse transcription coupled with real-time PCR was employed. Reverse transcription (RT) was performed directly on-chip, on the miRNAs adsorbed by PDMS internal surfaces by adding the TaqMan® MicroRNA Reverse Transcription Kit (ThermoFisher Scientific) master mix at 10 μL/min into the microdevice. This master mix included 100 mM dNTPs (with dTTP), MultiScribe Reverse Transcriptase (50 U/μL), 10x Reverse Transcription Buffer, RNase Inhibitor (20 U/μL), 20x miR-specific RT primers. In detail, the reaction was perfomed for 30 minutes at 16 °C, 30 minutes at 42 °C, and 5 minutes at 85 °C on a XP Thermal cycler (Bioer Technology Co., Ltd.) equipped with a flat thermal block. Once synthetized, cDNA was subsequently recovered from the microdevice with the help of microsyringes and amplified with TaqMan® MicroRNA Assay—hsa-miR-specific (ThermoFisher Scientific) in standard conditions (

Figure 4.2.6). An amount of 20 μL of real-time PCR mix was composed of TaqMan® Small RNA Assay (20x), TaqMan® Universal PCR Master Mix II (2x) (ThermoFisher Scientific), nuclease-free water and cDNA, following the

manufacturer's instructions. The cycling protocol, 95 °C for 10 minutes and 45 cycles of 95 °C for 15 seconds and 1 minute at 60 °C was run on a CFX Connect™ Real-Time PCR Detection System (BioRad). Samples were amplified in triplicates and non-templates controls were included (amplification negative control). Data were analyzed with BioRad CFX Manager 2.1 software and threshold cycles (Ct) were reported and compared with a standard curve, build with known amounts of cDNA, for quantification.

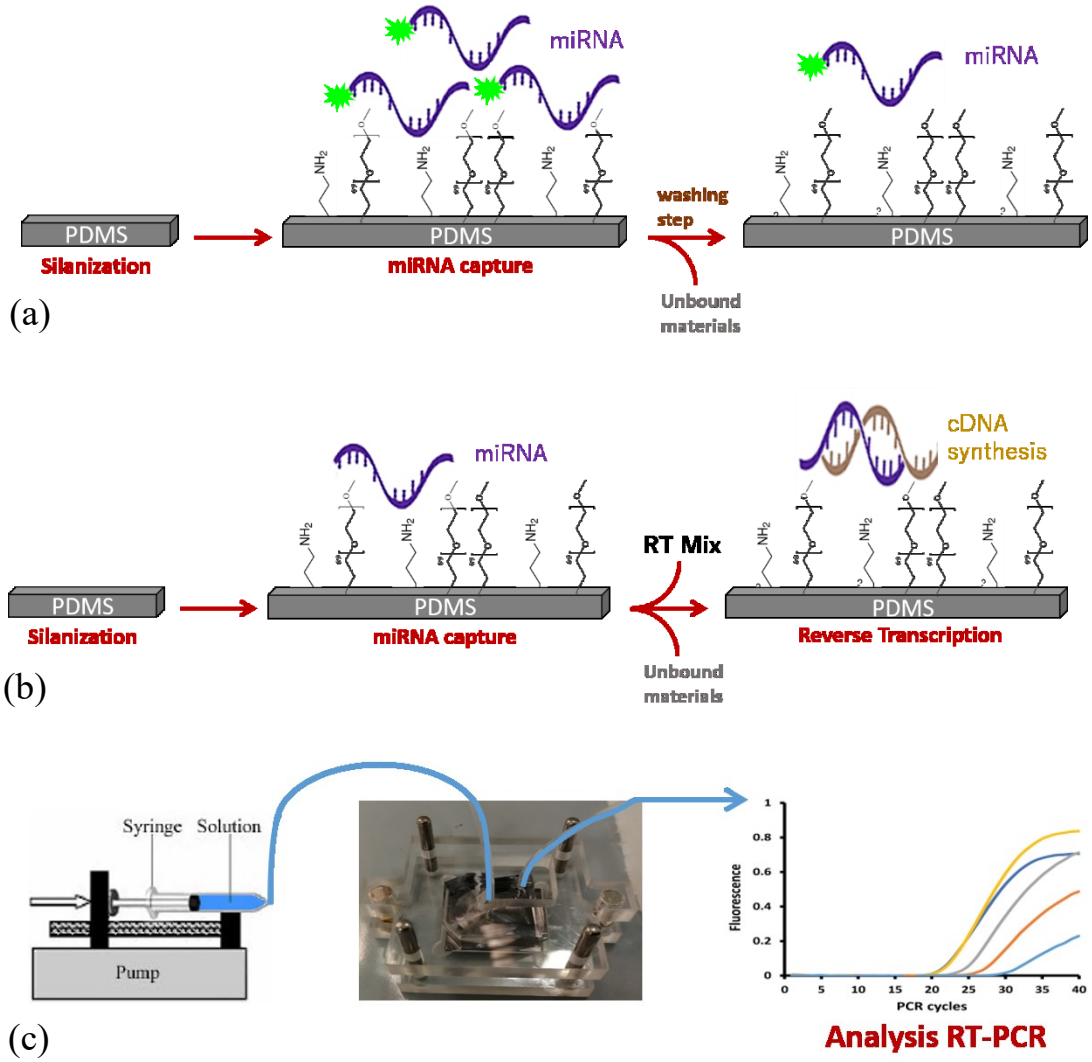

Figure 4.2.6 (a) On-chip microRNAs functional assay, (b) on-Chip microRNAs RT-PCR and (c) experimental setup.

4.3 Results and discussion

4.3.1 Microdevices morphological analysis

Morphological analyses on SU-8 mold and PDMS replicas were performed to evaluate features dimensions of both spiral-shape microdevices. As a first step, during the fabrication process, optical images of SU-8 mold were acquired after developing the SU-8 photoresist to check a correspondence between the mold spiral-shape pattern and the design one **Figure 4.3.1**.

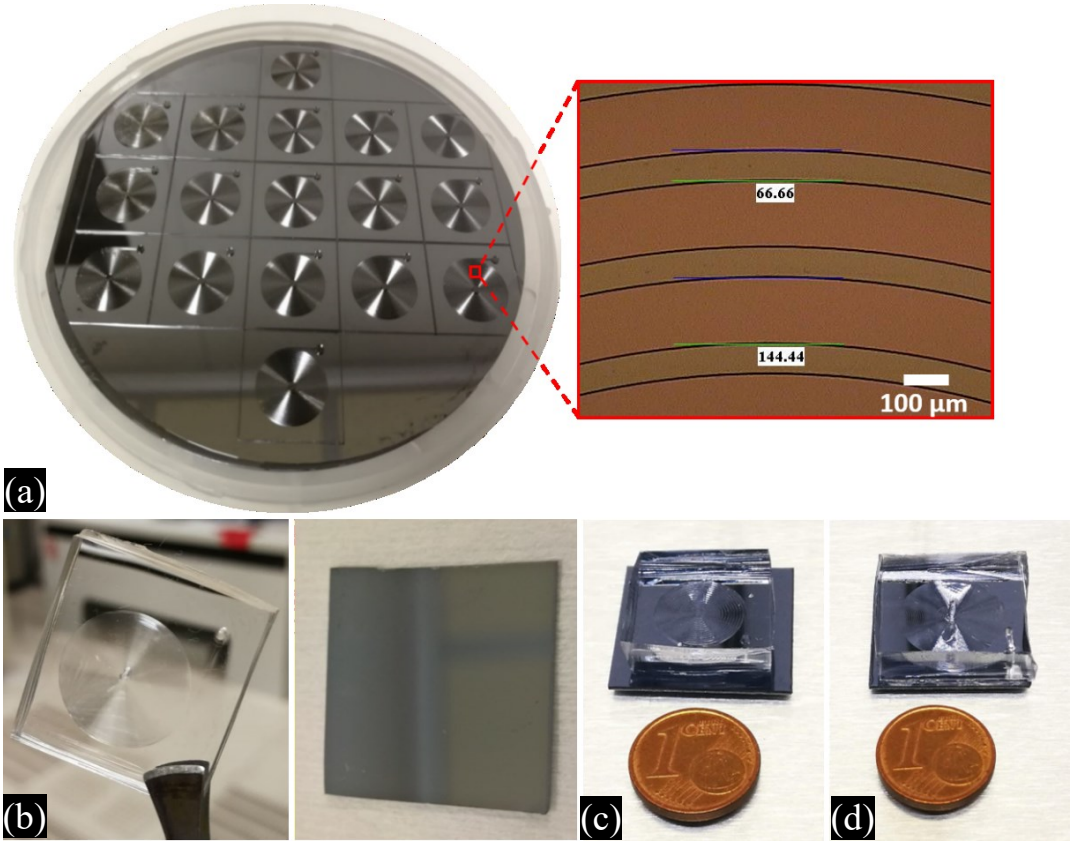

Figure 4.3.1 Optical photographs captured during the spiral-shape fabrication process: (a) SU-8 mold with spiral-shape microdevices having 60 µm wide channels. Inset of a measurement of channel and wall spacing dimensions through an optical microscope with a 10x objective lens, (b) PDMS replica and silicon support coated by a thin layer of PDMS, (c) Chip A and (d) Chip B.

A comparison between the real microchannel dimensions and the design ones was performed on PDMS replicas both through optical microscopy and FE-SEM image analyses (**Figure 4.3.2** and **Figure 4.3.3**). To do this, fifty microdevices for each configuration were sectioned and microchannels width and length as well as wall spacing widths were characterized.

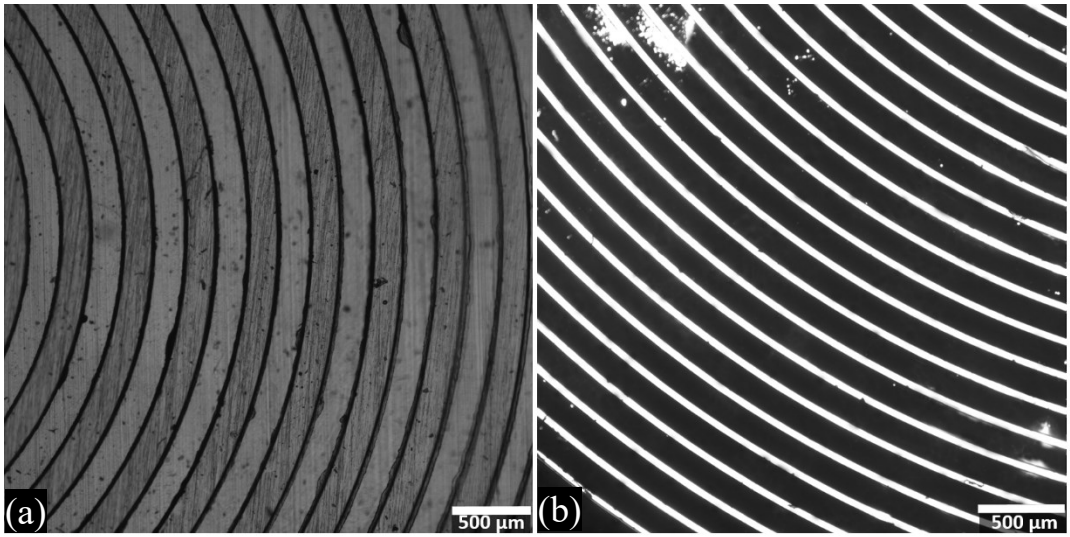

Figure 4.3.2 Optical images of spiral-shape microdevices metalized with Cromium performed with a 4x objective lens: (a) Chip A and (b) Chip B.

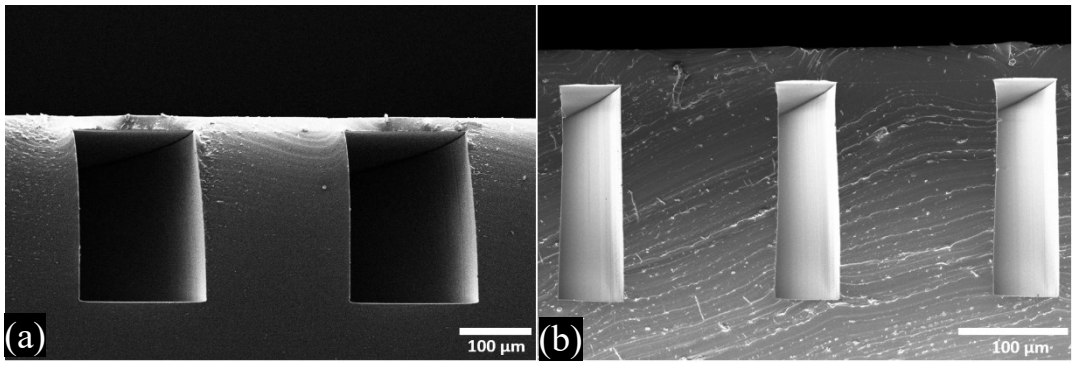

Figure 4.3.3 FESEM images of spiral-shape microdevices: (a) Chip A magnification 400x and (b) Chip B, magnification 600x.

In details, for Chip A microchannels possessed a width average value of 168.41±4.87 µm and a height mean value equal to 222.67±14.63 µm, with a wall spacing of 220.89±14.63 µm. Regarding Chip B microchannels mean values were 58.38±2.30 µm and 195.23±8.41 µm of width and depth, respectively, with wall spacing 146.18±2.54 µm wide. Thus, the mean volume of Chip A corresponded to 15.90 µL while Chip B was characterized by a total volume of 13.20 µL as reported in **Table 4.3.1** and **Table 4.3.2**. To conclude, while Chip B dimensions well fitted with the design ones, Chip A possesses greater dimensions than the design values.

Chip A		
Features	**CAD**	**PDMS-replica mean value**
Surface (S) (mm^2)	261.54	301.92
Volume (V) (μL)	13.07	15.90
S/V (1/mm)	20.01	18.97
$(S/V)/(S/V_{previous\ microdevice})$	4.45	4.21

Table 4.3.1 Chip A: CAD dimensions versus real values.

Chip B		
Features	**CAD**	**PDMS-replica mean value**
Surface (S) (mm^2)	561.73	565.97
Volume (V) (μL)	12.96	13.21
S/V (1/mm)	43.35	42.84
$(S/V)/(S/V_{previous\ microdevice})$	9.63	9.52

Table 4.3.2 Chip B: CAD dimensions versus real values.

4.3.2 Microdevices chemical analysis

XPS analyses were performed to investigate the chemical composition of the spiral-shape microdevices internal surfaces. In particular, this characterization was employed to verify the presence of chlorine on PDMS inner surfaces derived from the trichloromethylsilane compound. As reported before, during the fabrication process trichloromethylsilane was used to create an anti-adhesion layer necessary to easily detach the PDMS replica. Thus, before carrying out biological tests, it was fundamental to verify if this reagent could contaminate channels inner surfaces of the PMDS replica, since it was known that materials composing microdevices and residues of reagents employed in fabrication process could inhibit microdevice performances when specific amplification of nucleic acids was required, as in this case [189][190].

The chemical composition of PDMS slices cutted from different sites, located inside and outside the microchannel of each spiral-shape microdevice configuration was evaluated and compared to planar PDMS slices. As expected for PDMS, XPS survey spectra related to PDMS slices inside the microchannel and on bulk, confirmed the presence of oxygen, carbon and silicon, while no chlorine was detected (**Figure 4.3.4**). A similar composition for all the measured samples was reported through the quantification of elements described in **Table 4.3.3** as relative elemental percentage. In all the tested conditions similar amount of elements were present both on inner channel surfaces and on bulk microdevice material, as well as on PDMS planar surface and no chlorine was detected. Finally, the overall elemental composition highlighted by XPS measurements showed the molecular composition of PDMS [(C2H6OSi)n], with C/O and C/Si ratios around 1.7 and 2.5,

respectively, in agreement with previous PDMS-based microdevice results [170][191][192], confirming the PDMS characteristic biocompatibility.

Sample	O 1s (%)	C 1s (%)	Si 2p (%)
Channel A	29.4	51.7	18.6
Chip A bulk	29.7	51.5	18.5
Channel B	29.4	49.9	20.7
Chip B bulk	29.9	50.1	20.0
planar PDMS	28.8	50.7	20.5

Table 4.3.3 XPS relative quantification (%) of O, C and Si detected with a 0° take-off angle on inner (Channel A or B) and outer surfaces (Chip A bulk or Chip B bulk) of microdevices channels and on PDMS planar surfaces. Standard error does not exceed the 1-2% of the reported value.

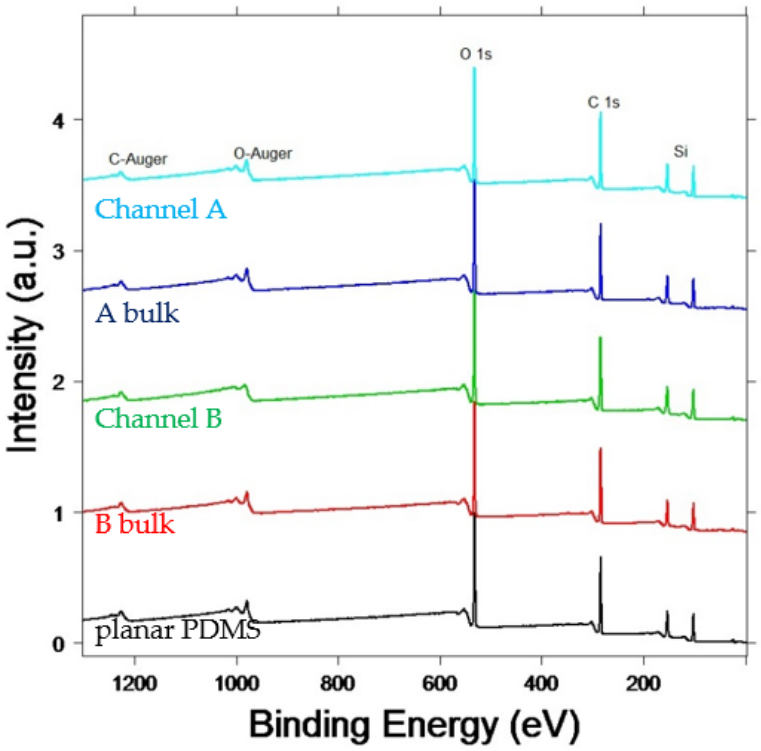

Figure 4.3.4 XPS survey spectra evaluated at 0° take-off angle. Spectra were taken inside microdevices channels (Channel A and Channel B), outside channels (A bulk and B bulk) and for comparison a planar PDMS surface was also considered (planar PDMS).

4.3.3 Silanization times analysis

Further experiments were carried out to adapt the manual protocol employed for the previous PDMS-based microdevice to the automated spiral-shape chip manipulation. As a first step, it was necessary to modify the silanization procedure to provide the best performances in terms of microRNAs adsorption.

The silanization mixture of 0.1% APTMS and 0.9% PEG-s silane (from now called AS) was injected in the central inlet of the microdevice at a flow rate of 2 µL/min and then, once full, the chip was immersed in water at 60°C for different times. In details, functionalizations on spiral-shape devices were studied at 0, 2, 5, 10, 20, 40 and 60 minutes. To perform this, 600 ng of fluorescent miR-1246-TAMRA diluted in water were infused and then adsorbed by the microchannels AS surfaces. **Figure 4.3.5(a)** reported the resulting value of fluorescence intensity, derived from the microscope image analysis, as a function of the silanization times. As depicted, a good microRNAs adsorption was observed both at 5 and 60 minutes concerning silanization times. In fact, after 5 and 60 minutes of silanization the fluorescence intensity of miR-1246-TAMRA resulted to be greater compared to the control experiment, i.e. when silanization occurred for 0 minute. Moreover, by evaluating the quantity of unbound microRNAs collected from every microdevices through a spectrophotometer analysis, it was possible to verify that the unbound material from microdevices silanized at 5 minutes was comparable with those silanized for 40 or even 60 minutes (**Figure 4.3.5(b)**). Finally, from these results, 5 minutes of silanization inside the water bath at 60 °C at the flow rate of 2 µL/min was chosen as the best compromise concerning the functionalization setting step for the automated protocol (**Figure 4.3.6**).

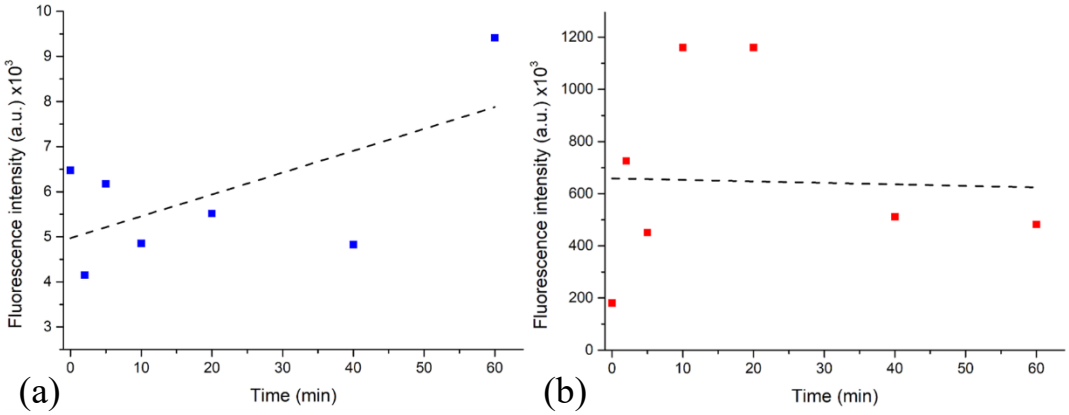

Figure 4.3.5 Optimization of silanization times: (a) fluorescence signal intensity of microRNAs absorbed in chips measured from optical microscopy images and (b) microRNAs solution recovered from chips after silanization experiment times.

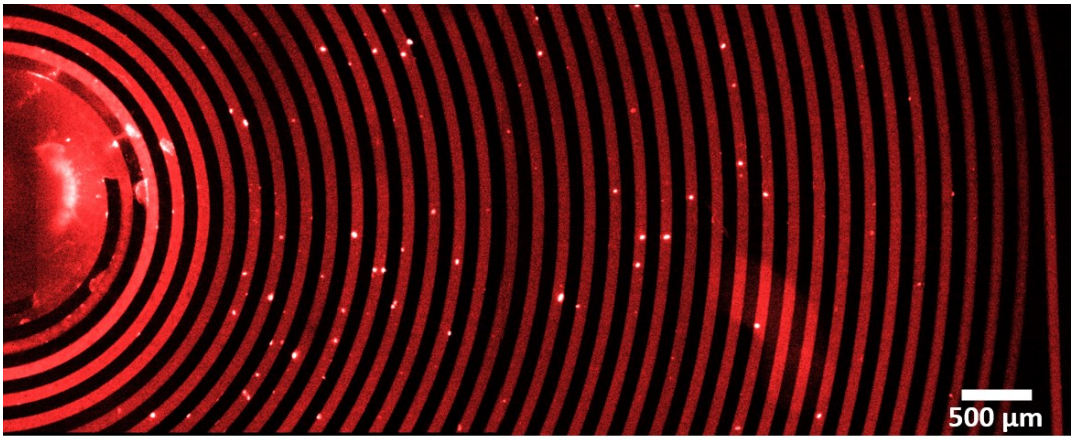

Figure 4.3.6 Fluorescence signal intensity of microRNAs absorbed in chips B after measured 5 minutes of silanization, using 2.5x objective lens with an exposure time of 3.01 s.

4.3.4 On-chip microRNA adsorption analysis

After having functionalized the chip, it was necessary to optimize the protocol for the microRNAs capture. Firstly, an investigation on the optimal flow rate value related to the microRNAs injection was carried out. During this step microRNAs infusion should be fast enough to allow the adsorption on the microchannels functionalized surfaces without damaging microRNAs molecules since it occurred at room temperature, but, at the same time, not too fast to avoid the effective contact of microRNAs with the positively charges surfaces. Then, the same quantity of miR-1246-TAMRA was injected either in Chip A and Chip B, after the silanization phase, and the microRNAs adsorption was evaluated for flow rates of 2 µL/min and 10 µL/min respectively. These two different flow rates were chosen to guarantee sufficient time to flux a quantity of 600 ng of microRNAs into microdevices. In details, 3 ng/ µL of miR-1246-TAMRA were injected at 2 µL/min for 100 minutes into the chip, while at a flow rate equal to 10 µL/min the same amount of microRNAs was infused for 20 minutes (**Figure 4.3.7**).

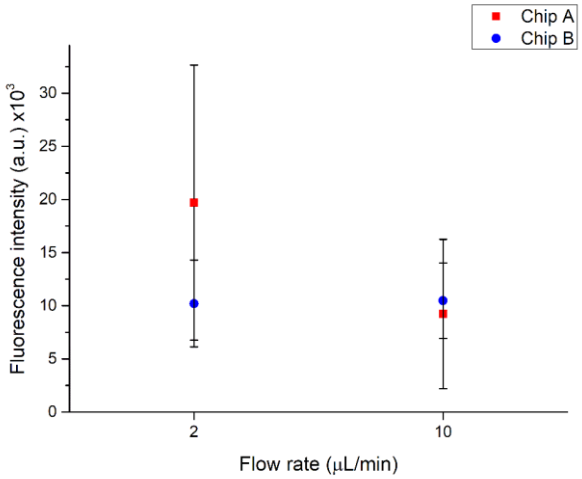

Figure 4.3.7 Flow rate optimization during microRNAs insertion in both spiral-shape configurations: 600 ng of miR-TAMRA were inserted at 2 µL/min for 100 minutes and 10 µL/min for 20 minutes.

Analyzing the fluorescence intensity of images acquired after the miRNAs capture, it was possible to notice how both flow rates gave similar results. Therefore, 10 µL/min was selected as the optimal flow rate value for what concerns microRNAs injection into the chip, thus allowing a reduction time of the assay.

Thereafter a washing step was crucial to remove the unbound microRNAs. Microdevices were rinsed with water, whose pH is slightly acidic, so surface charges did not preserve all the adsorbed microRNAs [193]. Thus, the volume of water used in the washing step should not exceed the minimum value that was necessary to effectively substitute the channel solution with water, otherwise the equilibrium of microRNA adsorbed on surfaces could be shifted toward its release. Therefore, after the microRNAs capture, two flow rates at 1 µL/min and 5 µL/min were considered to set during the washing step either at Chip A and Chip B. As depicted from fluorescence images in **Figure 4.3.8** a highlighted decrease of fluorescence intensities was observed during the washing step. Washing started from the central inlet hole and proceeded through the coils up to ending straight channel.

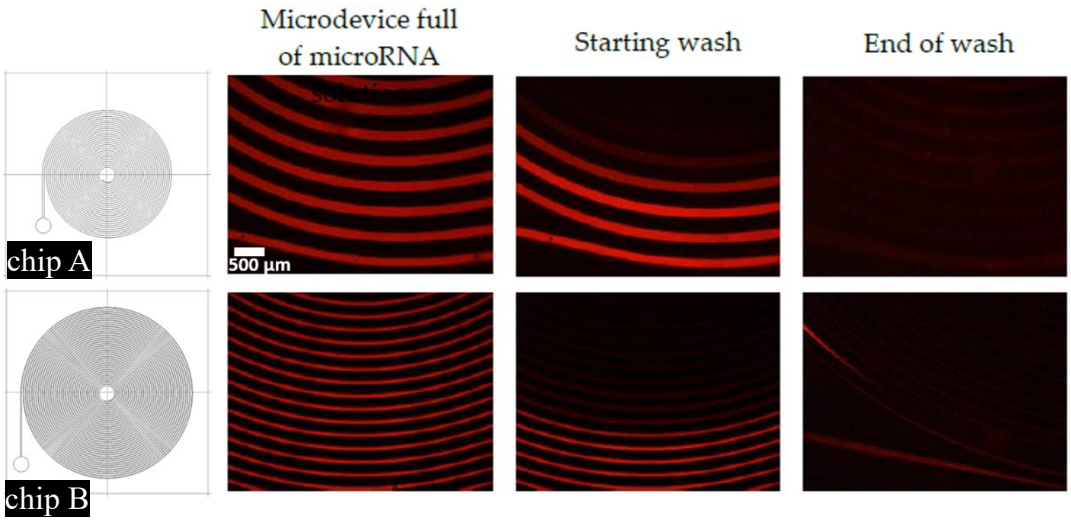

Figure 4.3.8 Fluorescence images of microRNAs washed into microdevices with 2.5x objective magnification lens.

Thus, to have a quantification of the fluorescence intensity decrease, fluorescence images were acquired at defined times during the washing step. As reported in **Figure 4.3.9**, fluorescence intensity of images were reported as a function of relative volumes, each one referred to a defined spiral shape configuration. In details, both flow rates provided similar results either in Chip A and Chip B. The excess of unbound microRNAs reached a plateau after fluxing a volume of water equal to a microdevice volume. Finally, to define a common protocol for both spiral-shape microdevices, a washing step at 1 µL/min for 10 minutes was selected as the most adequate to remove the unbound materials and preserve the adsorbed microRNAs on microchannels AS surfaces. Infusing water

for 10 minutes corresponded to about one washing volume and it was considered compatible with the overall duration of the assay.

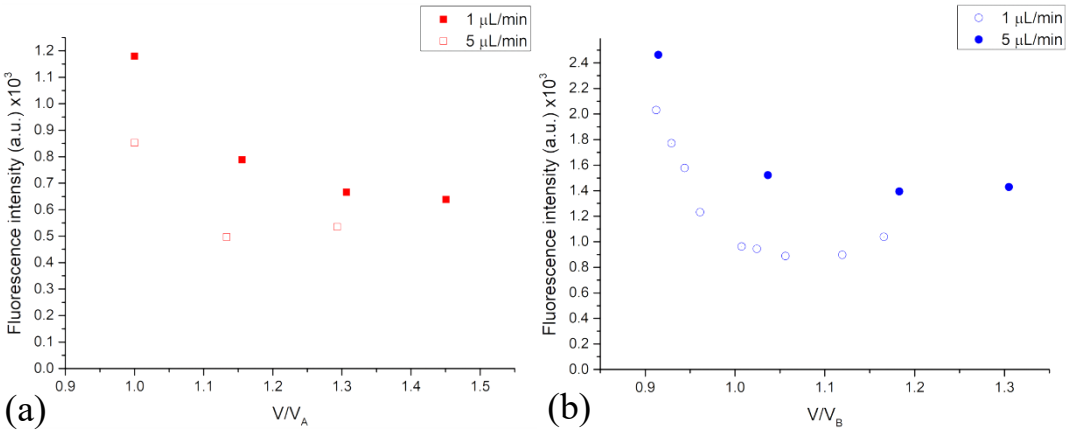

Figure 4.3.9 Optimization of washes speed after miR adsorption. A washing step with water was performed at 1 µL/min and 5 µL/min both for Chip A (a) and Chip B (b). Relative volumes were reported referred to each spiral configuration volume.

4.3.5 Confocal microscopy microRNA adsorption analysis

Until now all the parameters for the automatized protocol for both spiral-shape microdevices were set up by measuring the fluorescence signal related to the presence of miR-1246-TAMRA with a wide-field fluorescence microscope. This approach appropriated for a relative comparison when different conditions were applied to the microdevices, at the same time it appeared inadequate when a strict quantification was needed. In fact, the collected fluorescence signal was mostly related to the microRNA adsorbed on channels top and bottom surfaces, with a minor contribution from channels lateral surfaces. Therefore, a confocal microscope characterization was exploited to evaluate the uniformity of microRNAs adsorption on lateral microchannel surfaces. By working in the z-stacking mode of the microscope, it was possible to acquire three-dimensional images of microchannels from the two kinds of spiral-shape devices. To do this, after the washing step, following the microRNAs adsorption, microdevices were dried with a nitrogen flux and then were cut diagonally with an angle of about 30° with respect to the normal pattern surfaces to favor the imaging through the confocal microscope.

For these experiments for Chip A was injected an amount of 1200 ng of miR-1246-TAMRA diluted in water and adsorbed on the silanized surfaces, while Chip B was analyzed with an amount of 600 ng of miR-1246-TAMRA adsorbed onto the functionalized walls. As illustrated from three-dimensional images, all internal microchannels surfaces are sketched in **Figure 4.3.10** either in Chip A and Chip B. Indeed, the presence of fluorescent microRNAs resulted homogenously distributed on all the visible surfaces, allowing to consider both microdevices properly functionalized and then suitable for microRNAs adsorption.

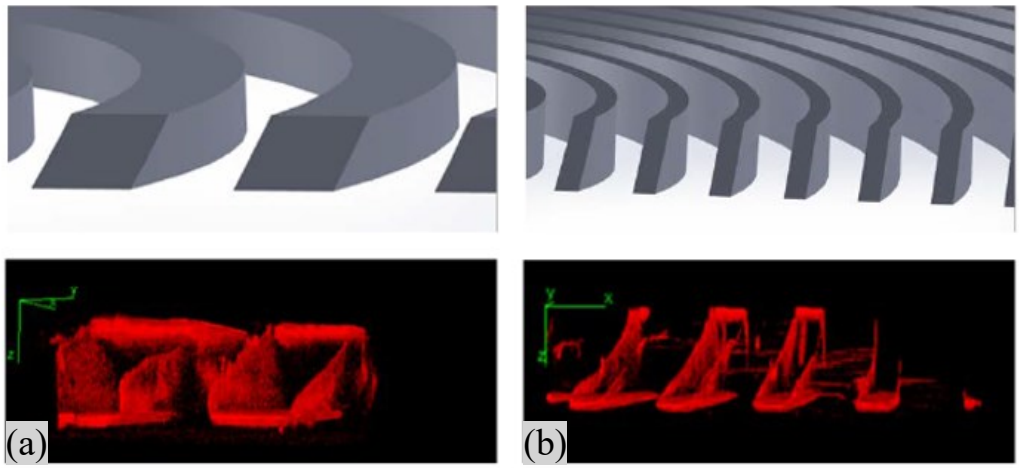

Figure 4.3.10 Check for surface availability for microRNA adsorption in chip A (a) and chip B (b) through the convolution of the images performed during the z-stacking mode using the 20x objective lens of the confocal microscopy. 3D CAD designs are presented for each spiral-shape microdevice on the top of the image.

4.3.6 Total channel surfaces analysis

Further tests were performed to study the maximum microRNAs loading capacity of the two spiral-shape device configurations. To do this, all parameters such as flow rate, microRNAs insertion time, flux and washing time were kept constant while microRNAs concentration spiked in water was variable. Thus, a titration based on different amount of miR-1246-TAMRA was carried out injecting 50, 150, 300 and 600 ng of microRNAs into microdevices (**Figure 4.3.11**).

Figure 4.3.12 revealed an estimation of the total area covered by fluorescent microRNAs versus the amount of microRNAs infused into Chip A and Chip B. These results confirmed how Chip B, characterized by a more extended channel surface, could adsorb a higher amount of microRNAs compared to Chip A. From design values the total surface area of Chip A corresponded to 261.54 mm^2, while for Chip B it resulted to be 561.73 mm^2. Thus, the insertion of 300 ng of miR-1246-TAMRA saturated the ability of microRNAs capture for Chip A, while a double amount of microRNAs could be still absorbed by Chip B, reflecting the different S/V values for the two spiral-shape devices. In fact, the S/V value of chip B, equal to 9.63 mm^{-1}, was about double the S/V value of Chip A (4.45 mm^{-1}).

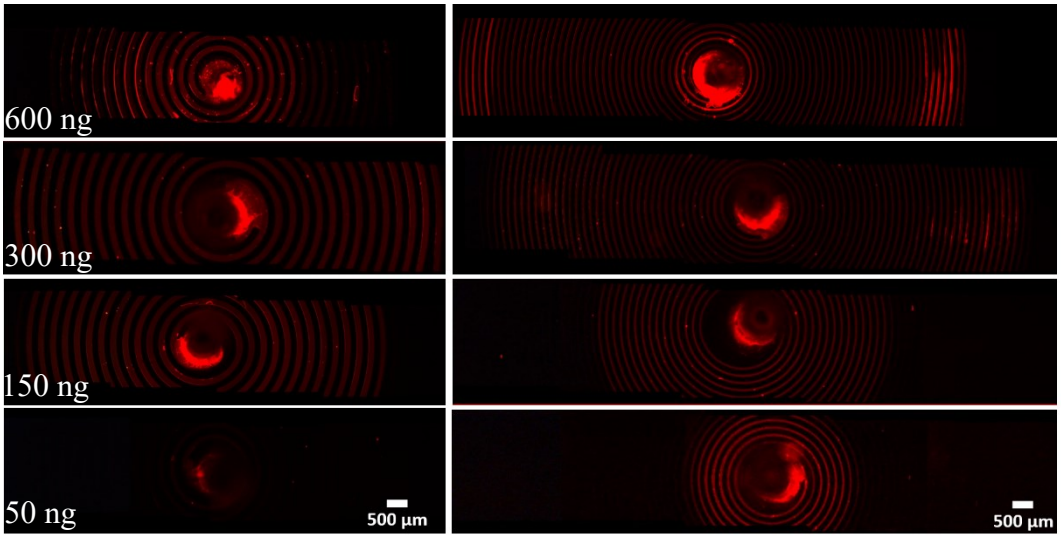

Figure 4.3.11 Miscroscope fluorescence images of Chip A (on the left) and Chip B (on the right) when 50, 150, 300 and 600 ng of miR-1246-TAMRA adsorbed. Images performed with 2.5x objective lens with exposure time of 3.1 s.

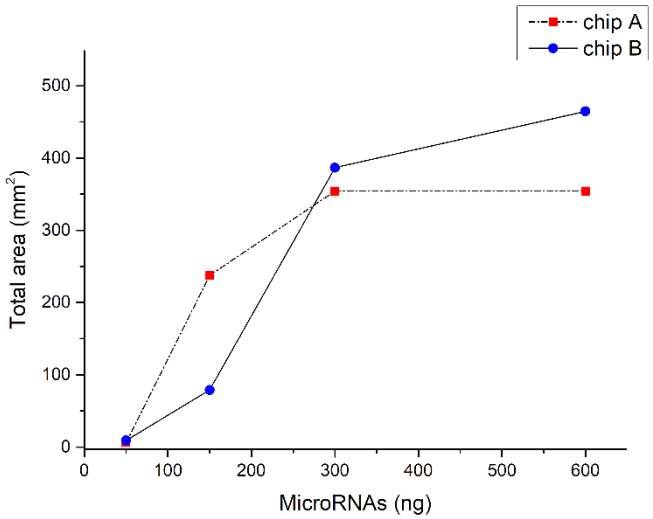

Figure 4.3.12 Testing microdevices performances in microRNAs adsorption. Both chips adsorbed different quantities of miR-1246-TAMRA spiked in water.

4.3.7 MicroRNAs spiked in human plasma analysis

As reported in the previous paragraph, since Chip B showed better performance than Chip A, that microdevice configuration was selected for microRNAs spike in human plasma analyses. In detail, chip B was characterized by introducing a constant concentration of microRNAs spiked in human plasma added with lysis buffer at different times (**Figure 4.3.13**). Lysis buffer was added into the human plasma in order to favor the release of microRNAs from vesicles encapsulation or protein complexes, in the perspective of the application of microdevices with clinically relevant samples.

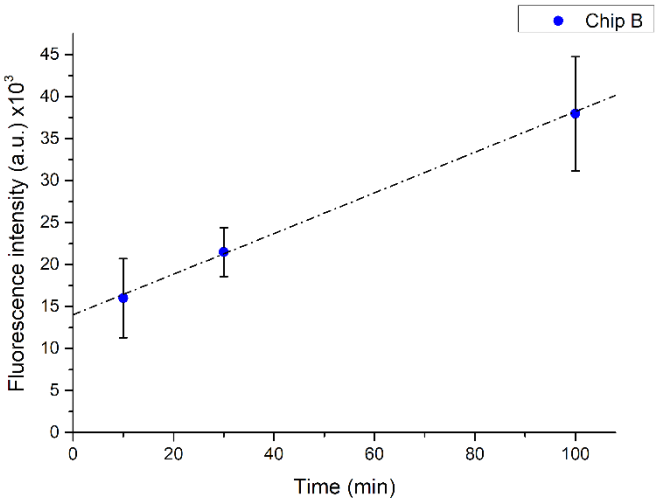

Figure 4.3.13 Adsorption of miR-1246-TAMRA spiked in human plasma added with lysis buffer at constant concentration on Chip B at different times. Fluorescence signal mean values were measured in consecutive coils, while error bars refer to standard error. Dotted line represented a linear fit with equation $y = 241.969x + 14024.942$ and R^2 =0.999).

As expected, it was found a linear increment of the microRNAs fluorescence signal intensity, derived from chips injected at different times. This trend demonstrated the capability of microchannel surfaces to capture the microRNA even when it was dissolved in a complex matrix such as human plasma. Moreover, from the same data, this behavior was constant in time, leading to a linear increase of captured miRNAs. In addition, even if blood plasma contains a lot of components such as proteins, lipids, small molecules, etc., that could be adsorbed to the positively-charged surfaces as well as nucleic acids, however, they did not impede the further adsorption of microRNAs on the surface sites still available. This PDMS-based microdevice characteristic was already demonstrated with the previous PDMS microdevice with a limited surface available for microRNAs capture [177][191].

4.3.8 Validation of PDMS microdevices through RT-PCR analysis

Finally, preliminary test on PDMS microdevices were accomplished through a chain reaction amplification step since the aim of this device was the specific capture of low amounts of microRNAs as biomarkers of oncological pathologies in the context of liquid biopsy. Then, to validate chips for their final application, microRNA-20a, microRNA-222 and microRNA-320 were chosen as a minimal panel of NSCLC biomarkers [194][195].

MicroRNAs, at different ranges of concentration, were spiked in water or in human plasma with lysis buffer and captured by the functionalized microdevice surfaces. Then, after the washing step, necessary to remove the unbound material on the channel walls, the proper reverse transcription mix was injected into the microdevice from the central inlet of each spiral-shape configuration and the

adsorbed miRNAs were directly reverse-transcribed on-chip on a thermal cycler equipped with a flat thermal block, as already performed for the previous PDMS microdevice[177]. Thereafter, the solution containing cDNA molecules was extracted from the external outlet and collected to feed the DNA amplification step via the RT-qPCR reaction using standard tubes and equipment.

Figure 4.3.14 reports the results related to the RT-qPCR assays for miRNAs quantifications: an inverse proportionality between threshold cycles (Ct) and the amounts of spiked microRNAs was observed. The Ct is defined as the number of cycles required for the fluorescent signal to cross the threshold line, that indicates the fluorescence background level. The Ct is a relative measure of the concentration of target in the PCR reaction and its value increases with a decreasing amount of specimen. Analyses performed on the same amount of microRNAs spiked in water or in plasma, revealed a dependence on Ct values with respect to the medium, indeed better Ct values was detected in plasma. This discrepancy could be explained through the passivation effect derived from proteins present in plasma and absent when microRNAs was spiked in water. So, the components of a biological sample not only did not adversely compete with microRNA molecules for the adsorption sites, but allow their greater reaction with channel surfaces. A possible explanation could be that on silanized microchannel surfaces were available the same quantities of functionalized sites, but since in water more sites were free, they could have captured constrained conformation microRNA molecules, thus yielding a lower amount of cDNA molecules to be amplified in the reverse transcription step. In addition, non-passivated chip surfaces could also have adsorbed components of the reverse transcription mix as well as the just-copied cDNA RT-qPCR.

As depicted in **Figure 4.3.14** microdevices were able to capture different amounts of synthetic microRNAs spiked either in water and in human plasma directly reverse-transcribed on chip and amplified in standard conditions.

MicroRNA-20a, microRNA-222 and microRNA-320, the panel of biomarkers associated with NSCLC, were detected at different concentrations equal to 0.1, 1, 10, 100, 1000 pg of microRNAs proving that no preferences were observed for different microRNA molecules. Results from all three microRNA molecules were evaluated as similar and so they were fitted together, as reported in the dotted lines in **Figure 4.3.14**. The resulting fit is a straight line in semi-log graphs both for microRNAs spiked in water and in plasma confirming the correlation between microRNA incubated and adsorbed on microchannel surfaces. Finally, microdevices performances were further tested by detecting microRNAs naturally present in human plasma collected from a healthy donor, even if at lower concentrations. The same protocol as before was applied for the adsorption of miR-20a and miR-222 on Chip A, obtaining a Ct of 31 ± 2 and of 32 ± 4, respectively. These data were compared with those obtained by using a PDMS microdevice already validated for capturing circulating microRNAs [177][191]. In this case, the previous PDMS microdevice acted in this context as positive control. The Ct resulting from the capture of miR-20a and miR-222 from the same human plasma sample were 32 ± 0.1 and 34 ± 0.1, respectively. Therefore, the results of the spiral-shaped microdevice were in-line with the positive control. As a conclusion, the

spiral-shaped microdevice was demonstrated as a good candidate for the easy detection of microRNAs biomarkers from biological samples, even if a further optimization, especially in terms of fluids manipulation is still necessary.

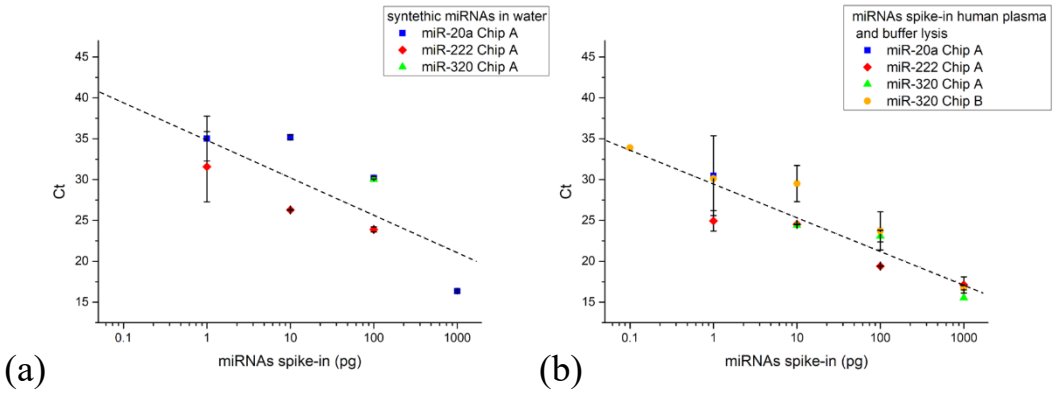

Figure 4.3.14 RT-qPCR results expressed as threshold cycles (Ct) measured when different amounts of synthetic microRNA were spiked in water (a) or in blood plasma (b). A dotted line, from a logarithmic fit of all data is shown.

4.4 Conclusion

This chapter presented PDMS-based microdevices focused on the specific capture of low amounts of microRNAs as biomarkers of oncological pathologies in the context of liquid biopsy. This procedure is easily accessible, not invasive and, therefore useful for mass screening and for biomarkers profiling of patients during specific therapies such as diagnostic purposes or following the progress of a disease. Thus, microdevices to be evaluated as diagnostic tools in liquid biopsy must be able to concentrate and detect microRNAs molecules found in little amounts in biological fluids. To do this, based on the performance of a previous PDMS-based microdevice reported in literature [177][191], novel spiral-shape chips with a higher S/V were presented.

Two spiral-shape microdevices possessing different surface to volume ratios, thus offering different internal surfaces available for the microRNA molecules capture, were deeply investigated from the fabrication process to chips functional applications. Firstly, spiral-shape microdevices reported in this chapter were characterized both through a morphological and chemical analysis to verify the compatibility for biological applications. Then, the manual protocol used for the previous PDMS-based microdevice [177][191] was adopted to the automated microdevice manipulation. Thus, all on-chip protocol steps such as surfaces silanization, microRNAs capture and washing step were examined in depth employing synthetic microRNAs spiked both in water and human plasma. Finally, validation of spiral-shape microdevices was performed via PCR reaction tests.

Results demonstrated that spiral-shape chips offered a higher S/V able to capture a higher amount of microRNAs with respect to the previous PDMS-based device. Finally, since spiral-shape microdevices were able to purify a group of microRNAs as cancer biomarkers from biological fluids such as human plasma, this suggested the possibility to use them in a future for the earlier diagnosis of pathologies.

Chapter 5

Conclusions and future perspectives

Results presented in this PhD Thesis work display the development of three microfluidic devices for the analysis of various biomarkers (i.e. cells, exosomes and miRNAs), exploiting different fabrication methods, with the aim to achieve lab on a chips for the early detection and diagnosis of lung cancer. The development of these tools in liquid biopsy can improve our understanding of lung cancer pathophysiology and its molecular origins. Thus, the actual challenge is to introduce new microfluidic platforms, owing high integration, throughput and efficiency with reduced time and cost in clinical practice.

Considering some of the common issue reported in literature, this PhD Thesis presents the development and the analysis of each microfluidic device, first by introducing the relevant design and fabrication method related to its functionality and then by inspecting device features dimensions and evaluating its performances either with synthetic and biological samples employing different approaches.

In Chapter 2 a novel free-flow zone electrophoresis microfluidic device based on an active method for the manipulation of biomarkers is analysed. Morphological characterizations of device features dimensions highlighted how an accurate reproducibility of the design was performed employing an additive manufacturing method. The introduction of 3D printing technology to microfluidics enables fast and rapid device prototyping exploiting low-cost materials. Moreover, this fabrication method allows an easy introduction of further design updates in limited re-work time, as depicted in this chapter, where inlet and outlet ports with proper tube connection were easily integrated by modifying a preliminary design. Furthermore, characterization of analytes, different in surface-to-charge ratios (i.e. particles and exosomes), collected at the outlets demonstrated the device performance to tune the motion of analytes in a specific outlet when a defined voltage value at the electrodes was imposed and also to accumulate them in a microliter volume range.

In Chapter 3, performance analyses of a silicon-based microfluidic device employed to separate biomarkers possessing micrometric dimensions are investigated. In this case, the active mechanism of controlling biomarkers motion exploited acoustic forces, rather than applying an electric field, as mentioned above. Prior to analyse bulk acoustic wave device focalization performances, design and fabrication method were reported and investigated, as well as protocol steps involved in the development of a customized set-up to allow the formation of an acoustic standing wave field into the microfluidic channel. Afterwards, device focalization potentiality is evaluated analysing samples, composed either by polystyrene micro- and nanoparticles and cells as single or mixed populations, collected at the outlets of the device when different setting condition (i.e. sample concentration, applied voltage value at the piezoelectric element and flow rate) were applied. Regarding micro particles results, higher device focalization

performances are demonstrated when lower concentration, lower flow rate and higher applied voltage value to the transducer was applied. Furthermore, a confirmation of these data resulted from a comparison between experimental data and simulated analysis. Finally, data obtained from HL-60 cells demonstrated the capability to collect cells either at high flow rate and when they were mixed with a population of micro and nanoparticles without affecting device focalization performances.

In Chapter 4 a third type of microfluidic device developed during this thesis work is inspected. In detail, two PDMS-based microfluidic devices, characterized by different surface-to-volume ratios were designed to capture low amount of microRNA molecules from biological fluids. Morphological results performed on both microfluidic devices demonstrated increased availability of internal channel surfaces for the capture of biomarkers with respect to a previous developed PDMS-microfluidic device, while chemical results displayed the compatibility for biological applications regarding materials exploited during the fabrication process. Furthermore, from the analysis on parameters involved during steps performed for the microRNAs capture of devices, a customized and fully automatized process was defined. Finally, a validation of both PDMS-microfluidic devices was performed via PCR reaction tests, employing synthetic microRNAs and a pool of microRNA molecules associated to NSCLC spiked either in water and human plasma.

To conclude, microfluidic devices results performed with biological samples presented in this PhD Thesis constitutes a proof of concept for the development of new diagnostic tools for the early detection, prognosis and treatments of lung cancer disease. Indeed, these microfluidic devices represent a starting point for the analysis of various biomarkers useful in routine diagnostic and clinical practice. Combining advantages of each developed microfluidic device as well as advantages of each fabrication method, new microfluidic platforms can be manufactured, overcoming critical issues related to the use of conventional methods. Thus, the development of rapid integrated and multi-analysis systems will be useful to enhance the standardization and the performance of the analytical procedures involved in liquid biopsy.

Chapter 6

References

[1] "GLOBOCAN," 2018. [Online]. Available: http://gco.iarc.fr/.

[2] R. S. Herbst, J. V. Heymach, and S. M. Lippman, "Molecular origin of cancer Lung cancer," *N. Engl. J. Med.*, no. September, pp. 1367–1380, 2008.

[3] M. B. Schabath and M. L. Cote, "Cancer progress and priorities: Lung cancer," *Cancer Epidemiol. Biomarkers Prev.*, vol. 28, no. 10, pp. 1563–1579, 2020.

[4] C. S. Dela Cruz, L. T. Tanoue, and R. A. Matthay, "Lung Cancer: Epidemiology, Etiology and Prevention," *Clin Chest Med*, vol. 32, no. 4, 2011.

[5] A. M. Romaszko and A. Doboszynska, "Multiple primary lung cancer: A literature review," *Adv. Clin. Exp. Med.*, vol. 27, no. 5, pp. 717–722, 2018.

[6] F. Nasim, B. F. Sabath, and G. A. Eapen, "Lung Cancer," *Med. Clin. North Am.*, vol. 103, no. 3, pp. 463–473, 2019.

[7] J. Malhotra, M. Malvezzi, E. Negri, C. La Vecchia, and P. Boffetta, "Risk factors for lung cancer worldwide," *Eur. Respir. J.*, vol. 48, no. 3, pp. 889–902, 2016.

[8] Y. Mao, D. Yang, J. He, and M. J. Krasna, "Epidemiology of Lung Cancer," *Surg. Oncol. Clin. N. Am.*, vol. 25, no. 3, pp. 439–445, 2016.

[9] L. A. Torre, R. L. Siegel, and A. Jemal, "Lung cancer statistics," *Adv. Exp. Med. Biol.*, vol. 893, pp. 1–19, 2016.

[10] A. G. Pallis and K. N. Syrigos, "Lung cancer in never smokers: Disease characteristics and risk factors," *Crit. Rev. Oncol. Hematol.*, vol. 88, no. 3, pp. 494–503, 2013.

[11] G. A. Rivera and H. Wakelee, "Lung cancer in never smokers," *Adv. Exp. Med. Biol.*, vol. 893, pp. 43–57, 2016.

[12] G. Poulet, J. Massias, and V. Taly, "Liquid Biopsy: General Concepts," *Acta Cytol.*, vol. 63, no. 6, pp. 449–455, 2019.

[13] S. Mader and K. Pantel, "Liquid biopsy: Current status and future perspectives," *Oncol. Res. Treat.*, vol. 40, no. 7–8, pp. 404–408, 2017.

[14] P. Pisapia, U. Malapelle, and G. Troncone, "Liquid Biopsy and Lung Cancer," *Acta Cytol.*, vol. 63, no. 6, pp. 489–496, 2019.

[15] C. Rolfo *et al.*, "Liquid Biopsy for Advanced Non-Small Cell Lung Cancer (NSCLC): A Statement Paper from the IASLC," *J. Thorac. Oncol.*, vol. 13,

no. 9, pp. 1248–1268, 2018.
[16] K. Pantel and C. Alix-Panabières, “Liquid biopsy and minimal residual disease — latest advances and implications for cure,” *Nat. Rev. Clin. Oncol.*, vol. 16, no. 7, pp. 409–424, 2019.
[17] P. Hofman, “Liquid biopsy and therapeutic targets: Present and future issues in thoracic oncology,” *Cancers (Basel).*, vol. 9, no. 11, pp. 1–13, 2017.
[18] M. Chen and H. Zhao, “Next-generation sequencing in liquid biopsy: cancer screening and early detection,” *Hum. Genomics*, vol. 13, no. 1, p. 34, 2019.
[19] R. Vaidyanathan, R. H. Soon, P. Zhang, K. Jiang, and C. T. Lim, “Cancer diagnosis: from tumor to liquid biopsy and beyond,” *Lab Chip*, vol. 19, no. 1, pp. 11–34, 2019.
[20] N. Guibert, A. Pradines, J. Mazieres, and G. Favre, “Current and future applications of liquid biopsy in nonsmall cell lung cancer from early to advanced stages,” *Eur. Respir. Rev.*, vol. 29, no. 155, 2020.
[21] K. Strimbu and J. A. Tavel, “What are Biomarkers?,” *Curr Opin HIV AIDS*, vol. 5, no. 6, pp. 463–466, 2010.
[22] R. M. Califf, “Biomarker definitions and their applications,” *Exp. Biol. Med.*, vol. 243, no. 3, pp. 213–221, 2018.
[23] A. J. Vargas and C. C. Harris, “Biomarker development in the precision medicine era: lung cancer as a case study,” vol. 16, no. 8, pp. 525–537, 2019.
[24] Y. Li *et al.*, “Clinical significance of circulating tumor cells and tumor markers in the diagnosis of lung cancer,” *Cancer Med.*, vol. 8, no. 8, pp. 3782–3792, 2019.
[25] L. Wu and X. Qu, “Cancer biomarker detection: Recent achievements and challenges,” *Chem. Soc. Rev.*, vol. 44, no. 10, pp. 2963–2997, 2015.
[26] P. Villalobos and I. I. Wistuba, “Lung Cancer Biomarkers,” *Hematol. Oncol. Clin. North Am.*, vol. 31, no. 1, pp. 13–29, 2017.
[27] V. A. Hristova and D. W. Chan, “Cancer biomarker discovery and translation: proteomics and beyond,” *Expert Rev. Proteomics*, vol. 16, no. 2, pp. 93–103, 2019.
[28] L. M. Seijo *et al.*, “Biomarkers in Lung Cancer Screening: Achievements, Promises, and Challenges,” *J. Thorac. Oncol.*, vol. 14, no. 3, pp. 343–357, 2019.
[29] N. A. Pennell, M. E. Arcila, D. R. Gandara, and H. West, “Biomarker Testing for Patients With Advanced Non–Small Cell Lung Cancer: Real-World Issues and Tough Choices,” *Am. Soc. Clin. Oncol. Educ. B.*, no. 39, pp. 531–542, 2019.
[30] C. Paoletti and D. F. Hayes, “Circulating tumor cells,” in *Novel Biomarkers in the Continuum of Breast Cancer*, 2nd ed., V. Stearns, Ed. 2016, pp. 235–258.
[31] S. A. Garcia, J. Weitz, and S. Scholch, “Circulating tumor cells,” *Cancer Stem Cells*, vol. 1692, pp. 213–219, 2018.
[32] H. Skovierova, E. Vidomanova, M. Skoviera, B. Tothova, E. Halasova, and J. Strnadel, “Circulating tumor cells in lung carcinogenesis,” *Neoplasma*, vol. 66, no. 1, pp. 1–7, 2019.
[33] K. Pantel and M. R. Speicher, “The biology of circulating tumor cells,” *Oncogene*, vol. 35, no. 10, pp. 1216–1224, 2016.
[34] L. Cabel *et al.*, “Circulating tumor cells: clinical validity and utility,” *Int. J. Clin. Oncol.*, vol. 22, no. 3, pp. 421–430, 2017.
[35] M. Yousefi *et al.*, “Prognostic and therapeutic significance of circulating tumor cells in patients with lung cancer,” *Cell. Oncol.*, vol. 43, no. 1, pp. 31–

49, 2020.
[36] N. Yu, J. Zhou, F. Cui, and X. Tang, “Circulating Tumor Cells in Lung Cancer: Detection Methods and Clinical Applications,” *Lung*, vol. 193, no. 2, pp. 157–171, 2015.
[37] B. Tong and M. Wang, “Circulating tumor cells in patients with lung cancer: Developments and applications for precision medicine,” *Futur. Oncol.*, vol. 15, no. 21, pp. 2531–2542, 2019.
[38] A. Tartarone *et al.*, “Possible applications of circulating tumor cells in patients with non small cell lung cancer,” *Lung Cancer*, vol. 107, pp. 59–64, 2017.
[39] N. Normanno, A. De Luca, M. Gallo, N. Chicchinelli, and A. Rossi, “The prognostic role of circulating tumor cells in lung cancer,” *Expert Rev. Anticancer Ther.*, vol. 16, no. 8, pp. 859–867, 2016.
[40] V. Maly, O. Maly, K. Kolostova, and V. Bobek, “Circulating tumor cells in diagnosis and treatment of lung cancer,” *In Vivo (Brooklyn).*, vol. 33, no. 4, pp. 1027–1037, 2019.
[41] S. Cui, Z. Cheng, W. Qin, and L. Jiang, “Exosomes as a liquid biopsy for lung cancer,” *Lung Cancer*, vol. 116, no. 25, pp. 46–54, 2018.
[42] S. Villata, M. Canta, and V. Cauda, “Evs and bioengineering: From cellular products to engineered nanomachines,” *Int. J. Mol. Sci.*, vol. 21, no. 17, pp. 1–32, 2020.
[43] L. Zhou *et al.*, “The biology, function and clinical implications of exosomes in lung cancer,” *Cancer Lett.*, vol. 407, pp. 84–92, 2017.
[44] R. M. Johnstone, M. Adam, J. R. Hammonds, and C. Turbide, “Vesicle Formation during Reticulocyte Maturation,” *J. Biol. Chem.*, vol. 262, no. 1, pp. 9412–9420, 1987.
[45] M. P. Zaborowski, L. Balaj, X. O. Breakefield, and C. P. Lai, “Extracellular Vesicles: Composition, Biological Relevance, and Methods of Study,” *Bioscience*, vol. 65, no. 8, pp. 783–797, 2015.
[46] G. Raposo and W. Stoorvogel, “Extracellular vesicles: Exosomes, microvesicles, and friends,” *J. Cell Biol.*, vol. 200, no. 4, pp. 373–383, 2013.
[47] G. Van Niel, G. D’Angelo, and G. Raposo, “Shedding light on the cell biology of extracellular vesicles,” *Nat. Rev. Mol. Cell Biol.*, vol. 19, no. 4, pp. 213–228, 2018.
[48] M. Kanada, M. H. Bachmann, and C. H. Contag, “Signaling by Extracellular Vesicles Advances Cancer Hallmarks,” *Trends in Cancer*, vol. 2, no. 2, pp. 84–94, 2016.
[49] J. Kowal, M. Tkach, and C. Théry, “Biogenesis and secretion of exosomes,” *Curr. Opin. Cell Biol.*, vol. 29, no. 1, pp. 116–125, 2014.
[50] C. Théry *et al.*, “Minimal information for studies of extracellular vesicles 2018 (MISEV2018): a position statement of the International Society for Extracellular Vesicles and update of the MISEV2014 guidelines,” *J. Extracell. Vesicles*, vol. 7, no. 1, 2018.
[51] S. Gurunathan, M.-H. Kang, M. Jeyaraj, M. Qasim, and J.-H. Kim, “Review of the Isolation, Characterization, Biological Function, and Multifarious Therapeutic Approaches of Exosomes,” *Cells*, vol. 8, no. 4, p. 307, 2019.
[52] K. C. S. Roballo *et al.*, “Neurons-derived extracellular vesicles promote neural differentiation of ADSCs: a model to prevent peripheral nerve degeneration,” *Sci. Rep.*, vol. 9, no. 1, p. 11213, 2019.
[53] I. J. McGough and J. P. Vincent, “Exosomes in developmental signalling,” *Dev.*, vol. 143, no. 14, pp. 2482–2493, 2016.

[54] D. Marimpietri *et al.*, "Proteome Profiling of Neuroblastoma-Derived Exosomes Reveal the Expression of Proteins Potentially Involved in Tumor Progression," *PLoS One*, vol. 8, no. 9, 2013.
[55] S. Mishra, T. Yadav, and V. Rani, "Exploring miRNA based approaches in cancer diagnostics and therapeutics," *Crit. Rev. Oncol. Hematol.*, vol. 98, pp. 12–23, 2016.
[56] T. X. Lu and M. E. Rothenberg, "MicroRNA," *J Allergy Clin Immunol*, vol. 141, no. 4, pp. 1202–1207, 2018.
[57] W. Wang *et al.*, "Identification of miRNAs as non-invasive biomarkers for early diagnosis of lung cancers," *Tumor Biol.*, vol. 37, no. 12, pp. 16287–16293, 2016.
[58] M. A. Iqbal, S. Arora, G. Prakasam, G. A. Calin, and M. A. Syed, "MicroRNA in lung cancer: role, mechanisms, pathways and therapeutic relevance," *Mol. Aspects Med.*, vol. 70, no. June, pp. 3–20, 2019.
[59] J. Li, H. Fang, F. Jiang, and Y. Ning, "External validation of a panel of plasma microRNA biomarkers for lung cancer," *Biomark. Med.*, vol. 13, no. 18, pp. 1557–1564, 2019.
[60] L. Chen, L. Heikkinen, C. Wang, Y. Yang, H. Sun, and G. Wong, "Trends in the development of miRNA bioinformatics tools," *Brief. Bioinform.*, vol. 20, no. 5, pp. 1836–1852, 2019.
[61] E. A. Lekchnov, I. A. Zaporozhchenko, E. S. Morozkin, O. E. Bryzgunova, V. V. Vlassov, and P. P. Laktionov, "Protocol for miRNA isolation from biofluids," *Anal. Biochem.*, vol. 499, pp. 78–84, 2016.
[62] J. D. Cohen *et al.*, "Detection and localization of surgically resectable cancers with a multi-analyte blood test," *Science (80-.).*, vol. 359, no. 6378, pp. 926–930, 2018.
[63] M. Wang, F. Yu, H. Ding, Y. Wang, P. Li, and K. Wang, "Emerging Function and Clinical Values of Exosomal MicroRNAs in Cancer," *Mol. Ther. - Nucleic Acids*, vol. 16, no. June, pp. 791–804, 2019.
[64] C. M. Pandey *et al.*, "Microfluidics Based Point-of-Care Diagnostics," *Biotechnol. J.*, vol. 13, pp. 1700047–1700058, 2017.
[65] P. Sajeesh and A. K. Sen, "Particle separation and sorting in microfluidic devices: A review," *Microfluid. Nanofluidics*, vol. 17, no. 1, pp. 1–52, 2014.
[66] H. S. Santana *et al.*, "Microfluidic Devices and 3D Printing for Synthesis and Screening of Drugs and Tissue Engineering," *Ind. Eng. Chem. Res.*, vol. 59, no. 9, pp. 3794–3810, 2020.
[67] M. Sonker, V. Sahore, and A. T. Woolley, "Recent advances in microfluidic sample preparation and separation techniques for molecular biomarker analysis: A critical review," *Anal. Chim. Acta*, vol. 986, pp. 1–11, 2017.
[68] M. Safdar, J. Jänis, and S. Sánchez, "Microfluidic fuel cells for energy generation," *Lab Chip*, vol. 16, no. 15, pp. 2754–2758, 2016.
[69] N. Pamme, "Continuous flow separations in microfluidic devices," *Lab Chip*, vol. 7, no. 12, pp. 1644–1659, 2007.
[70] H. Jayamohan, H. J. Sant, and B. K. Gale, "Applications of micro fluidics for molecular diagnostics," *Methods Mol. Biol.*, vol. 949, pp. 305–334, 2013.
[71] B. Yilmaz and F. Yilmaz, "Lab-on-a-Chip technology and its applications," *Omi. Technol. Bio-engineering Towar. Improv. Qual. Life*, vol. 1, pp. 145–153, 2018.
[72] A. Francesko, V. F. Cardoso, and S. Lanceros-Méndez, *Lab-on-a-chip technology and microfluidics*. 2018.
[73] D. J. Beebe, G. A. Mensing, and G. M. Walker, "Physics and applications of

microfluidics in biology," *Annu. Rev. Biomed. Eng.*, vol. 4, pp. 261–286, 2002.
[74] K. Ren, J. Zhou, and H. Wu, "Materials for microfluidic chip fabrication," *Acc. Chem. Res.*, vol. 46, no. 11, pp. 2396–2406, 2013.
[75] P. Kim, K. W. Kwon, M. C. Park, S. H. Lee, S. M. Kim, and K. Y. Suh, "Soft lithography for microfluidics: A Review," *Biochip J.*, vol. 2, no. 1, pp. 1–11, 2008.
[76] I. Ahmed, H. M. N. Iqbal, and Z. Akram, "Microfluidics Engineering: Recent Trends, Valorization, and Applications," *Arab. J. Sci. Eng.*, vol. 43, no. 1, pp. 23–32, 2018.
[77] D. I. Walsh, D. S. Kong, S. K. Murthy, and P. A. Carr, "Enabling Microfluidics: from Clean Rooms to Makerspaces," *Trends Biotechnol.*, vol. 35, no. 5, pp. 383–392, 2017.
[78] B. K. Gale *et al.*, "A review of current methods in microfluidic device fabrication and future commercialization prospects," *Inventions*, vol. 3, no. 3, 2018.
[79] A. A. S. Bhagat, H. Bow, H. W. Hou, S. J. Tan, J. Han, and C. T. Lim, "Microfluidics for cell separation," *Med. Biol. Eng. Comput.*, vol. 48, no. 10, pp. 999–1014, 2010.
[80] M. Antfolk and T. Laurell, "Continuous flow microfluidic separation and processing of rare cells and bioparticles found in blood – A review," *Anal. Chim. Acta*, vol. 965, pp. 9–35, 2017.
[81] J. Wu, Q. Chen, and J. M. Lin, "Microfluidic technologies in cell isolation and analysis for biomedical applications," *Analyst*, vol. 142, no. 3, pp. 421–441, 2017.
[82] W. Tang *et al.*, "Recent advances in microfluidic cell sorting techniques based on both physical and biochemical principles," *Electrophoresis*, vol. 40, no. 6, pp. 930–954, 2019.
[83] S. C. Guo, S. C. Tao, and H. Dawn, "Microfluidics-based on-a-chip systems for isolating and analysing extracellular vesicles," *J. Extracell. Vesicles*, vol. 7, no. 1, 2018.
[84] L. Reverté, B. Prieto-Simón, and M. Campàs, "New advances in electrochemical biosensors for the detection of toxins: Nanomaterials, magnetic beads and microfluidics systems. A review," *Anal. Chim. Acta*, vol. 908, pp. 8–21, 2016.
[85] P. Ajanth, A. Sudeepthi, and A. K. Sen, "Microfluidics Technology for Label-Free Isolation of Circulating Tumor Cells," *J. Inst. Eng. Ser. C*, vol. 101, no. 6, pp. 1051–1071, 2020.
[86] W. Su, H. Li, W. Chen, and J. Qin, "Microfluidic strategies for label-free exosomes isolation and analysis," *TrAC - Trends Anal. Chem.*, vol. 118, pp. 686–698, 2019.
[87] M. A. Md Ali, K. (Ken) Ostrikov, F. A. Khalid, B. Y. Majlis, and A. A. Kayani, "Active bioparticle manipulation in microfluidic systems," *RSC Adv.*, vol. 6, no. 114, pp. 113066–113094, 2016.
[88] Q. Luan, C. Macaraniag, J. Zhou, and I. Papautsky, "Microfluidic systems for hydrodynamic trapping of cells and clusters," *Biomicrofluidics*, vol. 14, no. 3, 2020.
[89] J. P. Beech, S. H. Holm, K. Adolfsson, and J. O. Tegenfeldt, "Sorting cells by size, shape and deformability," *Lab Chip*, vol. 12, no. 6, pp. 1048–1051, 2012.
[90] K. Lee, H. Shao, R. Weissleder, and H. Lee, "Acoustic purification of

extracellular microvesicles," *ACS Nano*, vol. 9, no. 3, pp. 2321–2327, 2015.
[91] K. Dholakia, B. W. Drinkwater, and M. Ritsch-Marte, "Comparing acoustic and optical forces for biomedical research," *Nat. Rev. Phys.*, vol. 2, no. 9, pp. 480–491, 2020.
[92] P. T. Kumar *et al.*, "Digital microfluidics for single bacteria capture and selective retrieval using optical tweezers," *Micromachines*, vol. 11, no. 3, 2020.
[93] S. D. Ibsen *et al.*, "Rapid Isolation and Detection of Exosomes and Associated Biomarkers from Plasma," *ACS Nano*, vol. 11, no. 7, pp. 6641–6651, 2017.
[94] R. T. Turgeon and M. T. Bowser, "Micro free-flow electrophoresis: Theory and applications," *Anal. Bioanal. Chem.*, vol. 394, no. 1, pp. 187–198, 2009.
[95] M. Islinger, C. Eckerskorn, and A. Völkl, "Free-flow electrophoresis in the proteomic era: A technique in flux," *Electrophoresis*, vol. 31, no. 11, pp. 1754–1763, 2010.
[96] D. E. Raymond, A. Manz, and H. M. Widmer, "Continuous Sample Pretreatment Using a Free-Flow Electrophoresis Device Integrated onto a Silicon Chip," *Anal. Chem.*, vol. 66, no. 18, pp. 2858–2865, 1994.
[97] C. X. Zhang and A. Manz, "High-Speed Free-Flow Electrophoresis on Chip," *Anal. Chem.*, vol. 75, no. 21, pp. 5759–5766, 2003.
[98] B. R. Fonslow, V. H. Barocas, and M. T. Bowser, "Using channel depth to isolate and control flow in a micro free-flow electrophoresis device," *Anal. Chem.*, vol. 78, no. 15, pp. 5369–5374, 2006.
[99] D. Kohlheyer, J. C. T. Eijkel, S. Schlautmann, A. Van Den Berg, and R. B. M. Schasfoort, "Microfluidic high-resolution free-flow isoelectric focusing," *Anal. Chem.*, vol. 79, no. 21, pp. 8190–8198, 2007.
[100] D. Kohlheyer, J. C. T. Eijkel, S. Schlautmann, A. Van Den Berg, and R. B. M. Schasfoort, "Bubble-free operation of a microfluidic free-flow electrophoresis chip with integrated pt electrodes," *Anal. Chem.*, vol. 80, no. 11, pp. 4111–4118, 2008.
[101] Y. A. Song, M. Chan, C. Cello, S. R. Tannenbaum, J. S. Wishnok, and J. Han, "Free-flow zone electrophoresis of peptides and proteins in PDMS microchip for narrow pi range sample prefractionation coupled with mass spectrometry," *Anal. Chem.*, vol. 82, no. 6, pp. 2317–2325, 2010.
[102] D. Janasek, M. Schilling, A. Manz, and J. Franzke, "Electrostatic induction of the electric field into free-flow electrophoresis devices," *Lab Chip*, vol. 6, no. 6, pp. 710–713, 2006.
[103] S. Jezierski, L. Gitlin, S. Nagl, and D. Belder, "Multistep liquid-phase lithography for fast prototyping of microfluidic free-flow-electrophoresis chips," *Anal. Bioanal. Chem.*, vol. 401, no. 8, pp. 2651–2656, 2011.
[104] S. Podszun *et al.*, "Enrichment of viable bacteria in a micro-volume by free-flow electrophoresis," *Lab Chip*, vol. 12, no. 3, pp. 451–457, 2012.
[105] T. Akagi, R. Kubota, M. Kobayashi, and T. Ichiki, "Development of a polymer-based easy-to-fabricate micro-free-flow electrophoresis device," *Jpn. J. Appl. Phys.*, vol. 54, no. 6, 2015.
[106] N. W. Frost and M. T. Bowser, "Using buffer additives to improve analyte stream stability in micro free flow electrophoresis," *Lab Chip*, vol. 10, no. 10, pp. 1231–1236, 2010.
[107] B. R. Fonslow and M. T. Bowser, "Optimizing band width and resolution in micro-free flow electrophoresis," *Anal. Chem.*, vol. 78, no. 24, pp. 8236–8244, 2006.

[108] C. Herzog, G. F. W. Jochem, P. Glaeser, and S. Nagl, “Gas removal in free-flow electrophoresis using an integrated nanoporous membrane,” *Microchim. Acta*, vol. 182, no. 3–4, pp. 887–892, 2014.
[109] S. Köhler, C. Weilbeer, S. Howitz, H. Becker, V. Beushausen, and D. Belder, “PDMS free-flow electrophoresis chips with integrated partitioning bars for bubble segregation,” *Lab Chip*, vol. 11, no. 2, pp. 309–314, 2011.
[110] S. Köhler, C. Benz, H. Becker, E. Beckert, V. Beushausen, and D. Belder, “Micro free-flow electrophoresis with injection molded chips,” *RSC Adv.*, vol. 2, no. 2, pp. 520–525, 2012.
[111] S. K. Anciaux, M. Geiger, and M. T. Bowser, “3D Printed Micro Free-Flow Electrophoresis Device,” *Anal. Chem.*, vol. 88, no. 15, pp. 7675–7682, Aug. 2016.
[112] A. C. Johnson and M. T. Bowser, “Micro free flow electrophoresis,” *Lab Chip*, vol. 18, no. 1, pp. 27–40, 2017.
[113] D. Kohlheyer, J. C. T. Eijkel, A. van den Berg, and R. B. M. Schasfoort, “Miniaturizing free-flow electrophoresis - A critical review,” *Electrophoresis*, vol. 29, no. 5, pp. 977–993, 2008.
[114] R. Kuhn and S. Hoffstetter, “Electrophoresis,” *Electrophoresis*, pp. 942–947, 1990.
[115] “Polyjet Technology,” 2011. [Online]. Available: http://www.3daddfab.com/technology/.
[116] A. Nilsson, F. Petersson, H. Jönsson, and T. Laurell, “Acoustic control of suspended particles in micro fluidic chips,” *Lab Chip*, vol. 4, no. 2, pp. 131–135, 2004.
[117] A. Posch, *A protocol for exosome isolation and characterization*, vol. 1295. 2015.
[118] A. Jeyaram and S. M. Jay, “Preservation and Storage Stability of Extracellular Vesicles for Therapeutic Applications,” vol. 20, no. 1, pp. 1–13, 2019.
[119] T. Laurell, F. Petersson, and A. Nilsson, “Chip integrated strategies for acoustic separation and manipulation of cells and particles,” *Chem. Soc. Rev.*, vol. 36, no. 3, pp. 492–506, 2007.
[120] Y. Gao, M. Wu, Y. Lin, and J. Xu, “Acoustic microfluidic separation techniques and bioapplications: A review,” *Micromachines*, vol. 11, no. 10, 2020.
[121] M. Antfolk, P. B. Muller, P. Augustsson, H. Bruus, and T. Laurell, “Focusing of sub-micrometer particles and bacteria enabled by two-dimensional acoustophoresis,” *Lab Chip*, vol. 14, no. 15, pp. 2791–2799, 2014.
[122] M. Wu *et al.*, “Isolation of exosomes from whole blood by integrating acoustics and microfluidics,” *Proc. Natl. Acad. Sci. U. S. A.*, vol. 114, no. 40, pp. 10584–10589, 2017.
[123] M. Wu, A. Ozcelik, J. Rufo, Z. Wang, R. Fang, and T. Jun Huang, “Acoustofluidic separation of cells and particles,” *Microsystems Nanoeng.*, vol. 5, no. 1, 2019.
[124] D. Xiaoyun, P. Li, S.-C. S. Lin, and Z. S. Stratton, “Surface acoustic wave microfluidics,” *Lab Chip*, vol. 13, no. 18, pp. 3626–3649, 2013.
[125] M. Koklu, A. C. Sabuncu, and A. Beskok, “Acoustophoresis in shallow microchannels,” *J. Colloid Interface Sci.*, vol. 351, no. 2, pp. 407–414, 2010.
[126] I. González, L. J. Fernández, T. E. Gómez, J. Berganzo, J. L. Soto, and A. Carrato, “A polymeric chip for micromanipulation and particle sorting by ultrasounds based on a multilayer configuration,” *Sensors Actuators, B*

Chem., vol. 144, no. 1, pp. 310–317, 2010.
[127] F. Petersson, A. Lena, A. Swa, and T. Laurell, "Free Flow Acoustophoresis: Microfluidic-Based Mode of Particle and Cell Separation," *Anal. Chem*, vol. 79, no. 14, pp. 5117–5123, 2007.
[128] M. E. Piyasena *et al.*, "Multinode acoustic focusing for parallel flow cytometry," *Anal. Chem.*, vol. 84, no. 4, pp. 1831–1839, 2012.
[129] F. Petersson, A. Nilsson, C. Holm, H. Jönsson, and T. Laurell, "Separation of lipids from blood utilizing ultrasonic standing waves in microfluidic channels," *Analyst*, vol. 129, no. 10, pp. 938–943, 2004.
[130] F. Petersson, A. Nilsson, C. Holm, H. Jönsson, and T. Laurell, "Continuous separation of lipid particles from erythrocytes by means of laminar flow and acoustic standing wave forces," *Lab Chip*, vol. 5, no. 1, pp. 20–22, 2005.
[131] Y. Chen *et al.*, "High-throughput acoustic separation of platelets from whole blood," *Lab Chip*, vol. 16, no. 18, pp. 3466–3472, 2016.
[132] A. Urbansky, P. Ohlsson, A. Lenshof, F. Garofalo, S. Scheding, and T. Laurell, "Rapid and effective enrichment of mononuclear cells from blood using acoustophoresis," *Sci. Rep.*, vol. 7, no. 1, pp. 1–9, 2017.
[133] W. J. Savage, J. R. Burns, and J. Fiering, "Safety of acoustic separation in plastic devices for extracorporeal blood processing," *Transfusion*, vol. 57, no. 7, pp. 1818–1826, 2017.
[134] M. C. Zalis *et al.*, "Label-free concentration of viable neurons, hESCs and cancer cells by means of acoustophoresis," *Integr. Biol. (United Kingdom)*, vol. 8, no. 3, pp. 332–340, 2016.
[135] P. Augustsson, C. Magnusson, M. Nordin, H. Lilja, and T. Laurell, "Microfluidic, label-free enrichment of prostate cancer cells in blood based on acoustophoresis," *Anal. Chem.*, vol. 84, no. 18, pp. 7954–7962, 2012.
[136] M. Antfolk, C. Magnusson, P. Augustsson, H. Lilja, and T. Laurell, "Acoustofluidic, Label-Free Separation and Simultaneous Concentration of Rare Tumor Cells from White Blood Cells," *Anal. Chem.*, vol. 87, no. 18, pp. 9322–9328, 2015.
[137] A. H. J. Yang and H. T. Soh, "Acoustophoretic sorting of viable mammalian cells in a microfluidic device," *Anal. Chem.*, vol. 84, no. 24, pp. 10756–10762, 2012.
[138] P. Ohlsson *et al.*, "Integrated Acoustic Separation, Enrichment, and Microchip Polymerase Chain Reaction Detection of Bacteria from Blood for Rapid Sepsis Diagnostics," *Anal. Chem.*, vol. 88, no. 19, pp. 9403–9411, 2016.
[139] B. Hammarström, T. Laurell, and J. Nilsson, "Seed particle-enabled acoustic trapping of bacteria and nanoparticles in continuous flow systems," *Lab Chip*, vol. 12, no. 21, pp. 4296–4304, 2012.
[140] P. Ohlsson, K. Petersson, P. Augustsson, and T. Laurell, "Acoustic impedance matched buffers enable separation of bacteria from blood cells at high cell concentrations," *Sci. Rep.*, vol. 8, no. 1, pp. 1–11, 2018.
[141] P. Dow, K. Kotz, S. Gruszka, J. Holder, and J. Fiering, "Acoustic separation in plastic microfluidics for rapid detection of bacteria in blood using engineered bacteriophage," *Lab Chip*, vol. 18, no. 6, pp. 923–932, 2018.
[142] A. A. Doinikov, "Acoustic radiation forces: classical theory and recent advances," *Transw. Res. Netw. India Recent Res. Devel. Acoust.*, vol. 37661, no. 1, pp. 39–67, 2003.
[143] J. Friend and L. Y. Yeo, "Microscale acoustofluidics: Microfluidics driven via acoustics and ultrasonics," *Rev. Mod. Phys.*, vol. 83, no. 2, pp. 647–704,

2011.
[144] I. Leibacher, S. Schatzer, and J. Dual, “Impedance matched channel walls in acoustofluidic systems,” *Lab Chip*, vol. 14, no. 3, pp. 463–470, 2014.
[145] I. Leibacher, P. Reichert, and J. Dual, “Microfluidic droplet handling by bulk acoustic wave (BAW) acoustophoresis,” *Lab Chip*, vol. 15, no. 13, pp. 2896–2905, 2015.
[146] R. Habibi, C. Devendran, and A. Neild, “Trapping and patterning of large particles and cells in a 1D ultrasonic standing wave,” *Lab Chip*, vol. 17, no. 19, pp. 3279–3290, 2017.
[147] M. Gröschl, “Ultrasonic Separation of Suspended Particles - Part I: Fundamentals,” *Acustica*, vol. 84, no. 3, pp. 432–447, 1998.
[148] A. A. Doinikov, “Acoustic radiation pressure on a rigid sphere in a viscous fluid,” *Proc. - R. Soc. London, A*, vol. 447, no. 1931, pp. 447–466, 1994.
[149] H. Bruus, “Acoustofluidics 1: Governing equations in microfluidics,” *Lab Chip*, vol. 11, no. 22, pp. 3742–3751, 2011.
[150] H. Bruus, “Acoustofluidics 2: Perturbation theory and ultrasound resonance modes,” *Lab Chip*, vol. 12, no. 1, pp. 20–28, 2012.
[151] R. J. Townsend, M. Hill, N. R. Harris, and N. M. White, “Modelling of particle paths passing through an ultrasonic standing wave,” *Ultrasonics*, vol. 42, no. 1–9, pp. 319–324, 2004.
[152] H. Bruus, “Acoustofluidics 7: The acoustic radiation force on small particles,” *Lab Chip*, vol. 12, no. 6, pp. 1014–1021, 2012.
[153] P. B. Muller, R. Barnkob, M. J. H. Jensen, and H. Bruus, “A numerical study of microparticle acoustophoresis driven by acoustic radiation forces and streaming-induced drag forces,” *Lab Chip*, vol. 12, no. 22, pp. 4617–4627, 2012.
[154] R. Barnkob, P. Augustsson, T. Laurell, and H. Bruus, “Acoustic radiation- and streaming-induced microparticle velocities determined by microparticle image velocimetry in an ultrasound symmetry plane,” *Phys. Rev. E - Stat. Nonlinear, Soft Matter Phys.*, vol. 86, no. 5, pp. 1–11, 2012.
[155] H. Bruus, “Acoustofluidics 10: Scaling laws in acoustophoresis,” *Lab Chip*, vol. 12, no. 9, pp. 1578–1586, 2012.
[156] R. Barnkob, P. Augustsson, T. Laurell, and H. Bruus, “Measuring the local pressure amplitude in microchannel acoustophoresis,” *Lab Chip*, vol. 10, no. 5, pp. 563–570, 2010.
[157] P. Augustsson, R. Barnkob, S. T. Wereley, H. Bruus, and T. Laurell, “Automated and temperature-controlled micro-PIV measurements enabling long-term-stable microchannel acoustophoresis characterization,” *Lab Chip*, vol. 11, no. 24, pp. 4152–4164, 2011.
[158] R. Barnkob, I. Iranmanesh, M. Wiklund, and H. Bruus, “Measuring acoustic energy density in microchannel acoustophoresis using a simple and rapid light-intensity method,” *Lab Chip*, vol. 12, no. 13, pp. 2337–2344, 2012.
[159] J. Dual and D. Möller, “Acoustofluidics 4: Piezoelectricity and application in the excitation of acoustic fields for ultrasonic particle manipulation,” *Lab Chip*, vol. 12, no. 3, pp. 506–514, 2012.
[160] S. Karthick and A. K. Sen, “Improved understanding of the acoustophoretic focusing of dense suspensions in a microchannel,” *Phys. Rev. E*, vol. 96, no. 5, pp. 1–10, 2017.
[161] A. Lenshof, M. Evander, T. Laurell, and J. Nilsson, “Acoustofluidics 5: Building microfluidic acoustic resonators,” *Lab Chip*, vol. 12, no. 4, pp. 684–695, 2012.

[162] M. Gunetti *et al.*, "Validation of analytical methods in GMP: The disposable Fast Read 102® device, an alternative practical approach for cell counting," *J. Transl. Med.*, vol. 10, no. 1, pp. 1–12, 2012.
[163] A. Garcia-Sabaté, A. Castro, M. Hoyos, and R. González-Cinca, "Experimental study on inter-particle acoustic forces," *J. Acoust. Soc. Am.*, vol. 135, no. 3, pp. 1056–1063, 2014.
[164] D. Saeidi, M. Saghafian, S. Haghjooy Javanmard, B. Hammarström, and M. Wiklund, "Acoustic dipole and monopole effects in solid particle interaction dynamics during acoustophoresis," *J. Acoust. Soc. Am.*, vol. 145, no. 6, pp. 3311–3319, 2019.
[165] K. Raj M and S. Chakraborty, "PDMS microfluidics: A mini review," *J. Appl. Polym. Sci.*, vol. 137, no. 27, pp. 1–14, 2020.
[166] C. Potrich, L. Lunelli, M. Cocuzza, S. L. Marasso, C. F. Pirri, and C. Pederzolli, "Simple PDMS microdevice for biomedical applications," *Talanta*, vol. 193, pp. 44–50, Feb. 2019.
[167] F. Schneider, T. Fellner, J. Wilde, and U. Wallrabe, "Mechanical properties of silicones for MEMS," *J. Micromechanics Microengineering*, vol. 18, no. 6, 2008.
[168] I. D. Johnston, D. K. McCluskey, C. K. L. Tan, and M. C. Tracey, "Mechanical characterization of bulk Sylgard 184 for microfluidics and microengineering," *J. Micromechanics Microengineering*, vol. 24, no. 3, 2014.
[169] Q. Tu *et al.*, "Surface modification of poly(dimethylsiloxane) and its applications in microfluidics-based biological analysis," *Rev. Anal. Chem.*, vol. 31, no. 3–4, pp. 177–192, 2012.
[170] A. Mata, A. J. Fleischman, and S. Roy, "Characterization of Polydimethylsiloxane (PDMS) Properties for Biomedical Micro/Nanosystems," *Biomed. Microdevices*, vol. 7, no. 4, pp. 281–293, 2005.
[171] I. J. Gomez, B. Arnaiz, M. Cacioppo, F. Arcudi, and M. Prato, "Nitrogen-doped Carbon Nanodots for bioimaging and delivery of paclitaxel," *J. Mater. Chem. B*, vol. 6, no. 35, 2018.
[172] G. G. Morbioli, N. C. Speller, and A. M. Stockton, "A practical guide to rapid-prototyping of PDMS-based microfluidic devices: A tutorial," *Anal. Chim. Acta*, vol. 1135, pp. 150–174, 2020.
[173] M. Pardelova, D. Pudiš, D. Jandura, and P. Gaso, "PDMS based micro-optics and microchannels for lab-on-a-chip application," *Opt. Sensors 2015*, vol. 9506, no. May 2015, p. 95061E, 2015.
[174] R. P. Bajpai, U. Chandrasekhar, and A. R. Arankalle, *Lecture Notes in Mechanical Engineering Innovative Design, Analysis and and Automotive Practices in Aerospace Development Engineering*. 2014.
[175] G. Gonzalez, A. Chiappone, K. Dietliker, C. F. Pirri, and I. Roppolo, "Fabrication and Functionalization of 3D Printed Polydimethylsiloxane-Based Microfluidic Devices Obtained through Digital Light Processing," *Adv. Mater. Technol.*, vol. 5, no. 9, pp. 1–10, 2020.
[176] S. L. Marasso *et al.*, "Optimized design and fabrication of a microfluidic platform to study single cells and multicellular aggregates in 3D," *Microfluid. Nanofluidics*, vol. 21, no. 2, p. 29, 2017.
[177] C. Potrich *et al.*, "OncomiR detection in circulating body fluids: A PDMS microdevice perspective," *Lab Chip*, vol. 14, no. 20, pp. 4067–4075, 2014.
[178] N. C. Speller *et al.*, "Cutting edge microfluidics: Xurography and a

microwave," *Sensors Actuators, B Chem.*, vol. 291, no. March, pp. 250–256, 2019.
[179] S. Halldorsson, E. Lucumi, R. Gómez-Sjöberg, and R. M. T. Fleming, "Advantages and challenges of microfluidic cell culture in polydimethylsiloxane devices," *Biosens. Bioelectron.*, vol. 63, pp. 218–231, 2015.
[180] H. Y. Y. Nyein *et al.*, "A Wearable Microfluidic Sensing Patch for Dynamic Sweat Secretion Analysis," *ACS Sensors*, vol. 3, no. 5, pp. 944–952, 2018.
[181] Y. Gao, H. Ota, E. W. Schaler, K. Chen, and A. Zhao, "Wearable Devices: Wearable Microfluidic Diaphragm Pressure Sensor for Health and Tactile Touch Monitoring," *Adv. Mater.*, vol. 29, no. 39, 2017.
[182] D. Huh, B. D. Matthews, A. Mammoto, M. Montoya-Zavala, H. Y. Hsin, and I. Donald E., "Reconstituting Organ-Level Lung," *Science (80-.).*, no. June, pp. 1662–1668, 2010.
[183] A. Raj, P. P. A. Suthanthiraraj, and A. K. Sen, "Pressure-driven flow through PDMS-based flexible microchannels and their applications in microfluidics," *Microfluid. Nanofluidics*, vol. 22, no. 11, pp. 1–25, 2018.
[184] S. Mishra, A. Thakur, S. Redenti, and M. Vazquez, "A model microfluidics-based system for the human and mouse retina," *Biomed. Microdevices*, vol. 17, no. 6, 2015.
[185] D. Tsvirkun, A. Grichine, A. Duperray, C. Misbah, and L. Bureau, "Microvasculature on a chip: Study of the Endothelial Surface Layer and the flow structure of Red Blood Cells," *Sci. Rep.*, vol. 7, no. March, pp. 1–11, 2017.
[186] G. Beamson and D. Briggs, *High Resolution XPS of Organic Poly- mers. The Scienta ESCA300 Data- base*. 1992.
[187] G. Speranza and R. Canteri, "RxpsG a new open project for Photoelectron and Electron Spectroscopy data processing," *SoftwareX*, vol. 10, p. 100282, 2019.
[188] J. Schindelin *et al.*, "Fiji: An open-source platform for biological-image analysis," *Nat. Methods*, vol. 9, no. 7, pp. 676–682, 2012.
[189] H. J. Crabtree *et al.*, "Inhibition of on-chip PCR using PDMS-glass hybrid microfluidic chips," *Microfluid. Nanofluidics*, vol. 13, no. 3, pp. 383–398, 2012.
[190] C. Potrich *et al.*, "Effect of materials for micro-electro-mechanical systems on PCR yield," *Eur. Biophys. J.*, vol. 39, no. 6, pp. 979–986, 2010.
[191] G. C. Santini *et al.*, "miRNA purification with an optimized PDMS microdevice: Toward the direct purification of low abundant circulating biomarkers," *Biophys. Chem.*, vol. 229, no. April, pp. 142–150, 2017.
[192] P. Louette, F. Bodino, and J.-J. Pireaux, "Poly(dimethyl siloxane) (PDMS) XPS Reference Core Level and Energy Loss Spectra," *Surf. Sci. Spectra*, vol. 12, no. 1, pp. 38–43, 2005.
[193] L. Lunelli *et al.*, "PDMS-based microdevices for the capture of MicroRNA biomarkers," *Appl. Sci.*, vol. 10, no. 11, 2020.
[194] X. Chen *et al.*, "Identification of ten serum microRNAs from a genome-wide serum microRNA expression profile as novel noninvasive biomarkers for nonsmall cell lung cancer diagnosis," *Int. J. Cancer*, vol. 130, no. 7, pp. 1620–1628, 2012.
[195] M. Cui *et al.*, "Circulating MicroRNAs in Cancer: Potential and Challenge," *Front. Genet.*, vol. 10, no. July, 2019.

Appendix A

I. First micro-free flow device fabrication

Concerning the first µFFE device fabrication process steps, they were the same presented for the enhanced µFFE device (see **2.2.2**), but instead of integrating threaded fluidic fittings directly into the 3D design, they were milled into a PMMA holder. The 3D printed part of the device was manufactured as already mentioned. On the 750 µm thick PMMA slice, inlets and outlets were milled using a computer numerical control (CNC) milling machine (BENCHMAN). After that, either the 3D printed part and the PMMA slide were cleaned by isopropanol and flushed by a nitrogen flux before bonding. Then, a uniform and irreversible bonding between the 3D printed part and the PMMA slide was achieved by using as glue Poly(ethylene glycol) diacrylate (PEGDA) 575 resin (Sigma-Aldrich) mixed with 1% IRGACURE 819 (Sigma-Aldrich) by leaving the whole device one hour on hot plate at 70°C. After that, two stainless steel wire electrodes (The Crazy Wire Company) were manually inserted in the corresponding lateral channels. Finally, the first µFFE device was placed in a PMMA holder composed by two slides of PMMA with thickness equal to 3 mm. In details, on the slice representing the top of the PMMA holder inlets were milled and threated to guarantee a stable connection with the tubes and the device. Outlets were also milled and on the back of it, an additional milling was performed to host o-ring elements. Finally, along borders of both slides of PMMA holder six holes of diameter 5 mm were milled to allow the clamping of the device into the PMMA holder through screws, to avoid solutions leakages during tests (**Figure Appendix A I.I**).

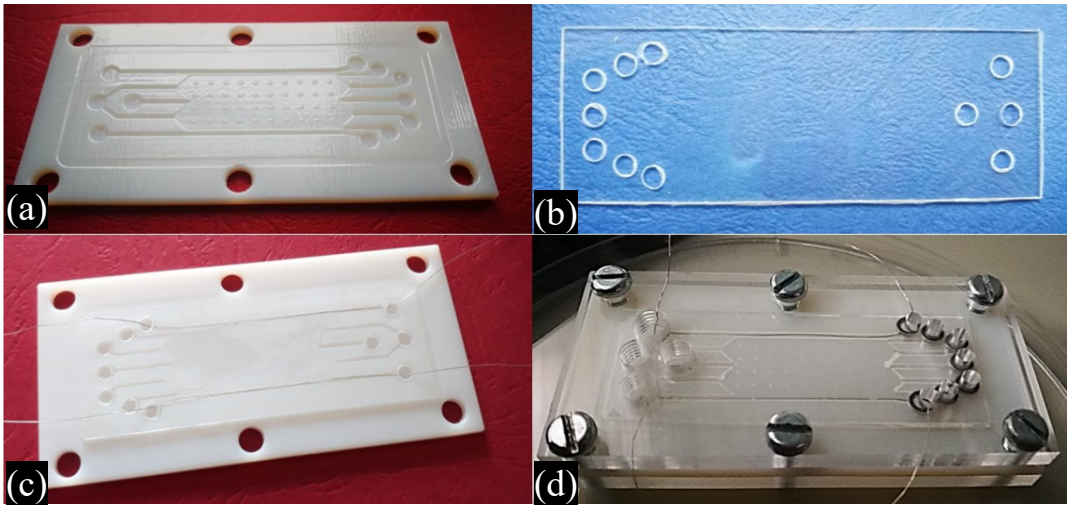

Figure Appendix A I.I First µFFE device fabrication: (a) 3D printed microfluidics, (b) PMMA slide inlets and outlets milling, (c) electrodes insertion and (d) device sealing.

II. First micro-free-flow device leakage test

To evaluate the bonding between the 3D printed microfluidics and the PMMA top cover, leakage tests were performed by filling the device with an orange food dye. After having injected the orange food dye into the inlet access, whole microfluidics was filled by the solutions as depicted in **Figure Appendix A II.I**.

Thus, not only the device bonding performance was verified, but it was possible to notice that the microfluidics was free from the excess of glue employed during the sealing step of the device thanks to the gutter designed near the device borders.

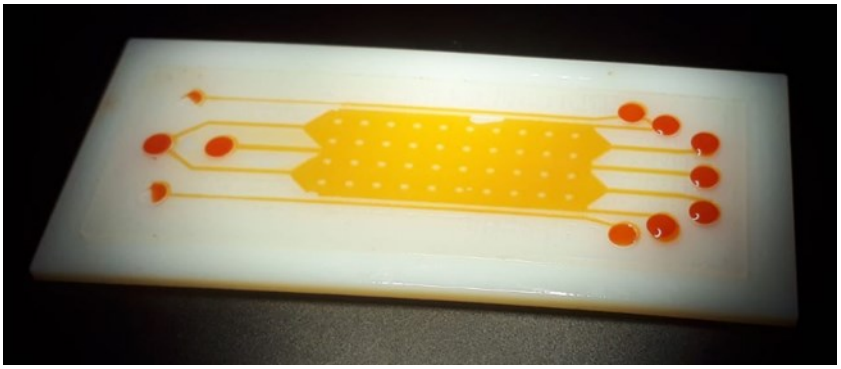

Figure Appendix A II.I First µFFE device leakage test performed with orange food dye.

Finally, leakage tests failed when the device was placed into its PMMA holder. As showed in **Figure Appendix A II.II** the interconnections between tubes and the device were not able to guaranteee a stable sealing, indeed a little amount of solution spread in the space between the top of the device in correspondence of inlet and outlet accesses and the backside of the top PMMA holder.
Thus, to overcome this critical issue, the enhanced µFFE device was developed with threaded fluidic fittings directly integrated into the 3D design on the backside of the microfluidics in correspondence of inlet and outlet ports.

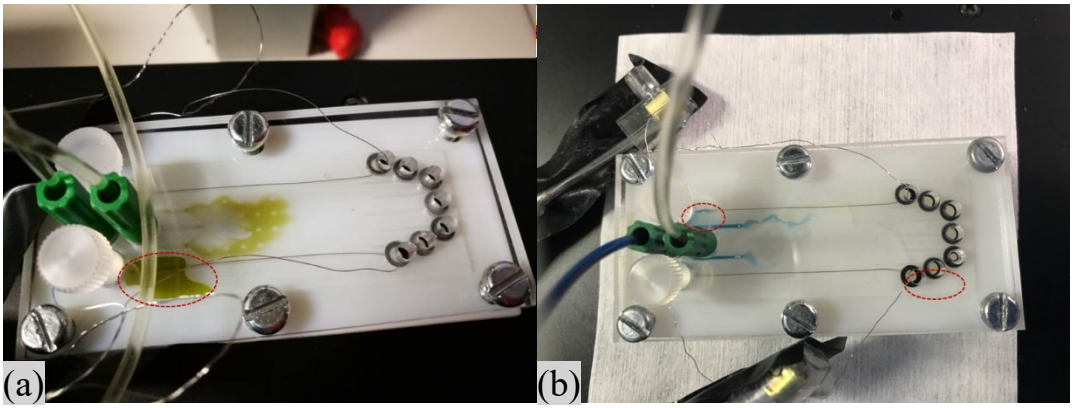

Figure Appendix A II.II First µFFE device leakage tests performed with green (a) and blue (b) food dyes when the device was clamped into the PMMA holder. Dotted circles highlight where leakage tests failed.

Appendix B

I. Spiral-shape mold microdevice fabrication

Concerning the mold material employed for the fabrication of the spiral-shape microdevices (see **4.2.2**), instead of spinning SU-8 photoresist on silicon wafers, thus using them as supports, in another fabrication process themselves were used as mold. In details, spiral-shape configurations were etched into 4-inch n-type silicon wafer with (100) orientation and 0.35 mm thick, finished with 1 μm of thermal SiO_2. At first step, the Omnicoat photoresist (Microchemicals GmbH) was coated on the silicon wafer by using a spin coater (Spinner 150 Wafer Spinner) by setting 10 seconds at 500 rpm and 30 seconds at 3000 rpm to guarantee a perfect adhesion between the silicon surface and the photoresist used as mask. Then, a soft bake step occurred on a hot plate at 200°C for 60 seconds. Next, SU-8 3005 (Microchemicals GmbH) was spinned on silicon wafer setting 10 seconds at 500 rpm and 60 seconds at 1000 rpm. The soft bake process was run in two thermal steps: the first one at 65 °C for 30 seconds and the second step at 95 °C for 3 minutes, both performed on the hot plate. After that, the SU-8 was exposed for 90 seconds to standard UV photolithography by means of a double side mask aligner (Neutronix Quintel NXQ 4006) used in contact mode, ensuring the correct alignment between the SU-8 3005 and the desired mask patterns. As the previous soft bake step, the post bake was characterized by two thermal steps: the first at 65 °C for 1 minute and the second one at 95 °C for 5 minutes, on a hot plate. After that, to obtain the desired exposed pattern, the SU-8 was developed using Propylene glycol methyl ether acetate (PGMEA) for 40 seconds, then rinsed with 2-propanol (Sigma-Aldrich) and dried with a nitrogen flux. Next, a Buffer Oxide Etching (BOE) was performed for 15 minutes to remove the thermal oxide in the unwanted area and then the spiral-shape microchannels etching was completed by Deep Reactive Ion Etching (DRIE) (Oxford Plasmalab 100 System). A Bosch® process was performed to obtain about 200 μm deep microdevices using the following parameters: 1500 W of ICP power, 10 W of RF power, 50 sccm of C_4F_8 for the passivation step extent of 4 seconds, and 150 sccm of SF_6 for the etch step extent of 10 seconds imposing 14 sccm of He backside cooling to maintain 18°C on the wafer in both steps. After that, the etched silicon wafer was submerged into a solution of sulphuric acid and hydrogen peroxide in a 3:1 ratio (v/v) for 5 minutes to remove the residual SU-8 mask layer, rinsed 3 times in water and dried with a nitrogen flux. Finally, the residual thermal oxide was removed through a further BOE process of 15 minutes to obtain the finished mold.

Following steps in which silicon mold was involved to manufacture PDMS replicas were the same performed for the SU-8 mold (see **4.2.2**) (**Figure Appendix B I.I**).

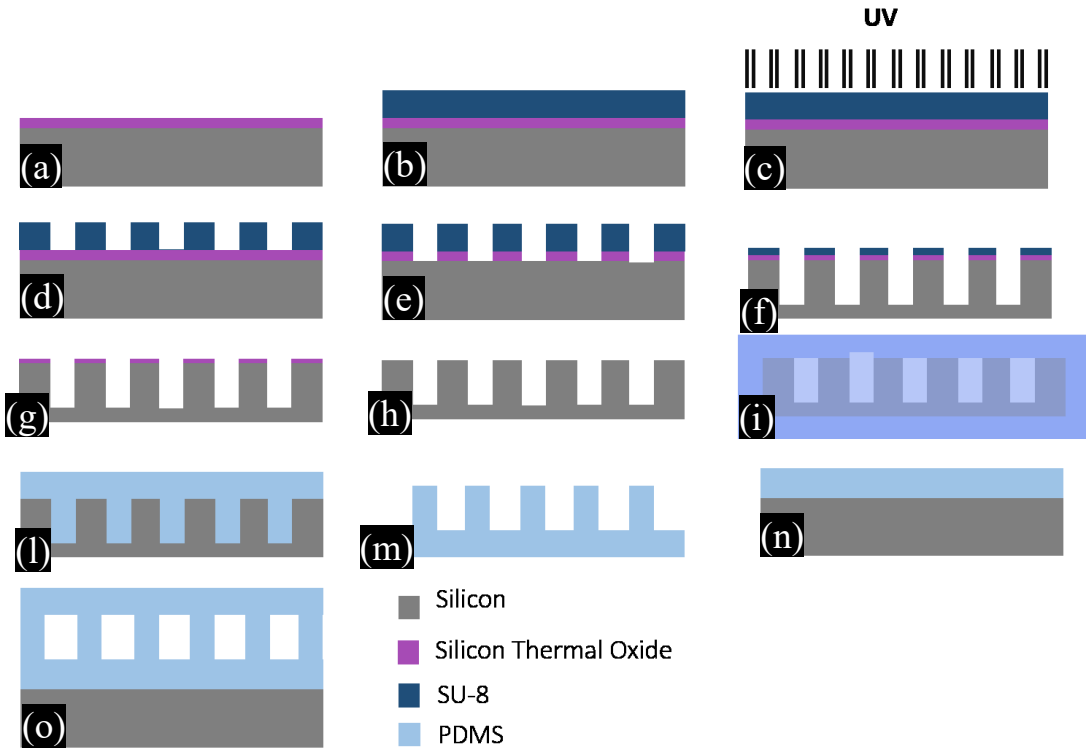

Figure Appendix B I.I Fabrication process flow: (a) silicon wafer, (b) SU-8 spinning on silicon wafer, (c) SU-8 exposition, (d) SU-8 develop, (e) BOE on silicon thermal oxide, (f) DRIE step, (g) remove of residual SU-8 mask, (h) BOE to remove the residual silicon thermal oxide, (i) silicon mold silanization, (l) PDMS pouring on SU-8 mold, (m) PDMS spiral replica, (n) silicon slice with PDMS thin layer and (o) final device assembled.

II. Spiral-shape mold characterization

Morphological analyses on silicon mold and PDMS replicas were performed to evaluate feature dimensions of both spiral-shape microdevices. FE-SEM characterizations were performed to make a comparison between real microchannel widths, lengths and wall spacing widths and the design ones.

Firstly, to define a recipe for the Bosch® process were set different ICP power during the etch step. **Figure Appendix B II.I** reported silicon molds characterized by ICP power of 1500 W and 1300 W during the etch step. In details, Chip A mold was etched using 1500 W of ICP power, while Chip B was etched with 1300 W of ICP one. As it was possible to notice, molds involved during these preliminary tests were characterized by 60 µm microchannels deep. This because, the aim of these preliminary tests were focused on evaluate the correct reproducibility of microchannel and wall spacing widths. In details, microchannels of Chip A possessed an width average value of 230.03±4.56 µm and walls spacing dimensions mean value equal to 172.33±4.48 µm. Regarding Chip B widths mean values were 56.22±2.31 µm and 151.97±1.87 µm of microchannels and walls spacing, respectively. Since Chip B dimensions corresponded to the design ones, for further test it was decided to exploit the Bosch® process setting an ICP power equal to 1300 W.

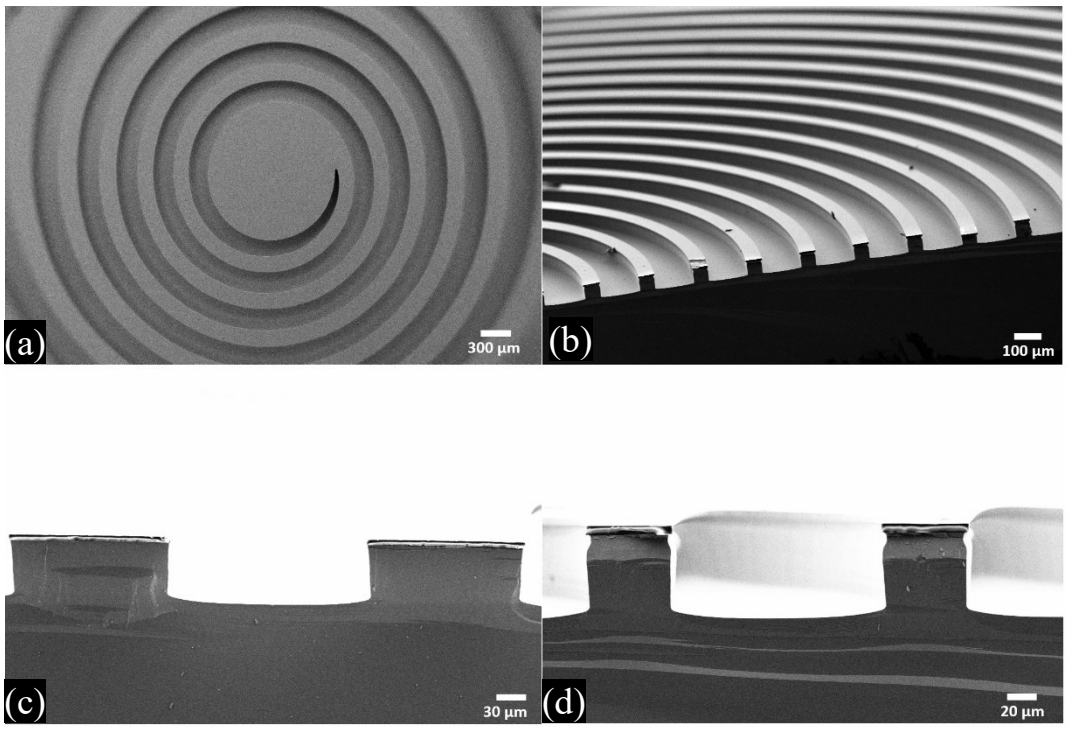

Figure Appendix B II.I FESEM images of spiral-shape microdevice molds: (a) Chip A, magnification 51x, (b) Chip B, magnification 150x, (c) Chip A cross section of features, magnification 500x and (d) Chip B cross section of features, magnification 800x.

Figure Appendix B II.II showed the final mold of Chip A and the PDMS-replicas derived from the mold of Chip B. Regarding Chip A, a pronounced under etch effect was observed in the upper sides of the trenches, suggesting that during the etching step ions etched silicon placed under the mask. Due to this, microchannel dimensions average values were 125.91±14.95 in width and 192.30±3.50 in height, while walls spacing mean value was 302.90±18.51. Also mean values analyzed from PDMS-replicas of Chip B mold demonstrated a discrepancy between the mold dimensions and the design ones. Indeed, Chip B microchannel mean values were 39.81±6.62 µm and 187.53±5.94 µm of width and depth, respectively, with wall spacing 166.52±6.09 µm wide. To conclude, further experiments must be performed to define the optimal settings of the Bosch® process to etch molds with the right design dimensions and to avoid the under etch effect visible in both spiral-shape molds. For instance, decreasing the etching step time or increasing the channel dimensions during the lithographic step could be attempt to respect the design dimensions, while the under etch effect could be avoided by employing a unique mask material such as silicon oxide.

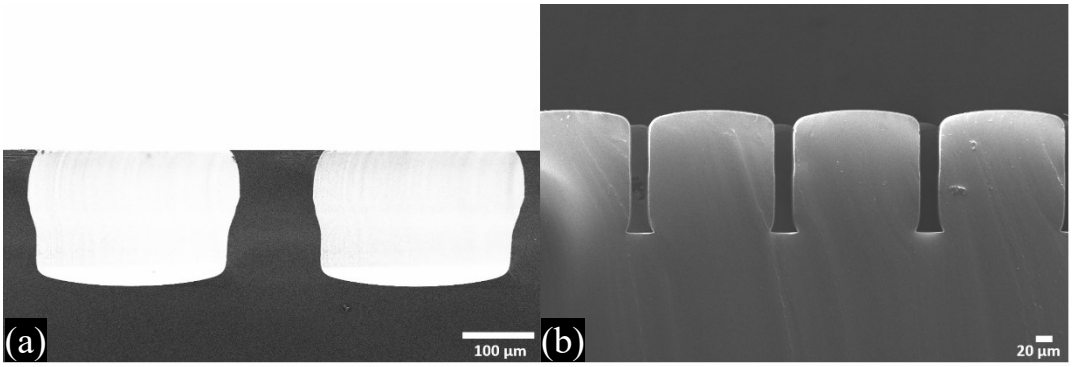

Figure Appendix B II.II FESEM images of spiral-shape microdevices: (a) Chip A mold features magnification 400x and (b) Chip B PDMS-replica, magnification 500x.

Appendix C

I. Papers published during PhD

Canavese Giancarlo, Ancona Andrea, Racca Luisa, Canta Marta, Dumontel Bianca, Barbaresco Federica, Limongi Tania, and Cauda Valentina, 2018, 'Nanoparticle-assisted ultrasound: A special focus on sonodynamic therapy against cancer', *Chemical Engineering Journal*, 340: 155-172.

Lorenzo Lunelli, Federica Barbaresco, Giorgio Scordo, Cristina Potrich, Lia Vanzetti, Simone Luigi Marasso, Matteo Cocuzza, Candido Fabrizio Pirri and Cecilia Pederzolli, 2020, 'PDMS-Based Microdevices for the Capture of MicroRNA Biomarkers', *Applied Science*, 10: 3867-3884.

Federica Barbaresco, Matteo Cocuzza, Candido Fabrizio Pirri and Simone Luigi Marasso, 2020, 'Application of a Micro Free-Flow Electrophoresis 3D Printed Lab-on-a-Chip for Micro-Nanoparticles Analysis', *Nanomaterials*, 10: 1277-1292.